

## Piezotronics and Piezo-phototronics of Third Generation Semiconductor Nanowires

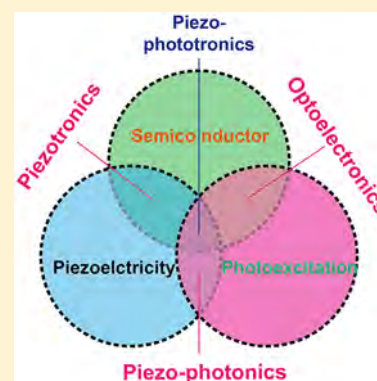
Caofeng Pan,<sup>\*,†,‡,§</sup> Junyi Zhai,<sup>\*,†,‡,§</sup> and Zhong Lin Wang<sup>\*,†,‡,§</sup>

<sup>†</sup>CAS Center for Excellence in Nanoscience, Beijing Key Laboratory of Micro-nano Energy and Sensor, Beijing Institute of Nanoenergy and Nanosystems, Chinese Academy of Sciences, Beijing 100083, P. R. China

<sup>‡</sup>School of Nanoscience and Technology, University of Chinese Academy of Sciences, Beijing 100049, P. R. China

<sup>§</sup>School of Material Science and Engineering, Georgia Institute of Technology, Atlanta, Georgia 30332, United States

**ABSTRACT:** With the fast development of nanoscience and nanotechnology in the last 30 years, semiconductor nanowires have been widely investigated in the areas of both electronics and optoelectronics. Among them, representatives of third generation semiconductors, such as ZnO and GaN, have relatively large spontaneous polarization along their longitudinal direction of the nanowires due to the asymmetric structure in their *c*-axis direction. Two-way or multiway couplings of piezoelectric, photoexcitation, and semiconductor properties have generated new research areas, such as piezotronics and piezo-phototronics. In this review, an in-depth discussion of the mechanisms and applications of nanowire-based piezotronics and piezo-phototronics is presented. Research on piezotronics and piezo-phototronics has drawn much attention since the effective manipulation of carrier transport, photoelectric properties, *etc.* through the application of simple mechanical stimuli and, conversely, since the design of new strain sensors based on the strain-induced change in semiconductor properties.



### CONTENTS

1. Introduction: The Origin of Piezotronics and Piezo-phototronics	B		
1.1. Piezopotential	B		
1.2. Piezotronics	C		
1.3. Piezo-phototronics and Piezophotonics	C		
1.4. Piezoelectric Semiconductor NWs	C		
2. Synthesis of Piezoelectric Semiconductor NWs	D		
2.1. Wet Chemical Synthesis	D		
2.1.1. Electrochemical Deposition	D		
2.1.2. Hydrothermal Synthesis	D		
2.2. Chemical and Physical Vapor Depositions	E		
2.2.1. Chemical Vapor Deposition	E		
2.2.2. Pulsed Laser Deposition	F		
2.3. Top-Down Fabrication	F		
3. Mechanisms of Piezotronics and Piezo-phototronics	G		
3.1. Piezotronic Transistors vs Traditional Field Effect Transistors	G		
3.2. Theoretical Framework of Piezotronics	H		
3.2.1. NW p–n Junctions	H		
3.2.2. Metal–Semiconductor Schottky Contact	J		
3.2.3. Metal–Wurtzite Semiconductor Contact	K		
3.3. Theoretical Discussion of the Piezo-Phototronic Effect	K		
3.3.1. Fundamental Theory for Piezo-phototronics	K		
3.3.2. Piezo-phototronic Effect in LEDs	L		
3.3.3. Piezo-phototronic Effect in Photodetectors	N		
3.3.4. Piezo-phototronic Effect in Solar Cells	P		
3.4. Temperature Dependence of Piezotronics and Piezo-phototronics	U		
4. Piezotronics and Its Applications	U		
4.1. Piezotronic Effect-Based Strain Sensors	U		
4.2. Piezotronic Strain-Gated Piezoelectric Electromechanical Switches	V		
4.3. Piezotronic Transistors Based on Vertical NWs	W		
4.4. Piezotronic Transistor Arrays and Tactile Imaging	W		
4.5. Piezotronic Effect-Enhanced Schottky-Contact Nanosensors	X		
4.5.1. Highly Sensitive, Fast-Response NW Sensors with Schottky Contacts	Y		
4.5.2. Piezotronic Effect-Enhanced Schottky-Contact Sensors	AA		
5. Piezo-phototronics and Its Applications	AB		
5.1. Piezo-phototronic Effect in Solar Cells	AB		
5.1.1. Fundamentals of Piezo-phototronics in Solar Cells	AB		
5.1.2. Piezo-phototronics in Thin Film Solar Cells	AD		

**Special Issue:** 1D Nanomaterials/Nanowires

**Received:** October 1, 2018

5.1.3. Piezo-phototronic Effect in NW Solar Cells	AE
5.1.4. Piezo-phototronic Effect in NW Array Solar Cells	AF
5.2. Piezo-phototronic Effect in Photodetectors	AH
5.2.1. Single NW Photodetector Based on the Piezo-phototronic Effect	AI
5.2.2. Core–Shell NW Photodetector Based on the Piezo-phototronic Effect	AK
5.2.3. Piezo-phototronic Effect in NW-Based Heterojunction Photodetectors	AK
5.2.4. Piezo-phototronic Effect in NW Photodetector Arrays	AK
5.3. Piezo-phototronic Effect in Light-Emitting Diodes	AM
5.3.1. Theoretical Study of p–n Junction Piezo-phototronic Nano-LEDs	AM
5.3.2. Single NW LED Based on the Piezo-phototronic Effect	AM
5.3.3. Piezo-phototronic Effect in LED Arrays	AO
5.3.4. Piezo-phototronic Effect in Visible Mechanosensory Electronics	AP
5.4. Piezo-phototronic Effect in Electrochemical Processes	AR
6. Conclusion and Perspective	AT
Author Information	AV
Corresponding Authors	AV
ORCID	AV
Notes	AV
Biographies	AV
Acknowledgments	AW
References	AW

## 1. INTRODUCTION: THE ORIGIN OF PIEZOTRONICS AND PIEZO-PHOTOTRONICS

### 1.1. Piezopotential

The piezoelectric effect is a coupling of mechanics and electrical polarization. When a dielectric material is deformed through an applied force along its asymmetry direction, positive and negative charges are generated on both opposite surfaces. In the case when the applied force has been removed, the dielectric material will come back to the original uncharged status. Besides, the polarity of the charge also changes upon the change of the direction of the applied force. The most classic piezoelectric material is lead zirconate titanate (PZT) ceramic with a perovskite structure, which has been successfully applied in actuators, strain sensors, and energy harvesting equipment.<sup>1,2</sup> However, the resistance of PZT is too large; thus, this material is not suitable for use in electronic devices. Traditionally, the study of piezoelectric materials and the piezoelectric effect has been mainly limited to the field of ceramic materials because perovskite materials, represented by PZT, have good piezoelectric and mechanical properties.

The working principle of the fundamental devices (transistors, diodes, etc.) of current electronics is based on the movement and/or accumulation of charge carriers. Most of the first- and second-generation semiconductor materials do not have piezoelectric properties due to their symmetric crystal structure. However, representatives of third generation semiconductors, GaN and ZnO, have piezoelectric properties along their *c*-axis. These wurtzite materials are hexagonal crystal

systems; they have asymmetric structures along and perpendicular to the *c*-axis. Take a ZnO single crystal nanowire (NW) as an example.<sup>3–5</sup> The Zn<sup>2+</sup> cation and the adjacent O<sup>2–</sup> anion form a cation-centered tetrahedral structure.<sup>6,7</sup> When no external stress is applied to NW, the charge centers of the cations and the anions overlap, as shown in Figure 1. When

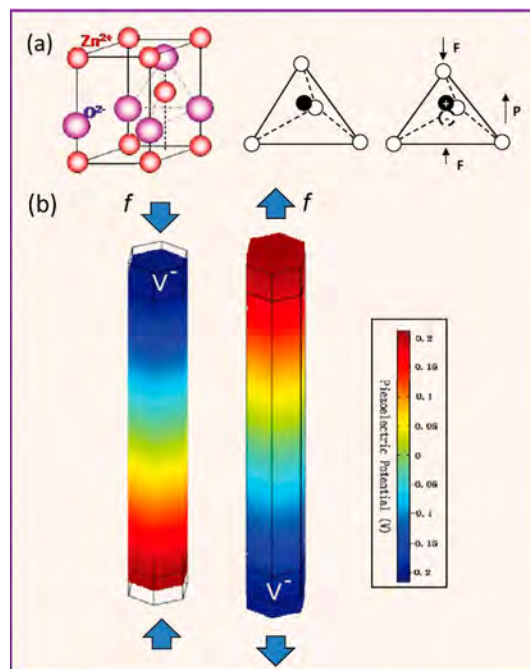


**Figure 1.** Piezoelectric potential in a wurtzite single crystal. (a) Schematic of the atomic model of a ZnO unit cell. Reproduced with permission from ref 6. Copyright 2012 John Wiley and Sons. (b) Distribution of the piezopotential along the longitudinal direction of a ZnO NW due to external compressive or tensile strain, obtained through numerical calculations. The external force (80 nN) is applied along the *c*-axis of ZnO and the *x*-axis. Here, the length of the NW is 600 nm, and the hexagonal side length is 25 nm. Reproduced with permission from ref 17. Copyright 2009 American Institute of Physics.

applying an external stress along its *c*-axis of the ZnO NW, the charge centers of anions and cations are relatively displaced; thus, a dipole moment is formed. A potential distribution along the stress direction is macroscopically generated after dipole moment superposition occurs in all the cells inside the NW. Such potential is the so-called piezoelectric potential, or piezopotential. When external mechanical deformation is applied, the piezoelectric potential generated in the material can drive electrons to flow in the external circuit load, which is the fundamental mechanism of a nanogenerator.<sup>8–13</sup>

Without considering the effect of doping in ZnO NWs, the piezoelectric potential distribution of ZnO NWs subjected to an external stress can be calculated by the Lippman theory.<sup>14,15</sup> Here, the longitudinal directions of the ZnO NWs are along their *c*-axis. When this NW is subjected to a tensile stress of 80 nN, the piezoelectric potential induced at the two ends of the ZnO NW is approximately 0.4 V, and the piezoelectric potential at the +*c* end of the NW is positive (Figure 1). When the applied stress is maintained at the same magnitude but the tensile stress is changed to a compressive stress, the positive and negative polarities of the piezoelectric potential distribution in the NW are reversed, but the piezoelectric potential difference between the two ends remains 0.4 V. At this time,

the potential at the  $-c$ -axis end of the NW is positive.<sup>16,17</sup> The piezoelectric potential in semiconductor materials is the basis of piezotronics and piezo-phototronics.

### 1.2. Piezotronics

The simplest NW field effect transistor (FET) is a semiconductor NW sandwiched by electrodes at the two ends: one electrical contact serves as the source and the other as the drain of the device.<sup>18,19</sup> A gate voltage can be applied to the NW either through the upper gate electrode or through the substrate at the bottom of the device. By applying a driving voltage  $V_{DS}$  from the source to the drain, the carrier transport process of the NW FET can be adjusted and controlled through the external gate voltage  $V_G$ .<sup>20</sup>

If the gate voltage is substituted by the piezoelectric potential (internal potential) in the crystal, then the charge carrier transportation processing of the NW FET can be regulated and/or tuned by the application of stress to the device. In this case, the device is named a piezotronic device, which can be driven or triggered by deformation of the NW.<sup>21–24</sup> A piezoelectric potential is longitudinally created throughout the NW. For NWs subjected to compressive strain, the piezopotential continuously decreases from one end of the NW to the other end. When the NWs reach equilibrium without an applied electric field, the Fermi level in the entire NW remains unchanged. This phenomenon causes the equivalent barrier height and/or width between the ZnO and the metal electrode to rise at one end of the NW and drop at the other end. Therefore, the influence of the piezoelectric potential on the barrier heights at the drain and source is asymmetric. In summary, the piezotronic effect involves using the piezoelectric potential to adjust/control the carrier transportation properties at the junction or interface region.<sup>25,26</sup>

### 1.3. Piezo-phototronics and Piezophotonics

The discipline of piezo-phototronics was first proposed in 2010.<sup>27–29</sup> For materials that simultaneously exhibit semiconductor, photoexcitation, and piezoelectric properties, the study of the coupling between semiconductor and piezoelectric properties has formed the field of piezotronics. In addition, the well-known field of optoelectronics studies the coupling of semiconductor properties with photoexcitation properties.<sup>26,30</sup> The study of the coupling between piezoelectric characteristics and photoexcitation characteristics has formed the field of piezophotonics.<sup>31–34</sup> Further research on the coupling among semiconductor, photoexcitation, and piezoelectric properties has formed the field of piezoelectric optoelectronics, which has become the basis for the construction of new piezo-phototronics (Figure 2).<sup>35–43</sup> The main idea of the piezo-phototronic effect is using the piezoelectric potential to modulate the generation, separation, transportation, and recombination processes of the carriers at interfaces or junctions.<sup>6,27</sup> High-performance optoelectronic devices can be realized via the piezo-phototronic effect, such as solar cells, LEDs, and photodetectors.<sup>34,44–52</sup>

### 1.4. Piezoelectric Semiconductor NWs

The fundamental mechanisms of the piezotronic and piezo-phototronic effects apply to both NWs and thin films. However, NWs have great advantages over thin films due to the below reasons: First, NWs could be fabricated by wet chemical synthesis at relatively low temperatures (less than 100 °C) on any substrates with arbitrary shape at low cost and in

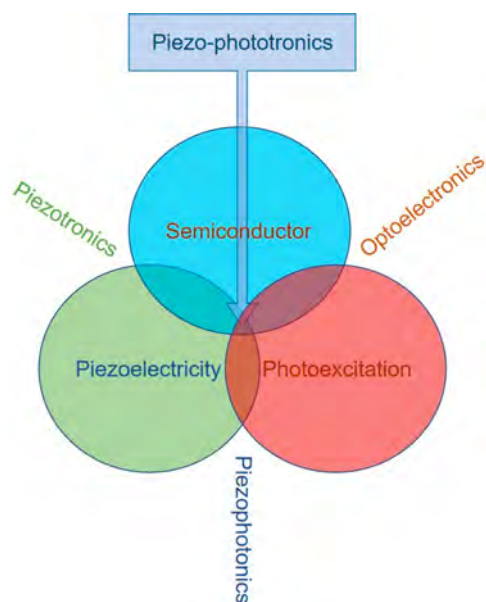


**Figure 2.** Schematic of multifield coupling: piezotronics is the coupling of piezoelectricity and semiconductivity; optoelectronics is the coupling of semiconductivity and photoexcitation; piezophotonics is the coupling of piezoelectricity and photoexcitation; and piezo-phototronics is the three-way coupling of piezoelectricity, semiconductivity, and photoexcitation. Reproduced with permission from ref 27. Copyright 2010 Elsevier Ltd.

large quantities; in contrast, the growth of thin films with high quality at low deposition temperatures is difficult. Second, because the slenderness ratio is very large and the diameter is very small, NWs are highly soft and flexible and can bear large mechanical deformation<sup>53</sup> (up to 6% deformation under applied tensile strain based on numerical calculations<sup>54</sup>) without fracture or cracking. In comparison, thin films will easily crack or break down under a smaller applied strain. Third, the small size of NWs can dramatically enhance the robustness and toughness of the NW structure such that they are almost free of fatigue. Fourth, even a very small external force can induce mechanical agitation; thus, designing ultrasensitive devices using NWs is very useful and important. Finally, NWs may have a larger piezoelectric coefficient compared to thin films.<sup>55,56</sup>

1D nanomaterials, such as NWs and nanobelts, are one of the ideal structures for research on the piezotronic and piezo-phototronic effects since they can bear a relatively large external mechanical strain/stress. Wurtzite ZnO, GaN or even doped ferroelectrics are good candidates for piezotronic applications. Until now, the most studied piezotronic and piezo-phototronic materials are ZnO NWs due to the following reasons. ZnO NWs with good crystal structure can be simply fabricated at a large quantity by using either a vapor–solid processing or wet chemical synthesis at relatively low temperature. More importantly, ZnO NWs are environmentally friendly and biologically compatible.

Normally, NWs fabricated by high-temperature vapor phase deposition techniques have fewer defects and are thus the most adequate candidates for research on piezotronics and piezo-phototronics.<sup>57,58</sup> In contrast, NWs grown by the low-temperature wet chemical approach have large concentrations of various types of defects, which are typically useful for applications in piezoelectric nanogenerators. An oxygen plasma

treatment after low-temperature fabrication of NWs can dramatically reduce the vacancy concentration, thus improving the electronic and optoelectronic properties and meeting the requirements of piezotronics and piezo-phototronics.<sup>30,51,59–63</sup>

## 2. SYNTHESIS OF PIEZOELECTRIC SEMICONDUCTOR NWS

### 2.1. Wet Chemical Synthesis

Wet chemical methods refer to the synthetic methods in which a liquid phase participates in a chemical reaction for the preparation of a material, such as chemical liquid deposition, electrochemical deposition, sol–gel processing, and hydrothermal synthesis. The principle of a wet chemical process is to select one or several required soluble metal salts or oxides and prepare the solution according to the composition of the target materials.<sup>64–66</sup> In the solution, the elements are in an ionic or molecular state. After a suitable precipitant is applied or crystallization is induced by evaporation, sublimation, or hydrolysis, the metal ions uniformly precipitate or crystallize to form nanomaterials. For the wet chemical synthesis of nanomaterials, there are several key techniques that can be used to control the size of the nanomaterials. The first one is separating the nucleation process from the growth process to control the solution concentration according to the formation of grains, such as accelerating the nucleation, generating a heterogeneous nucleus, adding a chelating agent, and/or using a saturated quenching technique. The second one is suppressing agglomeration. During the liquid phase reaction stage, agglomeration can be suppressed by forming an electric double layer or adding a protective agent. Moreover, the spray drying, freeze-drying, or supercritical gas drying techniques can effectively prevent grain growth in dry processing. The third technique is selecting a proper chemical reaction system that can control the diffusion of the ions and growth speed of the nanomaterials.

**2.1.1. Electrochemical Deposition.** The use of electrochemical reactions is a powerful approach for the growth of uniform NWs in large quantities at low cost because the applied external electric field can serve as a powerful driving force for the chemical reaction, as demonstrated in Figure 3a.<sup>67–69</sup> However, this method requires the substrate to be electrically conductive and the deposited material to not dissolve in the acidic environment. Electrochemical deposition of ZnO typically uses  $\text{ZnCl}_2/\text{KCl}$  solution as the electrolyte, Pt as the counter electrode, and Ag/AgCl as the reference electrode. Moreover, to maintain oxygen saturation of the electrolyte, continual introduction of  $\text{O}_2$  is required.<sup>70</sup> The current–voltage ( $I$ – $V$ ) characteristic curve during NW growth is generally controlled using a standard three-electrode device.

Electrochemical deposition can be used to deposit ZnO NWs onto various substrates, such as Si, Cu (Figure 3b), or even conductive polymers, due to the low-temperature synthesis process.<sup>71</sup> In addition to  $\text{Cl}^-$ , other counteranions ( $\text{SO}_4^{2-}$ ,  $\text{NO}_3^-$ , and  $\text{CH}_3\text{COO}^-$ ) for the reduction of  $\text{O}_2$  have also been studied. Different anions show distinct coordination capabilities with the crystal planes of ZnO NWs, which means that the growth rate, morphology, and aspect ratio of the ZnO NWs can be controlled by choosing the appropriate counter-cation during the electrochemical deposition. Moreover, the bandgap of ZnO NWs can be simply changed by controlling the Zn precursor concentration during the electrochemical deposition.

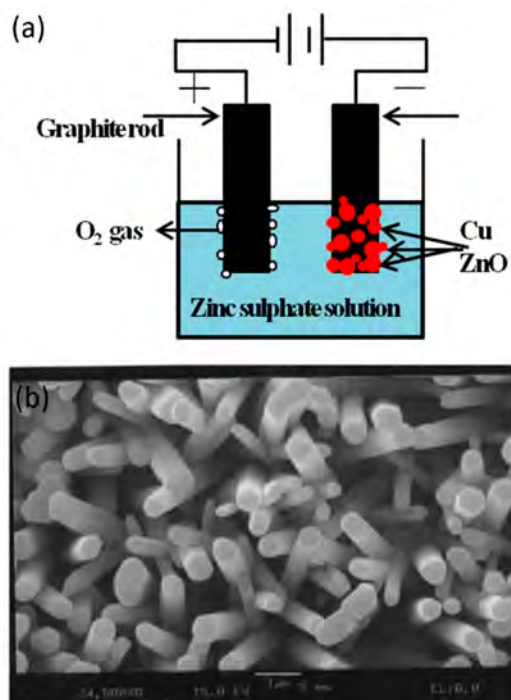


**Figure 3.** (a) Schematic illustration of the electrochemical deposition method, and (b) ZnO growth by electrochemical deposition on a Cu substrate. Reproduced with permission from ref 71. Copyright 2007 Elsevier.

**2.1.2. Hydrothermal Synthesis.** The hydrothermal synthesis method involves a chemical reaction in a fluid such as an aqueous solution or a vapor at a warm temperature and/or a high pressure. The basic principle of hydrothermal synthesis is that the solubility of hydroxides in water is higher than that of the corresponding oxide in water. Thus, hydroxides are dissolved in water, and simultaneously, oxides are precipitated. The as-prepared hydroxides can also transform into oxides under relatively high temperature and high pressure via a chemical reaction, such as a hydrolysis reaction. Hydrothermally synthesized nanomaterials have good dispersibility and little agglomeration and are well crystallized.<sup>72</sup>

ZnO NWs can be hydrothermally synthesized from zinc nitrate hexahydrate and hexamethylenetetramine.<sup>73,74</sup> Here zinc nitrate hexahydrate provides  $\text{Zn}^{2+}$  cations, and  $\text{H}_2\text{O}$  in the solution provides  $\text{O}^{2-}$  anions during the growth of ZnO NWs.<sup>75–78</sup> However, the working mechanism of hexamethylenetetramine in the chemical reaction is not yet fully understood. One possible explanation is that hexamethylenetetramine endows the solution with a weak alkalinity. Hexamethylenetetramine can hydrolyze slowly in water and continually release  $\text{OH}^-$  during the chemical reaction, which is very important for ZnO NW oriented growth. If the generation of  $\text{OH}^-$  in the solution is too fast, then  $\text{Zn}^{2+}$  cations will quickly deposit due to the high pH of the solution. Thus, the as-synthesized ZnO NWs will be poorly aligned and crystallized. Additionally, with the fast consumption of the  $\text{Zn}^{2+}$  cations in the solution, the chemical reaction will soon terminate, resulting in short ZnO NWs.

To fabricate well aligned patterned ZnO NW arrays, the preparation method needs to meet the following fundamental requirements: First, low-temperature synthesis must be performed, which allows the NWs to grow on all types of

substrates. Second, the NWs must grow along a predesigned pattern, which can be used to modulate the size, growth direction, dimensions, uniformity, and possible shape of ZnO NWs. Finally, the catalyst must be removable so that the ZnO NW-based devices can be combined with silicon-based techniques. By using electron beam exposure and hydrothermal methods at low temperature, highly oriented vertically aligned patterned ZnO NW arrays can be prepared on various inorganic substrates, including silicon and GaN (Figure 4), below 100 °C without a catalyst.<sup>16,79</sup>

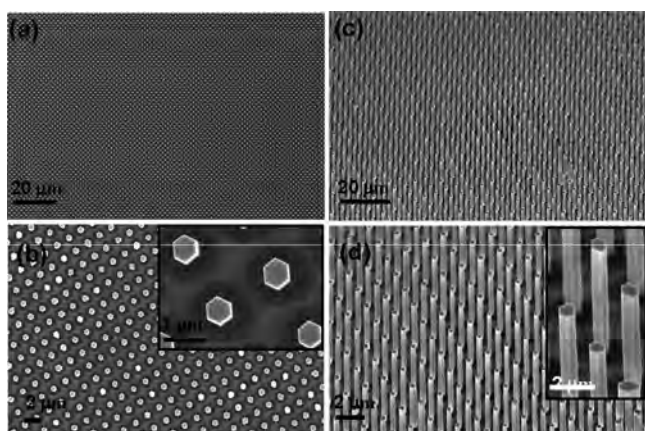


**Figure 4.** SEM images of hydrothermal epitaxial growth of vertically aligned ZnO NWs on a single crystal GaN substrate. (a and b) Top-view images of the ZnO NW array at various magnifications. (c and d) 45°-tilted-view images of well-aligned ZnO NWs under small and large magnification. Reproduced from ref 79. Copyright 2010 American Chemical Society.

Additionally, large-scale ZnO NWs can be grown on organic substrates in large quantities by hydrothermal methods. A ZnO seed layer is deposited on the substrate by magnetron sputtering at room temperature. Then, ZnO NWs can be grown at high density on the substrate on a large scale via hydrothermal methods. This approach is a ubiquitous method for ZnO growth on a variety of organic substrates.

In addition to changing the original concentrations of hexamethylenetetramine and zinc nitrate hexahydrate to control the density of ZnO NW growth on the substrate, patterned catalysts (Au, Ag, Pt) can also be used to effectively control the aspect ratio and density of ZnO NWs. Thus, the roughness of the substrate surface must be well controlled to enhance nucleation. Moreover, the orientations of the NWs are highly dependent on the surface topography of the substrate. To obtain consistent vertically oriented NWs, a suitable process must be followed to obtain a smooth substrate surface.

## 2.2. Chemical and Physical Vapor Depositions

Vapor deposition is the method of depositing high-quality materials on a substrate using physical or chemical processes occurring in the gas phase. According to the film formation mechanism, the vapor deposition techniques can be classified into chemical vapor deposition, physical vapor deposition, etc. Unlike wet chemical synthesis, vapor deposition techniques normally require a high temperature environment, expensive instruments, and comprehensive processing, but these methods can be used to fabricate various types of materials that cannot be synthesized by wet chemical synthesis, such as GaN. Furthermore, the composition of the NWs can be well

controlled by changing the deposition conditions. Although many chemical vapor deposition and physical vapor deposition techniques exist, here, we only introduce two deposition methods, chemical vapor deposition and pulsed laser deposition.

**2.2.1. Chemical Vapor Deposition.** Chemical vapor deposition can be used to grow high-quality ultralong ZnO NWs.<sup>58,80–82</sup> The oxide powder is heated in a tubular furnace, and then, steam generated by evaporation of the oxide is blown to the upper surface of the substrate by flowing Ar gas to form the desired material under the specific temperature, pressure, atmosphere, etc. The phase structure and morphology of the as-synthesized NWs are determined by various factors, such as the source materials, substrates, gas flow rate, growth temperature, temperature gradient, and pressure.<sup>83</sup> Highly oriented, vertically grown ZnO NWs can be fabricated on a single crystal sapphire substrate through chemical vapor deposition. Additionally, gold nanoparticles can be used as catalysts that excite and guide the growth of the ZnO NWs. The lattice parameters of ZnO and sapphire are very close, which makes the NWs grow vertically and well aligned on top of the sapphire substrate. During the reaction, the gold nanoparticles need to melt, form an alloy, and gradually deposit; thereby, an epitaxial ZnO NW is grown on a sapphire substrate (Figure 5). The growth rate of the NWs should be

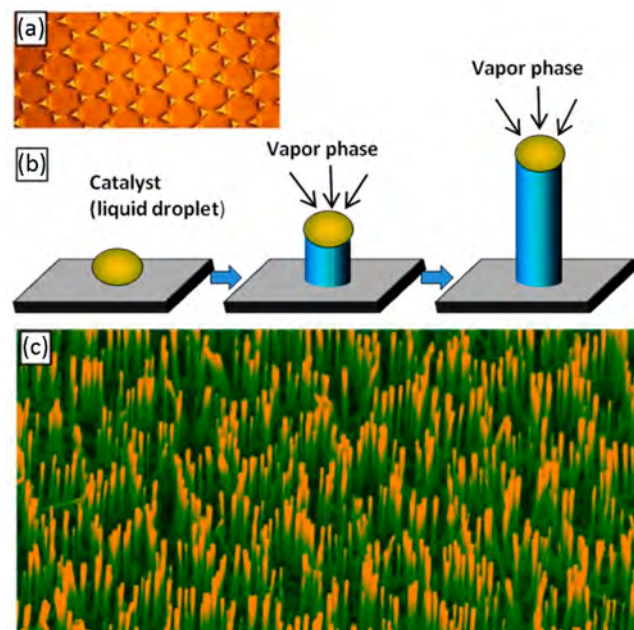


**Figure 5.** Chemical vapor deposition of ZnO NWs on a single crystal sapphire substrate by using a Au nanodot catalyst. (a) Top-view SEM image of as-synthesized aligned ZnO NWs. (b) Schematic of the Au-catalyst-assisted chemical vapor deposition process. (c) 45°-tilted-view SEM image of honeycomb-patterned ZnO NWs. Reproduced from ref 58. Copyright 2004 American Chemical Society.

moderately regulated, and thus, a low fabrication temperature can be utilized to decrease the vapor concentration. After the chemical vapor deposition, the gold nanoparticles will be on top of the ZnO NWs.<sup>84</sup>

Uniform and oriented ZnO NWs can be fabricated on GaN, AlN, AlGaIn, and sapphire substrates by chemical vapor deposition.<sup>58,85</sup> Here the crystal structure of the substrate has an important impact on the growth orientation of the ZnO

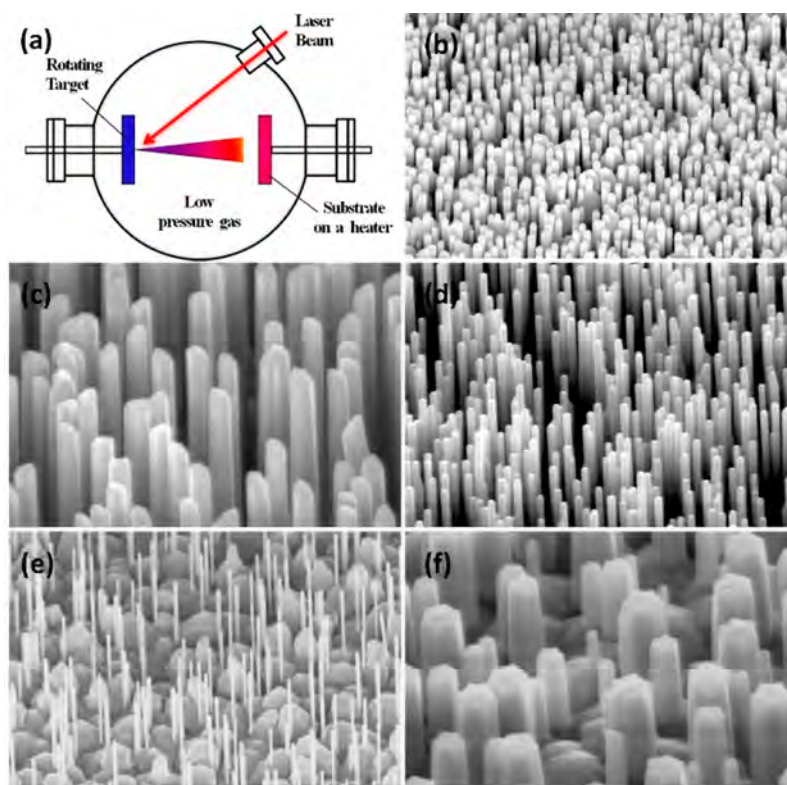


**Figure 6.** (a) Schematic illumination of the pulsed laser deposition method and SEM images of ZnO NWs grown by pulsed laser deposition with the substrate temperature at (b) 750 °C, (c) 800 °C, and (d) 850 °C. The growth pressure was fixed at 5 Torr. (e), (f) ZnO NW array deposited at 6.0 and 4.0 Torr; here, the deposition temperature of the substrate was 800 °C. Reproduced from ref 91. Copyright 2009 American Chemical Society.

NWs. The epitaxial relationship between the substrate and the NWs determines the growth direction of the NWs. The alignment quality of the NWs is controlled by many factors. Through systematic research on the effects of various growth conditions, three basic factors were found: oxygen partial pressure, intracavity pressure, and catalyst thickness.

**2.2.2. Pulsed Laser Deposition.** Since the successful fabrication of high-quality superconducting thin films, pulsed laser deposition has become a common method for growing epitaxial thin films.<sup>86</sup> Pulsed laser deposition can be used to deposit many types of films, such as complex oxides, nitrides, metals, and multilayer superlattices. When pulsed laser deposition is used for the growth of ZnO NWs, a KrF excimer laser is selected as the excitation source to bombard the ceramic target (ZnO ceramic target). The high energy of the laser transforms the ZnO ceramic into a plasma that finally deposits on the top surface of a single crystal substrate (as shown in Figure 6a). Before the NWs are grown, a textured ZnO buffer layer needs to be prepared on the single crystal substrate, which is the key to the fabrication of vertically oriented ZnO NWs.<sup>87–90</sup>

The morphology of the NW array can be tuned by the following factors: temperature of the substrate, gas pressure during growth, gas composition, gas flow rate, and pulse frequency and intensity of the laser. Scanning electron micrographs of ZnO NWs prepared at different substrate temperatures under a laser pulse frequency of 5 Hz, a 6:1 argon gas and hydrogen gas mixture, and a total gas pressure of 5 Torr are shown in Figure 6.<sup>91</sup> When the substrate temperature is 700 °C, a ZnO film with a rough surface is grown. When the temperature is raised to 750 °C, ZnO NWs with a typical

length of approximately 800 nm are formed. Longer ( $2\sim 3\ \mu\text{m}$ ) ZnO NWs are fabricated at 800 °C. When the temperature is further increased to 850 °C, some NWs merge together. The effect of the gas pressure on the aspect ratio of the NWs was investigated for a fixed substrate temperature of 800 °C. When the growth gas pressure is raised to 6 Torr, slimmer NWs are obtained. In contrast, when the gas pressure is dropped to 4 Torr, larger diameter NWs can be formed. The length and aspect ratio of the NWs can be adjusted by controlling the substrate temperature and growth gas pressure.

### 2.3. Top-Down Fabrication

All previous fabrication methods can be categorized as bottom-up methods, which means that the NWs are grown on a substrate. However, the bottom-up growth of large-scale NWs has some shortcomings, such as the nonuniform height, diameter, and composition. For applications, fabricating NWs with the same performance is very important. In contrast to bottom-up methods, another means to fabricate NWs is the top-down method, which is well used in the semiconductor industry. By employing patterning and inductively coupled plasma (ICP) techniques, highly uniform and well-oriented NWs are fabricated from a high-quality epitaxial single crystal film (Figure 7).<sup>92–95</sup>

An InGa<sub>2</sub>N/GaN multiple quantum well (MQW) multilayer was deposited on a c-plane single crystal sapphire substrate by using metal organic chemical vapor deposition (MOCVD). From bottom to top, it first consisted of a 2 μm GaN buffer layer, a 3 μm n-type GaN layer, five sets of InGa<sub>2</sub>N/GaN (3 nm/12 nm) quantum well layers, and a 100 nm p-type GaN capped layer. To fabricate patterned NWs, a large-area Ni dot

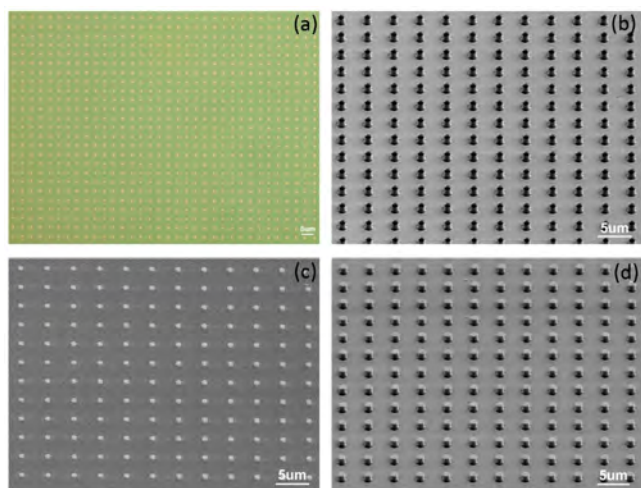


**Figure 7.** Top-down fabrication process. (a) Large-area Ni dot matrix, (b) ICP etching of thin films, in which the Ni dot matrix serves as a protective material, (c) multiple quantum well pillar array after removing the Ni dot pattern, and (d) transparent PMMA filling in the gaps of the pillar array. Reproduced from ref 96. Copyright 2015 American Chemical Society.

matrix with a diameter of 800 nm and a period of 4  $\mu\text{m}$  was first photolithographically patterned. Then, the MQW film was etched using the ICP etching technique. The MQW film under the Ni metal mask remained, while the exposed part was etched. The height of the etched MQW pillar was 1.2  $\mu\text{m}$ . The remnant Ni dot matrix could be easily removed by sulfuric acid. Finally, a 2.5  $\mu\text{m}$  thick PMMA layer was spin-coated to fill in the area around the MQW pillars. By using the top-down technique, the height, diameter, and composition of each pillar are nearly the same.<sup>96</sup>

In summary, three categories of synthesis methods have been introduced here. Among them, wet chemical synthesis is the least expensive method in terms of both equipment and materials. The fabrication temperature is either at room temperature or less than 100  $^{\circ}\text{C}$ , which is important for energy savings and direct fabrication on flexible polymer substrates. In addition, under different synthesis conditions, the morphology of the as-synthesized NWs can be widely modified. However, the quality of these low-temperature synthesized NWs may be poor compared to high temperature-fabricated ones due to the abundant defects. For the vapor deposition methods, a high synthesis temperature is always required. Chemical vapor deposition is suitable for either laboratorial or industrial continuous fabrication. The growth rate of chemical vapor deposition is fast, which is good for long NW growth. Pulsed laser deposition is a typical laboratorial growth method due to the limited size of the growth area. The crystal quality of the NWs fabricated by this method is good and easily reproducible under fixed growth conditions. However, the cost is relatively high. Top-down fabrication is the most expensive method because it requires many types of large-scale equipment and complicated techniques. However, this method is compatible with state-of-the-art semiconductor fabrication processes for large-scale fabrication. The quality and uniformity of the NWs are very good. NW arrays can be well designed and realized with nearly the same height, diameter, and periodicity, which makes this method one of the best for fabricating high-quality NW-based electronic or optoelectronic device arrays.

### 3. MECHANISMS OF PIEZOTRONICS AND PIEZO-PHOTOTRONICS

#### 3.1. Piezotronic Transistors vs Traditional Field Effect Transistors

To demonstrate the basic application concepts of piezotronics, we begin with traditional metal oxide semiconductor FETs (MOS-FETs). Figure 8a shows a schematic of a classic n-

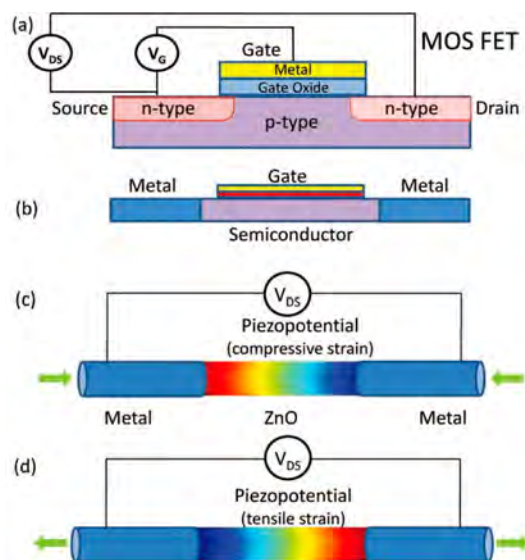


**Figure 8.** Structural comparison of (a) a MOS-FET, (b) an NW-based FET, and a piezotronic transistor under external (c) compressive strain or (d) tensile strain. Reproduced with permission from ref 97. Copyright 2011 John Wiley and Sons.

channel MOS-FET, which includes two n-type doped areas (source and drain), an ultrathin insulating oxide layer on top of the p-type area that acts as a gate material and an upper metal contact that serves as a gate.<sup>97</sup> The external voltage  $V_{\text{DS}}$  can control the current between the drain and the source, thus controlling the width of the channel that transports the charge carriers. Similarly, for a single-channel semiconductor NW-based FET (Figure 8b), the source and drain are two metal electrodes on both sides of the NWs. In this case, two methods can be used to apply the gate voltage to the NW FET: from the bottom substrate and from the insulator layer on top of the NW.

The NW-based piezotronic transistor has a simple metal-NW-metal structure, for example, Ag-ZnO-Ag or Pt-ZnO-Pt, as demonstrated in Figure 8c and 8d.<sup>97</sup> The basic mechanism of the NW-based piezotronic transistor is to tune carrier transportation at the metal–semiconductor (M–S) interface by changing the local contact barrier through the piezoelectric charges which is induced by applying strain to the ZnO NW. This structure has the following differences from the traditional CMOS. First, the applied external gate voltage is substituted by the internal piezoelectric potential through the piezoelectric effect, and therefore, the gate electrode is no longer required. In other words, the piezotronic transistor has only two ends: source and drain. Second, the controls at the M–S interface substitute the modulation through the channel width of the semiconductor. Because the current transmitted to the M–S interface can be considered an index of the local barrier height under external reverse bias, the nonlinear effect causes the on/off ratio to be quite high. Finally, the voltage control electronic

devices are replaced by external stress/strain control devices that may complementarily broaden the application area of MOS devices.

When a ZnO NW device is in a strained state, generally two types of effects can tune the carrier transportation processing. One type is the piezoresistive effect, which alters the bandgap, the density of charge carriers, and the states density in the conduction band when the semiconductor NW is subjected to an applied external strain. The piezoresistive effect is a symmetric effect at both ends of a NW without polarization and cannot be used to realize a transistor. The piezoresistive effect can be found in any semiconductor, such as GaAs, Si, and wurtzite semiconductors.<sup>98–100</sup> The other one is the piezoelectric effect from the inner polarization of the crystal, which is asymmetric.<sup>51</sup> In contrast to the piezoresistive effect, the piezoelectric effect is not a symmetrical effect through the local contacts at the drain and source due to the polarity arising from the piezoelectric potential. Normally, a negative piezoelectric potential increases the local barrier height of the contact between an n-type semiconductor, and a metal may thus change the Schottky contact to the “insulator” contact and Ohmic contact to the Schottky one.<sup>21</sup> In contrast, a positive piezoelectric potential can reduce the barrier height, thus possibly changing the Schottky junction to an Ohmic contact. However, the change of the local barrier height relies on the doping density and type of the semiconductor NW. Piezocharges are generated at both sides of the NW, which can directly control the local contacts. The piezoelectric effect in semiconductor materials not only occurs in wurtzite structure materials, such as ZnO, GaN, AlN, and PbS but also can arise in other piezoelectric semiconductor families.<sup>101–103</sup> More importantly, the polarization direction of the piezoelectric potential can be reversed simply by changing the compressive strain to a tensile strain. Therefore, a piezotronic device can be switched from drain controlled to source controlled by changing the direction of the external strain which is applied to the NW device.

### 3.2. Theoretical Framework of Piezotronics

Piezotronics can be considered as the coupling between semiconductor properties and piezoelectric properties. Thus, the fundamental functions in both semiconductor physics and piezoelectric theory should be taken into account, including the electrostatic, current–density, and continuity functions, which introduce not only static but also dynamic transport properties of carriers in either semiconductor materials or junctions,<sup>104</sup> and the piezoelectric equations, which introduce the mechanical–electric relationship of a piezoelectric material under external strain.<sup>105</sup>

The Poisson function is the fundamental equation to describe the electrostatic properties of charges:

$$\nabla^2 \psi_i = -\frac{\rho(r)}{\epsilon_s} \quad (1)$$

where  $\psi_i$  is the electric potential distribution,  $\epsilon_s$  is the permittivity of the material and  $\rho(r)$  is the charge density distribution.

The current–density equations give the relationship of the charge densities, local fields, and local currents:

$$\begin{cases} J_n = q\mu_n nE + qD_n \nabla n \\ J_p = q\mu_p pE - qD_p \nabla p \\ J_{\text{cond}} = J_n + J_p \end{cases} \quad (2)$$

where  $J_p$  and  $J_n$  are the current densities of holes and electrons, respectively,  $E$  is the electric field,  $q$  is the quantity of electric charge,  $\mu_p$  and  $\mu_n$  are the mobilities of holes and electrons, respectively,  $p$  and  $n$  are the concentrations of free holes and electrons,  $D_p$  and  $D_n$  are the diffusion coefficients for holes and electrons, respectively, and  $J_{\text{cond}}$  is the total current density.

The transport of charge under the driving of a field can be calculated by

$$\begin{cases} \frac{\partial n}{\partial t} = G_n - U_n + \frac{1}{q} \nabla \cdot J_n \\ \frac{\partial p}{\partial t} = G_p - U_p - \frac{1}{q} \nabla \cdot J_p \end{cases} \quad (3)$$

where  $G_p$  and  $G_n$  are the generation rates of holes and electrons, respectively, and  $U_p$  and  $U_n$  are the recombination rates of holes and electrons, respectively.

The piezoelectric property of a material can be evaluated through the polarization vector ( $P$ ) under an applied uniform external strain ( $S_{ik}$ ):

$$(P)_i = (e)_{ijk} (S)_{jk} \quad (4)$$

where the piezoelectric tensor  $(e)_{ijk}$  is a third-order tensor.

The relationship between electricity and elasticity through the piezoelectric effect can be given as

$$\begin{cases} \sigma = c_E S - e^T E \\ D = e S + k E \end{cases} \quad (5)$$

where  $D$  is the electric polarization,  $\sigma$  is the stress tensor,  $c_E$  is the elastic tensor, and  $k$  is the dielectric tensor.

The above fundamental equations can be calculated with specific boundary conditions for various heterostructure contacts. For NW cases, we first simplify that the drain and source of NW piezotronic devices are perfect ohmic contacts. In this case, the Dirichlet boundary conditions can be used for the electric potential and carrier concentration in the calculation. Additionally, an external strain applied to the interface of the NW junction does not generate shear strain.

**3.2.1. NW p–n Junctions.** The p–n junction is one of the most fundamental units in current electronic devices. The fundamental equation of the current–voltage ( $I$ – $V$ ) characteristics of p–n junctions can be calculated by using Shockley theory. In our case, the p-type semiconductor material is nonpiezoelectric, while the n-type semiconductor material is piezoelectric. Here, we choose ZnO as a representative of piezoelectric semiconductors. ZnO grows along its  $c$ -axis direction. When compressive stress is applied along the  $c$ -axis of ZnO, positive charges are generated at the p–n junction. In this case, the piezoelectric charges can be considered as induced charges at the surface of bulk piezoelectric materials since the area within which the piezoelectric polarization charge distributes is far smaller than the area of the bulk piezoelectric material; thus, we can consider that the piezoelectric charges are only distributed at the surface without thickness for simple calculation. In contrast, this assumption cannot be applied to NWs or even microwires. Here, we

consider that the induced piezoelectric charges are distributed at the contact area of the ZnO NW p–n junction over a width of  $W_{\text{piezo}}$ , as shown in Figure 9a.

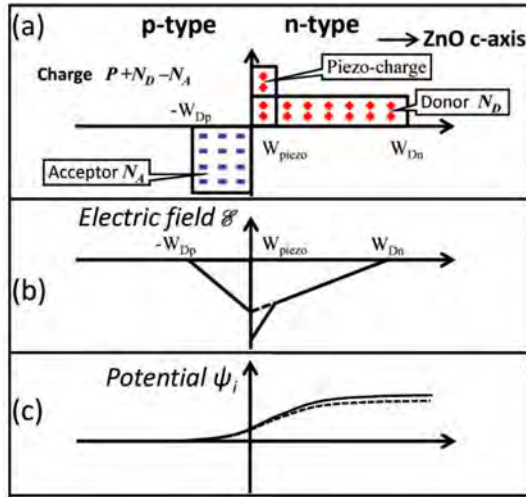


**Figure 9.** Piezoelectric semiconductor NW-based p–n junction with/without piezoelectric charges at thermal equilibrium. (a) Distribution of acceptor, donor, and piezoelectric charges; (b) electric field; and (c) potential distributions affected by piezoelectric charges at the interface of the p–n junction. The dashed and solid lines indicate the cases without/with the presence of piezoelectric charges at the interface of the p–n junction, respectively. Reproduced with permission from ref 97. Copyright 2011 John Wiley and Sons.

Figure 9a depicts the abrupt junction model that considers the impurity concentration in the NW p–n junction area to abruptly switch from the acceptor concentration  $N_A$  to the donor concentration  $N_D$ . The electrons and holes at the interface area generate a charge depletion area, which is considered to have a box profile. Here, the piezoelectric potential distribution and related electric field in the p–n junction can be calculated for a one-dimensional NW device, so the Poisson eq (eq 1) can be simplified as follows:

$$-\frac{d^2\psi_i}{dx^2} = \frac{dE}{dx} = \frac{\rho(x)}{\epsilon_s} = \frac{1}{\epsilon_s}[qN_D(x) - qn(x) - qN_A(x) + qp(x) + q\rho_{\text{piezo}}(x)] \quad (6)$$

where  $N_{A(x)}$  is the acceptor concentration,  $N_{D(x)}$  is the donor concentration, and  $\rho_{\text{piezo}(x)}$  is the polarization charge density.  $W_{Dn}$  and  $W_{Dp}$  are the widths of the depletion layers on the n-side and the p-side, respectively. Then, the electric fields at different positions can be calculated by combining these equations, as demonstrated in Figure 9b:

$$E(x) = -\frac{qN_A(x + W_{Dp})}{\epsilon_s}, \text{ for } -W_{Dp} \leq x \leq 0 \quad (7a)$$

$$E(x) = -\frac{q[N_D(W_{Dn} - x) + \rho_{\text{piezo}}(W_{\text{piezo}} - x)]}{\epsilon_s}, \text{ for } 0 \leq x \leq W_{\text{piezo}} \quad (7b)$$

$$E(x) = -\frac{qN_D(W_{Dn} - x)}{\epsilon_s}, \text{ for } W_{\text{piezo}} \leq x \leq W_{Dn} \quad (7c)$$

Thus, the maximum electric field  $E_m$  at the interface ( $x = 0$ ) is given by

$$|E_m| = \frac{q(N_D W_{Dn} + \rho_{\text{piezo}} W_{\text{piezo}})}{\epsilon_s} \quad (8)$$

In addition, the potential distribution  $\psi_i(x)$  can be expressed as (as shown in Figure 9c):

$$\psi_i(x) = \frac{qN_A(x + W_{Dp})^2}{2\epsilon_s}, \text{ for } -W_{Dp} \leq x \leq 0 \quad (9a)$$

$$\psi_i(x) = \psi_i(0) + \frac{q\left[N_D\left(W_{Dn} - \frac{x}{2}\right)x + \rho_{\text{piezo}}\left(W_{\text{piezo}} - \frac{x}{2}\right)x\right]}{\epsilon_s}, \text{ for } 0 \leq x \leq W_{\text{piezo}} \quad (9b)$$

$$\psi_i(x) = \psi_i(W_{\text{piezo}}) - \frac{qN_D}{\epsilon_s}\left(W_{Dn} - \frac{W_{\text{piezo}}}{2}\right)W_{\text{piezo}} + \frac{qN_D}{\epsilon_s}\left(W_{Dn} - \frac{x}{2}\right)x, \text{ for } W_{\text{piezo}} \leq x \leq W_{Dn} \quad (9c)$$

Thus, the built-in potential  $\psi_{bi}$  can be calculated as

$$\psi_{bi} = \frac{q}{2\epsilon_s}(N_A W_{Dp}^2 + \rho_{\text{piezo}} W_{\text{piezo}}^2 + N_D W_{Dn}^2) \quad (10)$$

From the above equations, the change in the built-in potential derives from the piezoelectric charges generated through the applied strain. Here, the sign of the local piezoelectric charges is determined by tensile or compressive strain. Obviously, the piezoelectric potential can effectively tune the band of the junction corresponding to the Fermi levels.

Shockley theory is now used to calculate the  $I$ – $V$  characteristics of the piezoelectric NW-based p–n junction, which analyze the ideal p–n junction based on the following hypotheses: (1) Piezoelectric semiconductor NWs are not degenerate, so the Boltzmann approximation can be applied. (2) An incoherent depletion layer exists at the piezoelectric NW-based p–n junction. (3) A generation and recombination current does not exist in the depletion layer, and the hole and electron currents are constant over the entire NW p–n junction. (4) The majority carrier concentration is much greater than the injected minority one. When the width of the piezoelectric charge region is less than that of the depletion area ( $W_{\text{piezo}} \ll W_{Dn}$ ), the tuning of the NW energy band through piezoelectric charges at the p–n junction can only serve as a perturbation. In this case, eq 2 can be used to calculate the total current density by

$$J = J_n + J_p = J_0 \left[ \exp\left(\frac{qV}{kT}\right) - 1 \right] \quad (11)$$

and the saturation current can be calculated as

$$J_0 = \frac{qD_p p_{no}}{L_p} + \frac{qD_n n_{po}}{n}$$

where  $L_n$  and  $L_p$  are the diffusion lengths of holes and electrons, respectively;  $n_{po}$  and  $p_{no}$  are the electron concentration inside the p-type semiconductor and the hole concentration inside the n-type semiconductor at thermal

equilibrium, respectively. Thus, the intrinsic carrier density  $n_i$  can be calculated as

$$n_i = N_C \exp\left(-\frac{E_c - E_i}{kT}\right) \quad (12)$$

where  $E_i$  represents the intrinsic Fermi level,  $N_C$  is the effective density of states in the conduction band, and  $E_c$  represents the bottom edge of the conduction band.

To simplify the case, we assume an abrupt junction with donor concentration  $N_D$  at the n-type side and locally  $p_{n0} \gg n_{p0}$ ; thus, we can calculate the total current density by

$$\begin{aligned} J &= J_0 \left[ \exp\left(\frac{qV}{kT}\right) - 1 \right] \\ &= \frac{qD_p n_i}{L_p} \exp\left(\frac{E_i - E_F}{kT}\right) \left[ \exp\left(\frac{qV}{kT}\right) - 1 \right] \end{aligned} \quad (13)$$

Without a piezopotential at the interface of the epidemic p–n junction, the relationship of the saturated current density ( $J_{co}$ ) and Fermi Level ( $E_{F0}$ ) can be expressed as

$$J_{co} = \frac{qD_p n_i}{L_p} \exp\left(\frac{E_i - E_{F0}}{kT}\right) \quad (14)$$

From eqs 9–10, we can obtain the Fermi level ( $EF$ ) with a piezopotential at the interface of the p–n junction as follows:

$$E_F = E_{F0} - \frac{q^2 \rho_{piezo} W_{piezo}^2}{2\epsilon_s} \quad (15)$$

Combining eqs 14 and 15 with eq 13, the  $I$ – $V$  characteristics of the piezoelectric NW-based p–n junction can be derived as<sup>97</sup>

$$J = J_{co} \exp\left(\frac{q^2 \rho_{piezo} W_{piezo}^2}{2\epsilon_s kT}\right) \left[ \exp\left(\frac{qV}{kT}\right) - 1 \right] \quad (16)$$

From eq 16, the current transport through the NW p–n junction is a functional of the piezoelectric charges, whose sign depends on the direction of the strain. Thus, both the magnitude and sign of the external strain (tension or compression) can be used to effectively adjust or control the transport current. This phenomenon is the basic working mechanism of a piezotronic transistor based on a p–n junction.

**3.2.2. Metal–Semiconductor Schottky Contact.** The metal–semiconductor contact is another typical heterostructure in the electronic devices. In the case when the work function of a metal is different from the electron affinity of the semiconductor, a Schottky barrier (SB) ( $e\phi_{SB}$ ) will be formed at the junction interface (Figure 10a).<sup>27</sup> When the Schottky barrier is too low, the M–S junction is called an ohmic contact, which conducts current in both directions without rectification. In contrast, when the Schottky barrier is sufficiently high, a current cannot pass the barrier unless the external voltage is greater than the threshold value ( $\phi_i$ ). In this case, the M–S junction is called a Schottky contact.

When a strain is applied to a semiconductor NW along its longitudinal direction and the semiconductor simultaneously exhibits the piezoelectric effect, a negative piezoelectric potential is realized at the semiconductor side, which can dramatically increase the local Schottky barrier height (SBH)

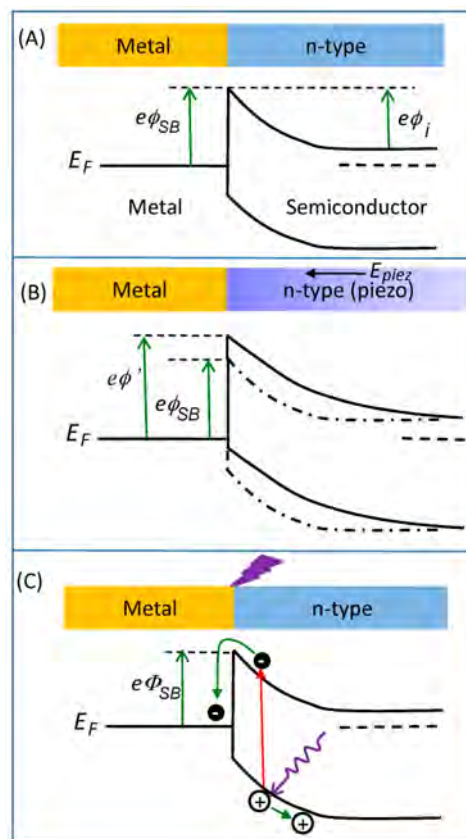


**Figure 10.** Schematic diagram of the energy band of an M–S Schottky contact with coupling modulation by laser excitation and piezoelectric charges. (a) Band diagram of an M–S contact; (b) band diagram of an M–S contact with coupling of the external strain-induced piezopotential; and (c) band diagram of an M–S contact under laser excitation. Reproduced with permission from ref 27. Copyright 2010 Elsevier Ltd.

to  $e\phi'$  (Figure 10b);<sup>27</sup> conversely, a positive piezopotential can reduce the SBH. The induced piezoelectric potential can efficiently modulate local Schottky contact by the magnitude of the strain and the piezoelectric constant of the piezoelectric semiconductor. Therefore, the charge carrier transportation processing at the M–S junction can be modulated. When switching the applied strain to a semiconductor NW from a tensile one to a compressive one, the local Schottky contact properties can also be changed because the sign of the external strain is reversed.<sup>23</sup> Thus, the charge transportation at the interface of a Schottky contact can be controlled by the strain induced piezoelectric potential, working as a gate effect. Such modulation is the fundamental mechanism of the piezotronics in a Schottky contact. Besides, at the interface of a Schottky contact, photoexcitation can generate electrons in the conduction band. These electrons prefer to move away from the interface, and at the same time, holes prefer to move toward the contact from the semiconductor. These accumulated holes can thus modulate the local barrier and lower the effective height of the Schottky barrier (Figure 10c); as a result, the conductance increases.

As ohmic M–S contacts do not have rectification characteristics, here, we only discuss M–S Schottky contacts. Similar to the previous discussion on piezoelectric NW-based p–n junctions, an M–S Schottky contact can be simplified as a charge distribution without thickness, as shown in Figure 11,

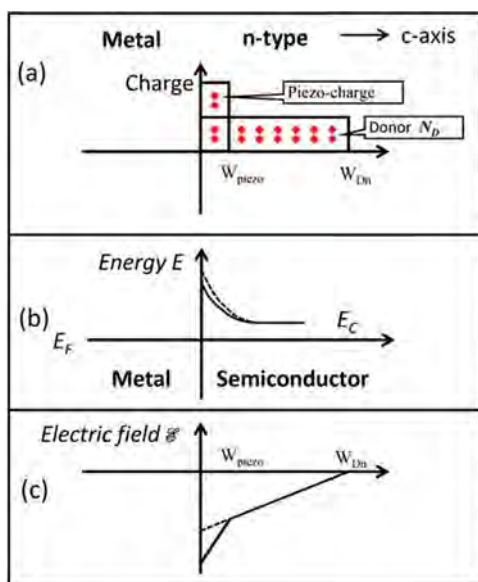


**Figure 11.** Piezoelectric semiconductor-based M–S Schottky contact with piezoelectric charges at thermal equilibrium. (a) Space charge distributions; (b) energy band diagram; and (c) electric field affected by the piezoelectric charges at the interface. The dashed and solid lines indicate the cases without/with piezoelectric charges at the interface of the M–S Schottky contact, respectively. Reproduced with permission from ref 97. Copyright 2011 John Wiley and Sons.

with a Schottky barrier at the junction area. It is assumed that the semiconductor side is n-type; for simplification, the surface states as well as other anomalies are not considered. Upon an applied external strain, the piezoelectric charges are generated at the interface of Schottky contacts and change both the height and the width of the Schottky barrier. Unlike the traditional means of changing the SBH by applying a dopant on the semiconductor side, the piezoelectric potential can be used to continuously adjust the SBH through the strain applied to a fabricated device.<sup>106–109</sup>

For a Schottky contact, the  $I$ – $V$  characteristics under forward bias according to the Schottky diffusion theory can be expressed as<sup>104</sup>

$$J_n \approx J_D \exp\left(-\frac{q\phi_{Bn}}{kT}\right) \left[ \exp\left(\frac{qV}{kT}\right) - 1 \right] \quad (17)$$

where

$$J_D = \frac{q^2 D_n N_c}{kT} \sqrt{\frac{2qN_D(\psi_{bi} - V)}{\epsilon_s}} \exp\left(-\frac{q\phi_{Bn}}{kT}\right)$$

where  $\psi_{bi0}$  and  $\phi_{Bn0}$  are the built-in electric potential and SBH when no piezoelectric charges exist at the interface of the p–n junction, respectively. Here, the piezoelectric charges are assumed to function as a perturbation to the conduction band edge  $E_C$ . In this case, the change in the SBH arising from the tuning of the piezoelectric charges can be calculated using eqs 9a–9c and 10:

$$\phi_{Bn} = \phi_{Bn0} - \frac{q^2 \rho_{\text{piezo}} W_{\text{piezo}}^2}{2\epsilon_s} \quad (18)$$

Thus, the current density of the piezoelectric M–S Schottky contact can be obtained:

$$J_n \approx J_{D0} \exp\left(\frac{q^2 \rho_{\text{piezo}} W_{\text{piezo}}^2}{2\epsilon_s kT}\right) \left[ \exp\left(\frac{qV}{kT}\right) - 1 \right] \quad (19)$$

Therefore, the current flowing through the M–S contact can be considered an exponential function of the piezoelectric charge at the junction area. Here, the polarity is dependent on the type of strain. Thus, both the magnitude and the sign (tension and compression) of the strain can be used to effectively adjust or control the transmitted current. This is the basic working mechanism of a piezotronic transistor based on the M–S Schottky contact.

**3.2.3. Metal–Wurtzite Semiconductor Contact.** We now use the above results to investigate the experimentally well-studied metal–wurtzite semiconductor contacts, for example, a Au–ZnO NW. The piezoelectric coefficient matrix of wurtzite structure ZnO can be written as

$$(e)_{ijk} = \begin{pmatrix} 0 & 0 & 0 & 0 & e_{15} & 0 \\ 0 & 0 & 0 & e_{15} & 0 & 0 \\ e_{31} & e_{31} & e_{33} & 0 & 0 & 0 \end{pmatrix}$$

As the easy axis of ZnO is the  $c$ -axis, normally, the longitudinal direction of a ZnO NW is along the  $c$ -axis; in this case, the piezoelectric polarization of the ZnO NW at the contact can be obtained as

$$P_z = e_{33} s_{33} = q \rho_{\text{piezo}} W_{\text{piezo}} \quad (20)$$

The current density is as follows:

$$J = J_{D0} \exp\left(\frac{q e_{33} s_{33} W_{\text{piezo}}}{2\epsilon_s kT}\right) \left[ \exp\left(\frac{qV}{kT}\right) - 1 \right] \quad (21)$$

Thus, the current transported across the M–S interface at the ZnO NW-based semiconductor contact is an exponential function of the external strain (magnitude and sign) along the  $c$ -axis, which means that the current of the metal–wurtzite semiconductor contact can be turned on or off by tuning the magnitude and sign of the strain.

We performed numerical calculations using eq 21. We chose the material constants as follows: the piezoelectric constant of ZnO is  $e_{33} = 1.22$  C/m<sup>2</sup>, the relative dielectric constant is  $\epsilon_s = 8.91$ , the width of the piezoelectric charges is assumed to be  $W_{\text{piezo}} = 0.25$  nm, and the temperature ( $T$ ) is fixed at 300 K. Figure 12a demonstrates the calculated results of the externally applied voltage  $V$ -tuned  $J/J_{D0}$  at the M–S interface under various external strains, clearly showing that the strain can dramatically modulate the transport current. When the applied strain changes from  $-1\%$  to  $1\%$ ,  $J/J_{D0}$  decreases over 500% under a fixed external forward bias of  $V = 0.5$  V, as shown in Figure 12b. The calculation results qualitatively fit experimental data. Moreover, when the bias is reversed, the effective voltage dependence mostly derives from the variation in the SBH based on the model.

### 3.3. Theoretical Discussion of the Piezo-Phototronic Effect

#### 3.3.1. Fundamental Theory for Piezo-phototronics.

Piezo-phototronic devices, an emerging and developing concept in physics, are devices that utilize the piezopotential arising from piezoelectric semiconductors working as a “gate” voltage to modulate carrier generation, transportation, and recombination processing near the inner p–n junction.<sup>110–112</sup> Especially for piezoelectric semiconductors, for example, ZnO,

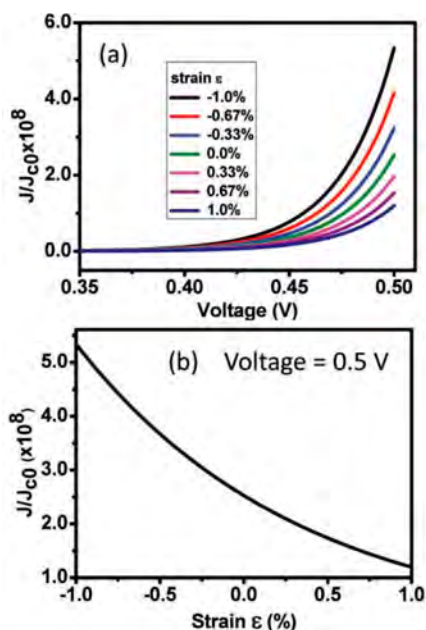


**Figure 12.**  $I$ - $V$  characteristics of an M-S Schottky contact tuned by the piezotronic effect. (a)  $I$ - $V$  curves under various strains and (b) strain-induced relative current densities under a fixed 0.5 V forward bias. Reproduced with permission from ref 97. Copyright 2011 John Wiley and Sons.

GaN, AlN, and PbS, a piezoelectric potential can be generated through an external stress, resulting from the induced piezoelectric charges from a microperspective. The presence of such piezocharges at the interface is important in altering the performance of photodetectors, light emitting diodes, or solar cells fabricated by using these materials.<sup>113–118</sup>

Semiconductor physics<sup>119</sup> and piezoelectric theory<sup>105</sup> have been employed to carefully explain the piezo-phototronic effect based on such devices. As complementary research areas, not only the static but also the dynamic transportation properties of the charge carriers as well as the interaction between electrons and photons in semiconductor materials can be analyzed based on the former, while other phenomena, such as the behavior of a piezoelectric material under dynamic strain, can be explained by the latter. To characterize piezo-phototronic devices, basic governing equations, including electrostatic, current-density, continuity, and piezoelectric equations, are indispensable and need to be balanced.

**3.3.2. Piezo-phototronic Effect in LEDs.** Precisely three main optical processes occur in a semiconductor device involving the interaction of an electron and a photon. First, after absorbing a photon, an electron may be excited from the valence band to the conduction band. This process lies at the core of developing photodetectors and solar cells. Second, as a reverse process, an electron dropping from the conduction band to the valence band can induce photon emission, which is named recombination and mainly occurs in LED devices.<sup>96,120–123</sup> Last but not least, through the recombination process, an injected photon has the potential to stimulate another similar photon and finally produce two coherent photons. The piezo-phototronic effect effectively compensates for the thermal degradation in high-power LEDs, which has significant applications in solid-state lighting.<sup>124</sup>

To visualize how the piezo-phototronic phenomenon affects the device performance, a piezoelectric NW LED is the

simplest but best choice for demonstration. Typically, the basic LED structure has an inner p-n junction (Figure 13a).<sup>62,110,125</sup> Under forward bias, excess carriers over the

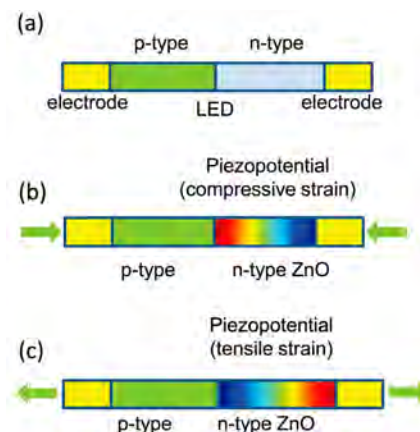


**Figure 13.** Schematic illustration of a basic LED structure with a p-n junction. Under (b) tensile or (c) compressive strain, a piezopotential distribution emerges in the proposed n-type piezoelectric NW LED device, which dramatically modulates the carrier generation, separation, and transportation characteristics. Reproduced with permission from ref 110. Copyright 2012 John Wiley and Sons.

equilibrium value will be generated, leading to radiative recombination of injected minority carriers and thus emission of light. This mechanism is also suitable for a single semiconductor NW-based LED.

A piezo-phototronic LED device is constructed with a nonpiezoelectric p-type and piezoelectric n-type heterostructure junction, where ZnO is selected as the key component for modulation (Figure 13b and 13c). With a tensile or compressive strain along the longitudinal direction, an emerging piezoelectric potential distribution is easily observed for the n-type NW. Such piezoelectric charges induced at the interface area can largely modulate the band structure of the device, thus adjusting the carrier generation, transportation, and recombination at the interface of the M-S contact or p-n junction.

Many experimental and theoretical studies have been performed on the effects of the current density and LED light intensity to realize real applications such as displays and optical communication. The optical power density  $P_{\text{optic}}$  is a nonlinear function of the current density  $J$ . For simplicity, the first order approximation can be utilized, and the correlation can be written as a power law relationship:

$$P_{\text{optic}} = \beta J^b \quad (22)$$

where  $\beta$  is a constant that depends on the materials and structure of the device, and  $b$  is a nonlinear power law parameter.

For an ideal junction,<sup>4</sup> by solving the basic eqs 1–5, the piezo-LED optical power output for an n-type abrupt junction (locally  $p_{n0} \gg n_{p0}$ ) can be derived as

$$P_{\text{optic}} = \beta \left\{ J_{c0} \exp \left( \frac{q^2 \rho_{\text{piezo}} W_{\text{piezo}}^2}{2 \epsilon_s k T} \right) \left[ \exp \left( \frac{qV}{kT} \right) - 1 \right] \right\}^b \quad (23)$$

where  $J_{c0}$  is the saturation current density.

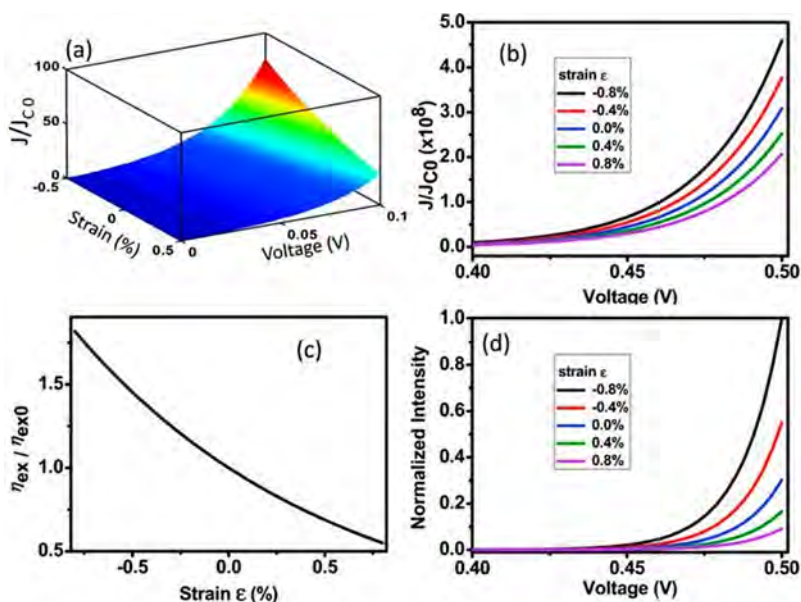


**Figure 14.** Demonstration of how an applied strain influences piezo-phototronics devices: (a) calculated relative current density variation with the externally applied voltage and strain; (b) detailed DC characteristics; (c) external strain-tuned relative external quantum efficiency; and (d) relative light intensity variation of a piezoelectric Schottky LED as a function of the applied voltage with strain ranging from  $-0.8\%$  to  $0.8\%$ . Reproduced with permission from ref 110. Copyright 2012 John Wiley and Sons.

In essence, the efficiency of an LED device depends on four distinct factors: the (1) external quantum efficiency  $\eta_{\text{ex}}$ ; (2) internal quantum efficiency  $\eta_{\text{in}}$ , which is the ratio of the number of photons emitted internally to the number of injected carriers passing through the junction; (3) power efficiency  $\eta_{\text{p}}$ ; and (4) optical efficiency  $\eta_{\text{op}}$ .

For clarity, the external quantum efficiency for the simplest cases is deduced:

$$\eta_{\text{ex}} = N_{\text{photons}}/N_{\text{elec}} \quad (24)$$

where  $N_{\text{photons}}$  and  $N_{\text{elec}}$  are the number of photons emitted from the junction and the number of carriers passing through the junction, respectively. The above equation can be rewritten as

$$\eta_{\text{ex}} = \frac{qP_{\text{optic}}}{h\nu J} \quad (25)$$

where  $h\nu$  is the emitted photon energy. Coupled with the above equation, the relationship can be abbreviated as

$$\eta_{\text{ex}} = \alpha \eta_{\text{ex}0} \quad (26)$$

where  $\eta_{\text{ex}0}$  represents the external quantum efficiency when there are no piezocharges at the interface of the p–n junction:

$$\eta_{\text{ex}0} = \frac{\beta q}{h\nu} \left\{ J_{\text{c}0} \left[ \exp\left(\frac{qV}{kT}\right) - 1 \right] \right\}^{b-1} \quad (27)$$

and  $\alpha$  is a factor describing the piezo-phototronic effect in the carrier transport and photon recombination processes:

$$\alpha = \left\{ \exp\left(\frac{q^2 \rho_{\text{piezo}} W_{\text{piezo}}^2}{2\varepsilon_s kT}\right) \right\}^{b-1} \quad (28)$$

According to eqs 7 and 11, for a piezoelectric p–n junction LED, both the LED optical power output and the external quantum efficiency have a nonlinear relationship with the local

piezocharges. Hence, such a photon emission process can be effectively affected by both the magnitude and the orientation (tensile vs compressive) of the strain, which is the general principle of a piezo-phototronic p–n junction LED.<sup>62</sup>

As for *c*-axis growth ZnO or GaN NWs, assuming that an external strain  $s_{33}$  is applied along the longitudinal direction and a nonlinear approximation,  $b = 2$ , the optical power output of a piezo-phototronic LED can be derived as

$$P_{\text{optic}} = \beta \left\{ J_{\text{c}0} \exp\left(-\frac{qe_{33}s_{33}W_{\text{piezo}}}{2\varepsilon_s kT}\right) \left[ \exp\left(\frac{qV}{kT}\right) - 1 \right] \right\}^2 \quad (29)$$

The external quantum efficiency can be expressed as

$$\eta_{\text{ex}} = \exp\left(-\frac{qe_{33}s_{33}W_{\text{piezo}}}{2\varepsilon_s kT}\right) \eta_{\text{ex}0} \quad (30)$$

where the effect factor is given by

$$\alpha = \exp\left(-\frac{qe_{33}s_{33}W_{\text{piezo}}}{2\varepsilon_s kT}\right) \quad (31)$$

Figure 14 roughly demonstrates how an external strain influences piezo-phototronics devices, and the entire calculation process was conducted using the same data as in Figure 12. The calculated  $J/J_{\text{C}0}$  strain tuned by the externally applied voltage  $V$  is demonstrated in Figure 14a. Specifically, in Figure 14b, the detailed DC characteristics of a piezo-phototronic Schottky LED with applied external strain ranging from  $-0.8\%$  to  $0.8\%$  are extracted. The relative current density clearly increases with increasing strain. The relative external quantum efficiency versus applied strain is depicted in Figure 14c, which reveals the essence of piezoelectric control/tuning of the photon emission process in a piezoelectric LED device. In addition, as an external manifestation, the light intensity improves by over 1000% with the strain change, as shown in Figure 14d.

In short, the above derivation and analytical process provides a shallow understanding of piezoelectric LED devices. Simply put, the nonradiative recombination is overlooked, which occurs throughout the entire device operation. Two types of nonradiative processes have been observed: Shockley–Read–Hall recombination and the Auger processing. The former relates to the nonradiative recombination phenomenon that occurs in the semiconductor forbidden bandgap with the help of traps, while the latter involves the energy transfer processing from the injected hole or electron to another free hole or electron. Both processes should be taken into account for an optimized operation in practice.<sup>47,113</sup>

**3.3.3. Piezo-phototronic Effect in Photodetectors.** Another influential advancement involving the interaction between electrons and photons is photodetectors. A photodetector is used to detect light or other electromagnetic radiation, which usually involves a p–n junction converting light photons into a current. As prime examples, photodiodes and phototransistors are now common in electronics used daily, such as mobile phones and smart watches. With the rise of the piezo-phototronic concept, this effect is believed to have great potential in tuning the electric performance.<sup>126,127</sup>

For a conventional photodetector, the photon intensity can be obtained by analyzing the photoinduced current. Therefore, starting the review of research in this area with a discussion of the Schottky contact current is understandable.<sup>128</sup> A one-dimensional NW model is adopted here to perform a qualitative analysis. According to semiconductor physics, for a typical n-type Schottky contact device with an M–S junction, the thermionic emission (TE) theory should be applied to determine the carrier transportation characteristics under a forward bias voltage, and the current density  $J_F$  is derived as<sup>1</sup>

$$J_F = A^* T^2 \exp\left(-\frac{q}{kT} \phi_n\right) \left[ \exp\left(\frac{qV}{kT}\right) - 1 \right] \quad (32)$$

where  $A^*$  is the Richardson constant. Nevertheless, the inadequacy of the current estimation for a reverse bias condition based on such theory inhibits accurate behavior learning. Thermionic field emission (TFE) theory is therefore proposed considering the tunneling effect, which aims to account for the behavior of heavily doped semiconductor materials.<sup>7,8</sup> Through this method, the current density under a reversed bias is featured as

$$J_R = J_{sv} \exp\left(-\frac{q}{E_0} \phi_n\right) \exp\left[V_R \left(\frac{q}{kT} - \frac{q}{E_0}\right)\right] \quad (33)$$

where  $J_{sv}$  is the slowly varying term corresponding to the Schottky barrier and external voltage,  $V_R$  is the reverse voltage,  $q$  is the electron charge,  $k$  is the Boltzmann constant, and  $E_0$  is the tunneling parameter.  $E_0$  is generally expected to remain constant with barrier height or applied external voltage variation. Thus, setting  $E_0 = akT$  with  $a > 1$  is acceptable; thereby, the equation can be rewritten as

$$J_R = J_{sv} \exp\left(-\frac{q}{akT} \phi_n\right) \exp\left[V_R \frac{q}{kT} \left(1 - \frac{1}{a}\right)\right] \quad (34)$$

Building a photoexcitation model from the ground up is highly meaningful. In photodetector devices, photons with energy higher than the bandgap ( $E_g$ ) are capable of exciting electron–hole pairs, and the excess free carrier concentration

remains constant under steady light illumination. All of these phenomena are revealed by the continuity equation:<sup>128</sup>

$$\Delta n = \Delta p = \tau_n G_L(I) \quad (35)$$

where  $\Delta n$  is the excess electron concentration and  $\Delta p$  is the excess hole concentration with light illumination,  $\tau_n$  is the lifetime of the carrier,  $G_L(I)$  is a function of the light intensity, and  $\tau_n$  is the rate of photon generation.

Within an equilibrium model, the Fermi level of the semiconductor lines up with that in the metal without photoexcitation. Once light irradiates the device, excess carriers will emerge, and the original Fermi level will split into two quasi-Fermi levels, one for holes and the other for electrons. In view of the NW structure, these quasi-Fermi levels should be uniform along the entire device if the light illumination is uniform. Referring to band theory, the quasi-Fermi level for holes and electrons can be expressed as<sup>119</sup>

$$\begin{aligned} E_{F_n} &= E_F + kT \ln\left(\frac{n_0 + \Delta n}{n_0}\right) \\ E_{F_p} &= E_F - kT \ln\left(\frac{p_0 + \Delta p}{p_0}\right) \end{aligned} \quad (36)$$

Additionally, to obtain deep insight into the piezo-phototronic effect, the semiconductor must be assumed to be piezoelectric. Undoubtedly, the Schottky barrier will be altered once piezoelectric charges appear. According to previous studies, the modification of the barrier height is derived as<sup>97</sup>

$$\Delta\phi_{\text{piezo}} = -\frac{1}{2\epsilon} \rho_{\text{piezo}} W_{\text{piezo}}^2 \quad (37)$$

Figure 15 demonstrates an ideal metal–semiconductor–metal (M–S–M) structure under the modulation of both piezoelectric charges and photoinduced charges.<sup>126</sup> The NW is assumed to exhibit a wurtzite structure along its  $c$ -axis.

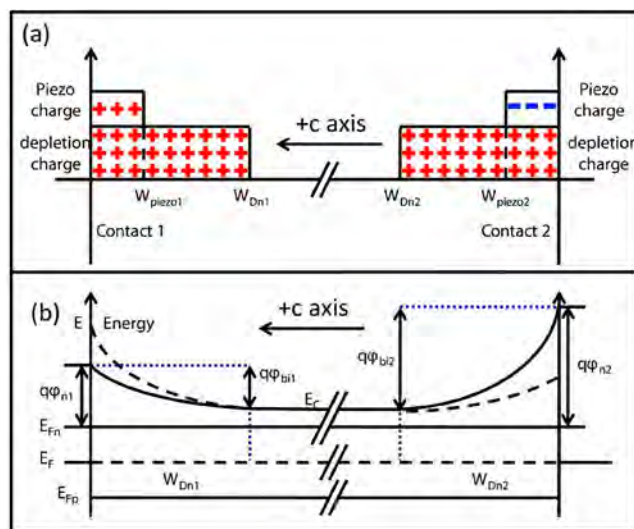


**Figure 15.** Schematic illustration of the (a) space charge distribution and (b) corresponding energy band diagram for an ideal M–S–M structure with both piezoelectric and photoinduced charges. The dashed lines represent the original Schottky barriers, while the solid lines represent the modified band structure. Reproduced with permission from ref 126. Copyright 2012 John Wiley and Sons.

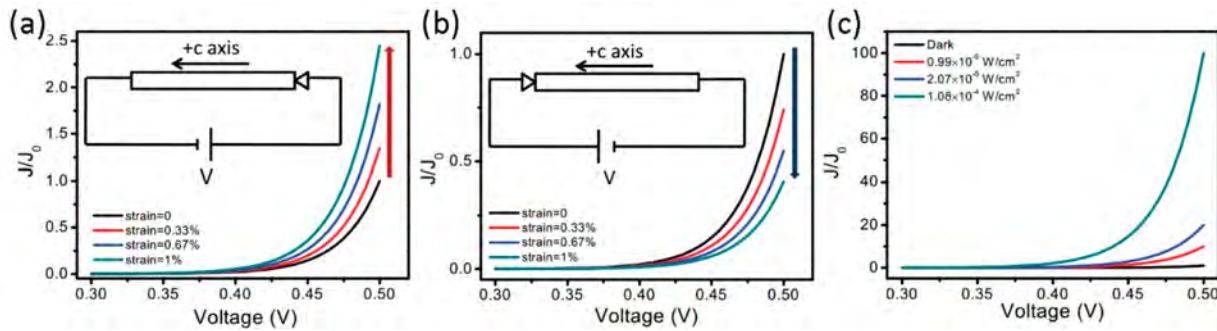


**Figure 16.** Numerical simulation based on a metal–ZnO–metal photodetector with one ohmic contact and one Schottky contact. For two different devices with opposite  $c$ -axis orientations corresponding to the Schottky contact position, the configurations and their current densities under various applied voltage and strain conditions are demonstrated in (a) and (b). (c) Diagram of relative current density versus voltage under different illumination powers without external strain. Reproduced with permission from ref 126. Copyright 2012 John Wiley and Sons.

Essentially, the piezoelectricity stems from the inner-crystal polarization of ions, which could mean that the fixed piezoelectric charges at the two NW ends have opposite signs. Figure 15a abstractly demonstrates the space charge distribution in the device. For a specific NW with strain along its  $c$ -axis, the piezo-polarization is

$$P = e_{33}^s s_{33} = \rho_{\text{piezo1}} W_{\text{piezo1}} = -\rho_{\text{piezo2}} W_{\text{piezo2}} \quad (38)$$

where  $\rho_{\text{piezo1}}$  and  $\rho_{\text{piezo2}}$  are the densities of the strain-generated piezoelectric charges at contact 1 and contact 2, respectively. The height of a Schottky barrier is determined by two factors: photoexcitation effectively reduces it, while piezocharges alter it. Thus, the change can be quantitatively represented as

$$\Delta\phi_n = -\frac{1}{2\epsilon}\rho_{\text{piezo}}W_{\text{piezo}}^2 - \frac{kT}{q}\ln\left(\frac{n_0 + \Delta n}{n_0}\right) \quad (39)$$

Therefore, the total modified barrier height is

$$\phi_n = \phi_{n0} + \Delta\phi_n \quad (40)$$

where  $\phi_{n0}$  is the original SBH.

Under a forward bias, the electron current density through a Schottky contact is

$$J_n = J_{n0}\left(\frac{n_0 + \Delta n}{n_0}\right)\exp\left(\frac{q}{kT}\frac{1}{2\epsilon}\rho_{\text{piezo}}W_{\text{piezo}}^2\right) \quad (41)$$

where  $J_{n0}$  is the original current density without any external stimulation, and

$$J_{n0} = A^*T^2\exp\left(-\frac{q}{kT}\phi_{n0}\right)\left[\exp\left(\frac{qV}{kT}\right) - 1\right] \quad (42)$$

As a consequence, the photoexcitation process can be either enhanced or inhibited by changing the direction or type of applied strain, which correlates with the sign of  $\rho_{\text{piezo}}$ .

In regard to a double Schottky contact structure, the phenomena become slightly more complicated. A reverse bias junction always occurs along with a forward bias junction under a certain bias voltage. According to Ohm's law for the entire device, the current should be expressed as

$$I = S_R J_R = \frac{V_{NW}}{R_{NW}} = S_F J_F \quad (43)$$

where  $S_R$  and  $S_F$  are the cross-sectional areas for the reverse and forward junctions, respectively,  $R_{NW}$  is the NW resistance, and  $V_{NW}$  is the voltage drop over the NW.

Therefore, the total voltage can be interpreted as consisting of three parts:

$$V = V_R + V_{NW} + V_F \quad (44)$$

where  $V_R$  and  $V_F$  are the voltage drops on the reverse and forward junctions, respectively. In real and common cases, the impact of the term  $R_{NW}$  on the current behavior is usually observed at applied voltages greater than 5 V. However, for a photodetector under its operating voltage, the dominant factor is the reverse bias contact.<sup>129</sup> To understand the effects induced by piezocharges as well as photoexcitation,  $V_R = cV$  can be taken to obtain a clear explanation, where  $c$  is a constant less than 1. Thus, eq 42 can be revised as

$$J = J_{sv}\exp\left(-\frac{q}{akT}\phi_{n0}\right)\exp\left[V\frac{q}{kT}c\left(1 - \frac{1}{a}\right)\right]\left(\frac{n_0 + \Delta n}{n_0}\right)^{1/a}\exp\left(\frac{q}{akT}\frac{1}{2\epsilon}\rho_{\text{piezo}}W_{\text{piezo}}^2\right) \quad (45)$$

Thus, the device current for a reverse bias on contact 1 ( $V > 0$ ) takes the form

$$I = S_1 J_{c1}\left(\frac{n_0 + \Delta n}{n_0}\right)^{1/a}\exp\left(\frac{q}{akT}\frac{1}{2\epsilon}\rho_{\text{piezo1}}W_{\text{piezo1}}^2\right) \quad (46)$$

For a reverse bias on contact 2 ( $V < 0$ ), this current can be described as

$$I = -S_2 J_{c2}\left(\frac{n_0 + \Delta n}{n_0}\right)^{1/a}\exp\left(\frac{q}{akT}\frac{1}{2\epsilon}\rho_{\text{piezo2}}W_{\text{piezo2}}^2\right) \quad (47)$$

where:

$$J_{c1} = J_{sv1}\exp\left(-\frac{q}{a_1kT}\phi_{n10}\right)\exp\left[V\frac{q}{kT}c_1\left(1 - \frac{1}{a_1}\right)\right]$$

and

$$J_{c2} = J_{sv2}\exp\left(-\frac{q}{a_2kT}\phi_{n20}\right)\exp\left[V\frac{q}{kT}c_2\left(1 - \frac{1}{a_2}\right)\right]$$

are the currents flowing from reverse contacts 1 and 2, respectively. In addition,  $k$  is the Boltzmann constant. Since  $\rho_{\text{piezo1}}$  and  $\rho_{\text{piezo2}}$  have opposite signs, asymmetric changes for the opposite biases are clearly observed under the same applied strain.

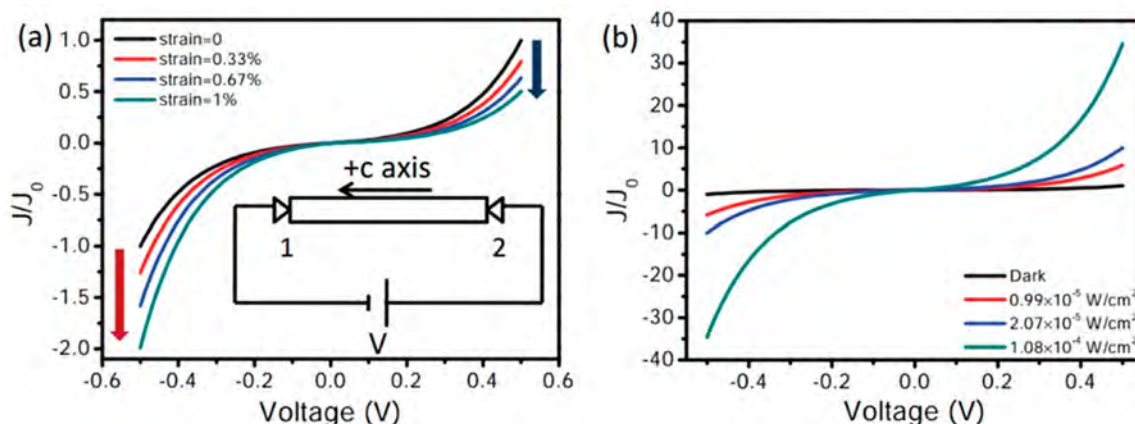


**Figure 17.** Numerical simulations for a Ag–ZnO–Ag device with two Schottky contacts. (a) Relative current density versus voltage under various strains and the same illumination power. (b) Diagram of relative current density versus voltage under different illumination powers without external strain. Reproduced with permission from ref 126. Copyright 2012 John Wiley and Sons.

Analytical results were utilized for numerical simulation of a Ag–ZnO–Ag structure. The detailed parameters for ZnO were as follows: diameter  $d = 100$  nm, carrier lifetime  $\tau_n = 3$  ns, external quantum efficiency  $\eta_{\text{ext}} = 1$ , and internal gain  $\Gamma_G = 1.5 \times 10^5$ .<sup>130</sup> A typical UV light was employed with wavelength  $\lambda = 385$  nm, and the electron concentration of ZnO NWs under dark conditions was presumed to be  $1 \times 10^{15} \text{ cm}^{-3}$ . Most piezo-phototronic devices are made from wurtzite family materials, for example, ZnO, GaN, CdS, and AlN, so they have the same piezoelectric coefficient matrix, and this simulation is suitable for all wurtzite family material-based devices.

When the two M–S contacts of the Ag–ZnO–Ag device are one ohmic contact and one Schottky contact, the photocurrents under various applied external strains ranging from 0 to 1% and uniform light illumination can be obtained using eq 41. Figure 16 depicts some of the numerical results based on the proposed structure. Depending on the direction of the  $c$ -axis, the photocurrent can clearly be either enhanced or restrained. Specifically, the electrical performances for two single-Schottky-contact devices are demonstrated in Figure 16a and 16b, where the insets show their corresponding configurations. As a reference case, the photocurrents for different illumination powers under a strain-free condition are also given in Figure 16c. For comparison, a Ag–ZnO–Ag structure with two Schottky contacts is also taken into consideration. Equation 41 plays a pivotal role in the entire simulation process, and in detail, the values  $a$  and  $c$  are set as 1.3 and 1.8, respectively, according to previous reports.<sup>129</sup> The numerical results for the proposed two-Schottky-contact structure are shown in Figure 17. In brief, an asymmetric feature is observed with respect to the piezo-phototronic effect. Under the opposite bias voltage and the same external strain, the current deviation shows the opposite tendency. Thus, the piezo-phototronic effect is clearly greatly significant in tuning the performance of the photodetector device, giving rise to an enhanced sensitivity and a broader application range.<sup>50,114,115,126,131</sup>

**3.3.4. Piezo-phototronic Effect in Solar Cells.** Clean energy is on the rise, from windmills to hydropower stations, and people are now increasingly demanding cleaner energy. Solar power is not new, and since the advent of silicon cells, it has undergone fast growth. Though many renewable energy sources exist, solar power is still one of the most promising candidates to solve energy crises.

The development of new energy-efficient materials and the construction of new structures are two prevailing methods to optimize solar cell performance, and tremendous efforts have been channeled into both.<sup>132</sup> For instance, to decrease the saturation current in Si-based solar cells, metal–insulator–semiconductor (MIS) structures have been incorporated.<sup>133,134</sup> With the aid of thermodynamic theory, investigations of the thickness dependence of p–n junctions have enabled a high open-circuit voltage to be achieved for photovoltaic (PV) devices.<sup>135</sup> Based on the low bandgap material PBDTTT4, the open-circuit voltage for a polymer solar cell can be enhanced to 0.76 V with an overall power efficiency of 6.77%.<sup>136</sup> In addition, advanced materials, such as fullerene, have also been employed to realize superb performance.<sup>15</sup> All of these approaches promote more developed and outstanding solar devices.

Lately, the advancements in piezoelectric and ferroelectric materials have blazed another trail toward better solar cells. Enabled by the intrinsic electric potential coming from the materials themselves, the charge separation process becomes much easier. By incorporating these materials, piezoelectric solar cells (PSCs)<sup>44</sup> and ferroelectric solar cells<sup>137</sup> were fabricated, showing remarkable output performance. Given this result, establishing the basic theory to obtain a deeper insight into the mechanism is highly desired.

Figure 18 shows a typical NW-based p–n junction solar cell.<sup>138</sup> The device has either one p–n junction or one M–S contact. By applying a high electric field to the device depletion region, electron–hole pairs generated by incident photons are spontaneously separated. If this cell is constructed with a piezoelectric material, when under an external strain, the piezoelectric charges generated at the interface of the junction will greatly facilitate control of the cell performance. The proposed solar cell device was built with a nonpiezoelectric p-type and piezoelectric n-type heterostructure junction, where ZnO was again selected as the key component for modulation, as shown in Figure 18b and 18c.

Due to the photocoupling, the properties of a PSC can also be characterized with the help of semiconductor physics and piezoelectric theory. For a piezoelectric semiconductor material under an external stress, two common effects arise: the piezoresistance effect and the piezotronic effect. Piezoresistance is generally accepted to be a volume effect, which manifests as a variation in the resistance of the bulk

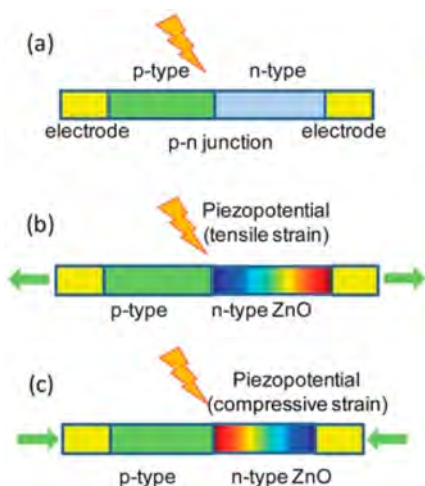


**Figure 18.** (a) Schematic illustration of a basic NW solar cell with a p–n junction. Under (b) tensile or (c) compressive strain, a piezopotential distribution emerges in the proposed n-type PSC, which dramatically modulates the carrier generation, separation, and transport characteristics. Reproduced with permission from ref 138. Copyright 2012 Royal Society of Chemistry.

semiconductor but has little influence on the contact property.<sup>99,100</sup> The change in the bandgap resulting from this effect does not correspond to the sign of the piezoelectric charges in the contact area. In light of this feature, the piezophototronic effect more strongly affects the output of solar cells.<sup>44,117</sup>

Recent experiments have shown that the open-circuit voltage and the maximum output power are sensitive to the external strain applied to ZnO NWs; however, the short-circuit current density is not affected.<sup>132</sup> Hence, the photocurrent density (short-circuit current density) is assumed to not correspond to the external strain. Theoretically, the excitation of excess

carriers by solar radiation gives rise to the short-circuit current. For simplicity, the electron and hole generation rates ( $G_n$  and  $G_p$ ) are considered to be constant as follows:

$$G_n = G_p = \frac{J_{\text{solar}}}{q(L_n + L_p)} \quad (48)$$

where  $J_{\text{solar}}$  is the short-circuit current density, and  $L_p$  and  $L_n$  are the diffusion lengths of holes and electrons, respectively. For simplification, photon emission is neglected in this model; in other words,  $U_n = U_p = 0$ . Similar to the 1D NW-based piezotronic p–n junction model, the photocurrent  $J_{\text{solar}}$  results in a modification of the total current density. By solving the basic eqs 1–5 and 32, the total current density can be derived as

$$J = J_{\text{pn}} \left[ \exp\left(\frac{qV}{kT}\right) - 1 \right] - J_{\text{solar}} \quad (49)$$

$$J_{\text{pn}} \equiv \frac{qD_p p_{n0}}{L_p} + \frac{qD_n n_{p0}}{L_n} \quad (50)$$

where  $J_{\text{pn}}$  is the saturation current density. Typically, for a solar cell constructed with a p-polymer and an n-type ZnO NW, the ZnO part commonly possesses a high n-type conductivity.<sup>139,140</sup> An abrupt junction at the p-type side can therefore be reasonably assumed, in which  $n_{p0} \gg p_{n0}$  and  $J_{\text{pn}} \approx \frac{qD_n n_{p0}}{L_p}$ .

Combining the previous results, the total current density can be revised as<sup>138</sup>

$$J = J_{\text{pn}0} \exp\left(-\frac{q^2 \rho_{\text{piezo}} W_{\text{piezo}}^2}{2\epsilon_s kT}\right) \left[ \exp\left(\frac{qV}{kT}\right) - 1 \right] - J_{\text{solar}} \quad (51)$$

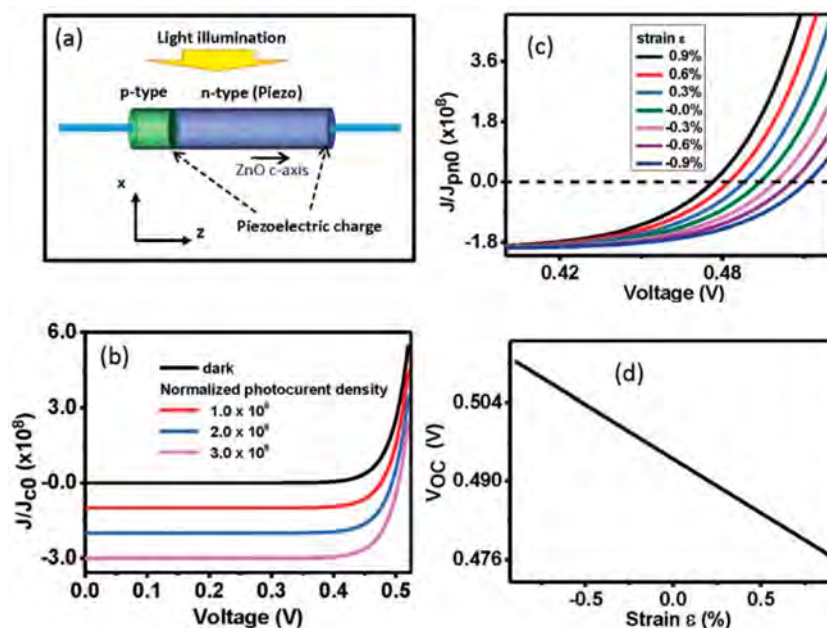


**Figure 19.** (a) Schematic illustration of the proposed ZnO NW-based solar cell. (b) Diagram of the relative current density versus voltage under different photocurrent densities. (c) Relative current density–voltage relationship under different external strains. (d) Open-circuit voltage under various applied external strains. Reproduced with permission from ref 138. Copyright 2012 Royal Society of Chemistry.

$$J_{pn} = J_{pn0} \exp\left(-\frac{q^2 \rho_{\text{piezo}} W_{\text{piezo}}^2}{2\epsilon_s kT}\right) \quad (52)$$

where the saturation current density without a piezopotential is given by  $J_{pn0} \approx \frac{qD_n n_{p0}}{L_n} \exp\left(-\frac{E_i - E_{F0}}{kT}\right)$ . Note that a negative sign appears in the exponential function of eq 52, in contrast to a previous study on piezoelectric p–n junctions. Here, two approximate cases can be studied: When  $n_{p0} \gg p_{n0}$ , the thermal equilibrium electron concentration  $n_{p0}$  becomes the dominant factor in the current characteristics, which corresponds to the PSC model. If  $p_{n0} \gg n_{p0}$ , the thermal equilibrium hole concentration becomes dominant. For the proposed NW model, if a compressive strain is employed, then the positive piezoelectric charges repel holes while attracting electrons. Conversely, if a tensile strain is applied, then the negative piezoelectric charges will attract holes while repelling electrons. Both cases contribute to the negative sign in the exponential function of eq 52.

In addition, the open-circuit voltage for a solar cell can be calculated by setting  $J = 0$ :<sup>17</sup>

$$V_{oc} = \frac{kT}{q} \ln\left(\frac{J_{\text{solar}}}{J_{pn}} + 1\right) \quad (53)$$

For a specific solar cell with  $J_{\text{solar}} \gg J_{pn}$ , the open-circuit voltage can be given as

$$V_{oc} \approx \frac{kT}{q} \ln\left(\frac{J_{\text{solar}}}{J_{pn}}\right) = \frac{kT}{q} \left\{ \ln\left(\frac{J_{\text{solar}}}{J_{pn0}}\right) + \frac{q^2 \rho_{\text{piezo}} W_{\text{piezo}}^2}{2\epsilon_s kT} \right\} \quad (54)$$

Thus, from eq 54, the open-circuit voltage can clearly be modulated by both the magnitude and sign (tension or compression) of the strain. This result can be extensively applied to bulk or thin film solar cells.

In light of the relationship between the polarization vector and mechanical strain in eq 54, for a GaN or ZnO NW with a strain  $s_{33}$  along its  $c$ -axis (growth orientation),  $q\rho_{\text{piezo}} W_{\text{piezo}} = -e_{33}s_{33}$ . To visualize the piezo-phototronic effect in specific solar cells, several parameters are set for numerical simulation: the diameter of the NW is 20 nm, and the partial lengths for the p-type and n-type segments are selected as 20 and 80 nm, respectively.

Figure 19a schematically illustrates the proposed model. Light uniformly irradiates the entire solar cell structure, in which the n-side exhibits the piezoelectric effect and the  $c$ -axis points away from the p–n junction. The  $I$ – $V$  characteristics calculated under different light intensities are shown in Figure 19b. Obviously, the short-circuit current density quickly increases with enhanced light intensity. If the saturation current density decreases, then the open-circuit voltage seems to increase slightly. In addition, the  $J$ – $V$  characteristics for the solar cell are shown in Figure 19c. With the applied external strain is changed from  $-0.9\%$  to  $0.9\%$ , the relative current density tends to accordingly improve. The piezo-phototronics of the solar cell can be reflected by the relationship between the open-circuit voltage and the applied strain, as elucidated in Figure 19d. When the strain is switched from  $-0.9\%$  to  $0.9\%$ , the open-circuit voltage decreases from 0.48 to 0.51 V.

The maximum output power of the proposed solar cell can be acquired through analytical results. As shown in Figure 20a,

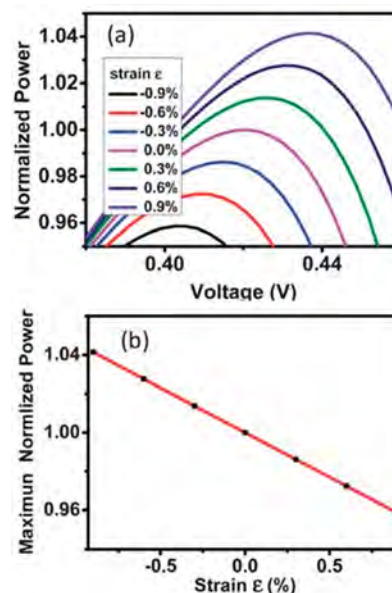


**Figure 20.** (a) Diagram of the output power versus voltage for a ZnO NW-based p–n junction piezo-phototronic solar cell; (b) strain-tuned relative maximum normalized output power. Reproduced with permission from ref 138. Copyright 2012 Royal Society of Chemistry.

when the photocurrent density is fixed, the output power curves rise with increasing external strain, with different maximum values. In Figure 20b, the relative maximum output power versus applied strain is depicted. Undoubtedly, the application of an external strain to the ZnO NW can dramatically modify the maximum output power of the solar cell.

For comparison, the cases of reversed  $c$ -axis polarity on the piezoelectric side or an exchange of the p and n parts is investigated, as shown in Figure 21. The detailed models are displayed in the insets. Compared with Figure 21a, a reversed  $c$ -axis leads to an opposite trend for the strain dependence on the current density due to the opposite sign of the piezoelectric charges (Figure 21a). Hence, the open-circuit voltage increases with changing applied external strain from  $-0.9\%$  to  $0.9\%$ , as shown in Figure 21b. Similarly, the exchange of the p and n segments in the device can achieve the same effect, as shown in Figure 21c and 21d. These results indicate that an enhanced performance for solar cells can be achieved through both of the above structure optimization processes.

In an M–S solar cell device, the M–S contact is also an essential element. Specifically, for the proposed piezoelectric n-type semiconductor NW, the total current density through an M–S contact can be derived as

$$J = J_{MS} \left[ \exp\left(\frac{qV}{kT}\right) - 1 \right] - J_{\text{solar}} \quad (55)$$

$$J_{MS} = J_{MS0} \exp\left(\frac{q^2 \rho_{\text{piezo}} W_{\text{piezo}}^2}{2\epsilon_s kT}\right) \quad (56)$$

where  $J_{MS}$  is the saturation current density of the M–S contact and  $J_{MS0}$  is the corresponding value without piezoelectric charges:

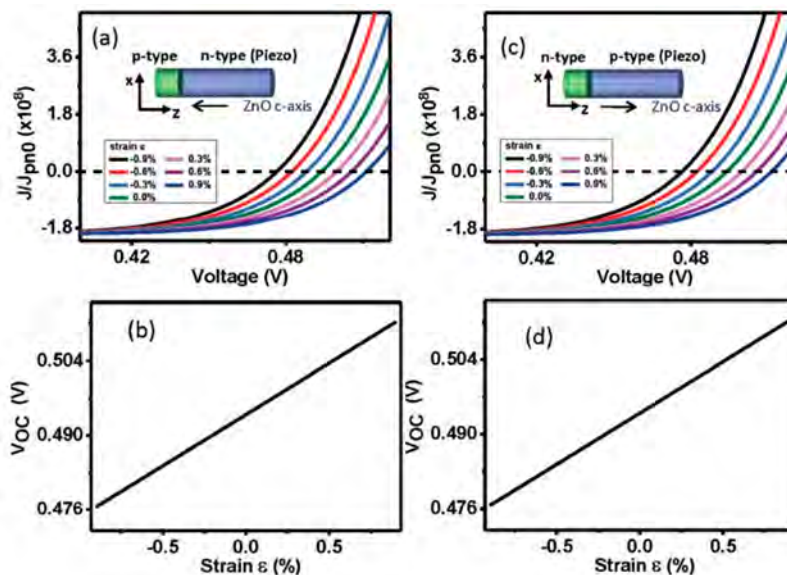


**Figure 21.** (a)  $I$ – $V$  curves and (b) open-circuit voltage under various strains for a specific p–n-type ZnO NW-based solar cell. In this case, the  $c$ -axis of ZnO is pointing toward the junction. (c)  $I$ – $V$  curves and (d) open-circuit voltage under various strains for the same solar cell. In this case, the  $c$ -axis of ZnO is pointing out of the junction. Reproduced with permission from ref 138. Copyright 2012 Royal Society of Chemistry.

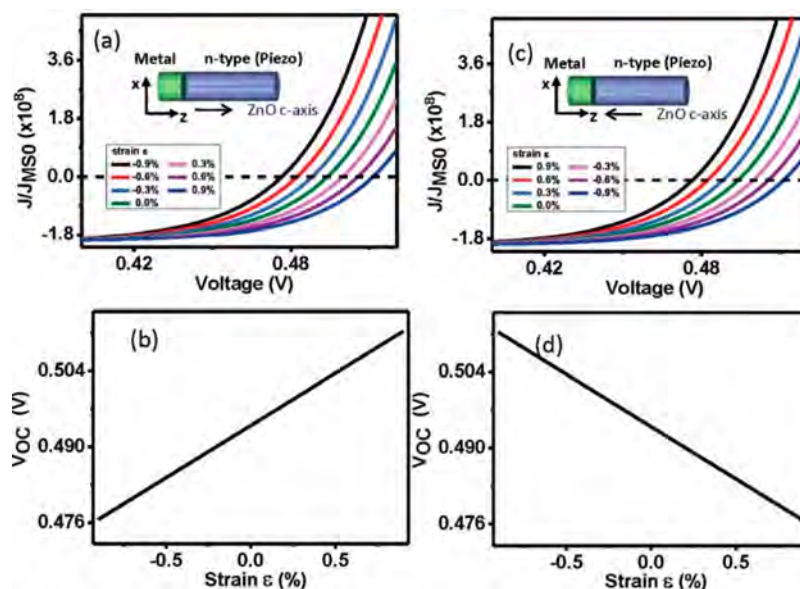


**Figure 22.** (a)  $I$ – $V$  curves and (b) open-circuit voltage under various strains for an M–S (ZnO NW) contact, where its  $c$ -axis points away from the junction. (c)  $I$ – $V$  curves and (d) open-circuit voltage under various strains for the same device, where its  $c$ -axis points toward the junction. Reproduced with permission from ref 138. Copyright 2012 Royal Society of Chemistry.

$$J_{MS0} = \frac{q^2 D_n N_c}{kT} \sqrt{\frac{2qN_D(\psi_{bi0} - V)}{\epsilon_s}} \exp\left(-\frac{q\phi_{Bn0}}{kT}\right) \quad (57)$$

Note that the piezocharges function as a perturbation to  $E_C$ . Therefore, the open-circuit voltage for a solar cell with an M–S contact can be acquired as

$$V_{oc} \approx \frac{kT}{q} \left\{ \ln\left(\frac{J_{solar}}{J_{MS0}}\right) - \frac{q^2 \rho_{piezo} W_{piezo}^2}{2\epsilon_s kT} \right\} \quad (58)$$

Consider eq 56 and eq 58. In the positive strain (tensile strain) case, the local negative piezocharges clearly lift the barrier at the M–S contact, thus realizing a decrease in the

saturation current density while enhancing the open-circuit voltage. In contrast, when the applied strain is changed to compressive strain, the situation is reversed.

Similar to the above calculation process for the p–n junction case, when a strain is applied along the longitudinal direction of the NW, the detailed parameters are also suitable for the M–S contact model. Figure 22a and c shows abstract schematics for the calculated model. In Figure 22a, under fixed light illumination, the relative current density clearly decreases when the external strain varies from  $-0.9\%$  to  $0.9\%$ . However, the open-circuit voltage increases with increasing strain, as demonstrated in Figure 22b. As a comparison, a numerical simulation for a shift of the  $c$ -axis in the polar direction for the M–S contact was also performed, as shown in

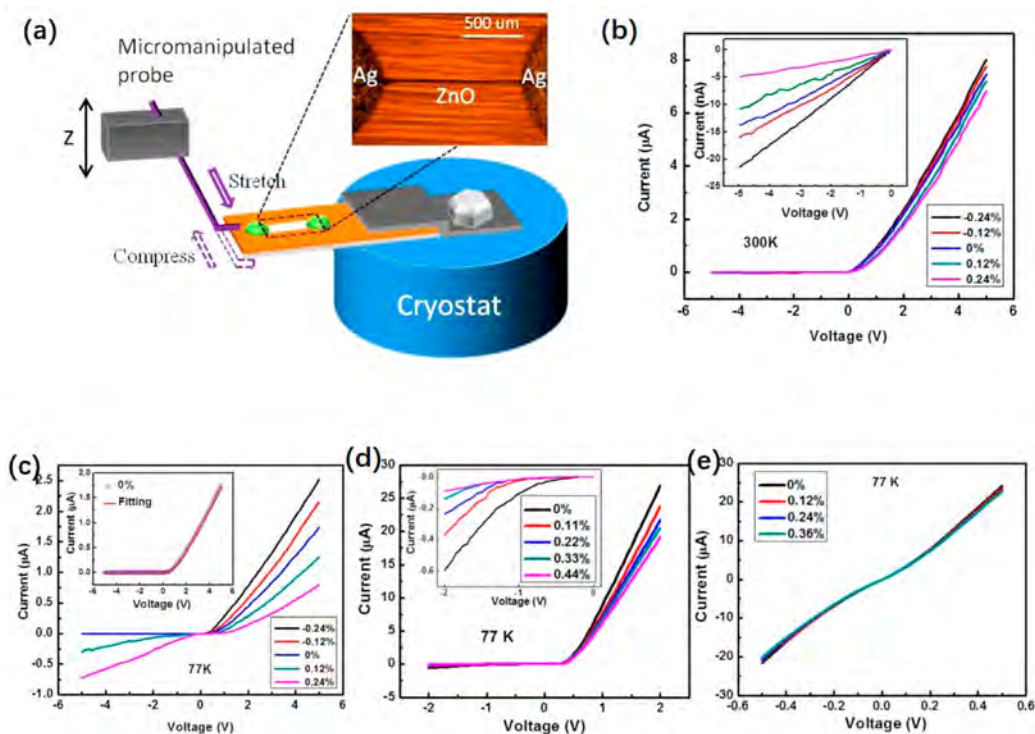


**Figure 23.** (a) Schematic illustration of the measurement setup. A device is fixed on the edge of a cryostat. A micromanipulated probe is used to deform the substrate. The upper right inset is a photograph of a real device. (b) Changes in the transport characteristics of devices with low conductivity under applied strain at 300 K. (c) Changes in the transport characteristics of devices with low conductivity under applied strain at 77 K. (d) Changes in the transport characteristics of devices with moderate conductivity under applied strain at 77 K. (e) Changes in the transport characteristics of devices with high conductivity under applied strain at 77 K. Reproduced from ref 143. Copyright 2013 American Chemical Society.

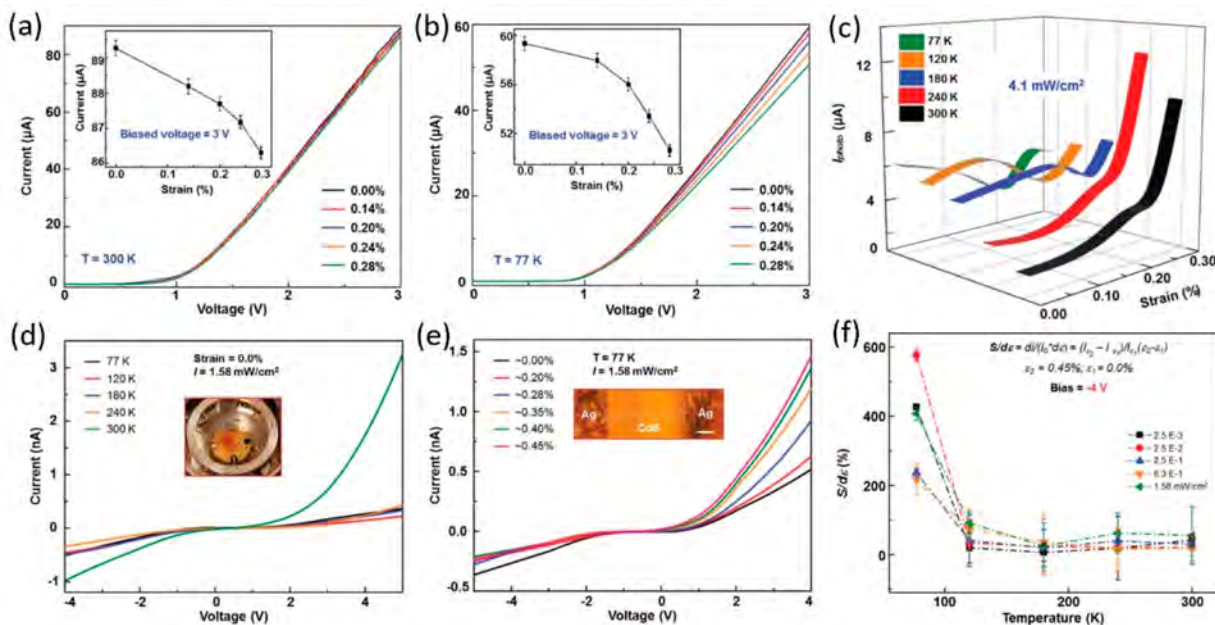


**Figure 24.** (a) Change in the  $I$ - $V$  characteristics of GaN devices due to the piezotronic effect at 300 K under dark conditions. (b) Change in the  $I$ - $V$  characteristics of GaN devices due to the piezotronic effect at 77 K under dark conditions. (c) Photocurrent of GaN devices versus tensile strain at various temperatures under the fixed illumination. Reproduced with permission from ref 144. Copyright 2015 John Wiley and Sons. (d)  $I$ - $V$  characteristics of CdS NW devices under various temperatures for a power density of  $1.58 \text{ mW cm}^{-2}$ . (e)  $I$ - $V$  characteristics of CdS NW devices under various strain conditions for a power density of  $1.58 \text{ mW cm}^{-2}$ . (f) Temperature dependence of the piezo-phototronic factor at a  $-4 \text{ V}$  bias voltage. Reproduced with permission from ref 145. Copyright 2015 John Wiley and Sons.

Figure 22c and d. According to the results, reverse trends in both the relative current density and open-circuit voltage with respect to the applied strain emerge, which is understandable due to the reverse polarization. Therefore, for an M–S contact solar cell, the electrical performance can be largely modified by the piezo-phototronic effect.<sup>141</sup>

### 3.4. Temperature Dependence of Piezotronics and Piezo-phototronics

The influence of temperature on the piezotronic and piezo-phototronic effects is now discussed, which will be conducive to understanding the underlying physical mechanisms of these two effects. Temperature can dramatically impact the carrier density of a semiconductor,<sup>142</sup> which is closely related to the piezotronic and piezo-phototronic effects. In 2013, Hu et al. thoroughly investigated the temperature dependence of the piezotronic effect by employing ZnO NWs for the first time.<sup>143</sup> In their configuration, ZnO NWs with three different dopant concentrations were integrated into a flexible substrate that was clamped at the edge to a cryostat, and the corresponding experimental setup is schematically shown in Figure 23a. The ZnO NW devices were made into typical M–S–M structures using silver paste as the electrodes, thus forming two back-to-back Schottky barriers. Their piezotronic response was measured under different strains by reducing the temperature from 300 to 70 K. The piezotronic effect is markedly enhanced with decreasing temperature. Specifically, a distinct difference is observed in the  $I$ – $V$  curves between 300 and 77 K for low-doped ZnO NW devices when applying an external strain. The current similarly increases or decreases by different magnitudes under different strains regardless of the direction of the bias voltage at 300 K, as shown in Figure 23b. The variation trend of the current is increased under a negative bias and decreased under a positive bias (or vice versa) when the temperature is decreased to 77 K, presenting an obvious asymmetric behavior (Figure 23c). This phenomenon was first observed in this study. The results illustrate that the piezotronic effect is dominant at the two Schottky contacts at low temperature, attributed to the screening effect of piezocharges by free carriers being weakened owing to the reduction in the carrier concentration as the temperature decreases. For moderately doped ZnO NWs, the current decreases asymmetrically under both positive and negative bias voltages with applied tensile strain at 77 K (Figure 23d). This result suggests that the piezotronic effect is only dominant at the one side where negative piezocharges are created, and the other side, where positive piezocharges accumulate, is still screened by free carriers. Once the ZnO NWs are heavily doped, the current exhibits no response to an external tensile strain even when the temperature is dropped to 77 K (Figure 23e), meaning that the piezotronic effect barely works in this case.

In addition to ZnO NWs, Wang and co-workers further studied the piezotronic effect in  $a$ -axis GaN nanobelts under different temperatures.<sup>144</sup> The fabrication process of the devices and experimental system are similar to those previously reported by Hu et al. Figure 24a and b displays the typical  $I$ – $V$  curves of the GaN devices under externally applied strain at 300 and 77 K, respectively. The changes in the current with increasing strain are clearly more noticeable at 77 K than at 300 K. A qualitative analysis indicates that the piezotronic effect in the  $a$ -axis GaN can be enhanced by over 440% when the temperature decreases from 300 to 77 K under 0.28% tensile strain. This enhancement occurs because the freeze-out

effect of free carriers increases the number of effective piezocharges due to the reduced screening effect at low temperature, analogous to the effect of temperature on the piezotronics in ZnO NWs. Considering the superior optical excitation of GaN, these authors also examined the temperature dependence of the piezo-phototronic effect based on GaN nanobelt devices. The three-dimensional (3D) diagram in Figure 24c depicts the photocurrent ( $I_{\text{photo}}$ ) as a function of strain at various temperatures ranging from 77 to 300 K.  $I_{\text{photo}}$  gradually increases with increasing tensile strain at 240 and 300 K, but at low temperature (180, 120, and 77 K), it first decreases and then increases as the tensile strain increases. This novel phenomenon results from a competing mechanism between the attraction of noncompletely screened positive piezocharges to electrons and detrapping/activation of bound electrons at low temperature.

In another work, the impact of temperature on the piezo-phototronic effect in CdS NWs was also systematically explored by varying the temperature from 77 to 300 K; therein, the piezo-phototronic effect could be enhanced by over 550% at 77 K.<sup>145</sup> Under a fixed illumination intensity of 1.58 mW cm<sup>-2</sup> and strain-free conditions, the photocurrent of CdS NWs varies with temperature as displayed in Figure 24d, and the inset exhibits the experimental system. However, once mechanical strain is introduced to the device at 77 K under the same illumination conditions, the photocurrent markedly increases in the positive bias regime, as shown in Figure 24e. To further analyze the experimental data, a physical parameter named the piezo-phototronic factor was defined as the response sensitivity per unit strain:  $d_{\epsilon} = dI/(I_0 \times d_{\epsilon}) = (I_{\epsilon_2} - I_{\epsilon_1})/I_{\epsilon_1}(\epsilon_2 - \epsilon_1)$ , in which  $I_{\epsilon_2}$  and  $I_{\epsilon_1}$  correspond to the currents derived under  $\epsilon_2$  and  $\epsilon_1$  strain conditions at the same illumination intensity, respectively. Figure 24f shows the piezo-phototronic factors derived under a  $-4$  V bias voltage. The maximum of the piezo-phototronic factor can reach 576.2% at 77 K under an illumination intensity of  $2.5 \times 10^{-2}$  mW cm<sup>-2</sup>, so the piezo-phototronic effect can also be significantly improved at low temperature. This improvement mainly occurs because the number of mobile charge carriers in CdS NWs decreases at lower temperatures, thus increasing the number of surface/interface effective piezocharges as a result of the reduced screening effect and further promoting the separation efficiency of photoinduced electron–hole pairs. These works minutely investigated the temperature dependence of the piezotronic and piezo-phototronic effects, which not only helps better understand the fundamental working mechanisms of these two effects but also provides valuable guidance for designing and developing high-performance piezotronic/piezo-phototronic devices.<sup>146</sup>

## 4. PIEZOTRONICS AND ITS APPLICATIONS

### 4.1. Piezotronic Effect-Based Strain Sensors

Investigations about micro- and nanoelectromechanical systems (MEMS and NEMS) are growing fast, with potential applications for ultrafast, low-power consumption and high-sensitivity devices. To measure nano- and microscale strain/stress and pressure, a lot of NW<sup>147</sup> and carbon nanotube (CNT)<sup>148–152</sup> sensors have been fabricated. Normally, such kind of strain sensors use the piezoresistance effect of the nanomaterial; for example, upon a relatively small strain, the change of resistance has a linear relationship with the change of strain.<sup>106,114,153–159</sup>

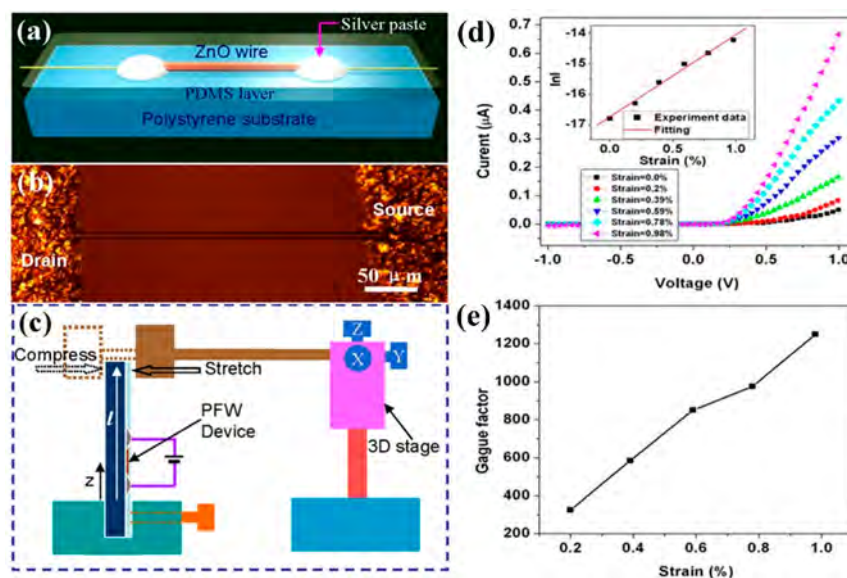


**Figure 25.** (a–b) Illustration and optical image of a single ZnO NW based strain sensor. (c) The measurement setup of the ZnO NW strain sensor. (d)  $I$ – $V$  curves of a ZnO NW strain sensor under various strains. The inset is the relationship between  $\ln I$  (A) and the applied strain. (e) Gauge factors calculated from (d) vs applied strain. Reproduced from ref 24. Copyright 2008 American Chemical Society.

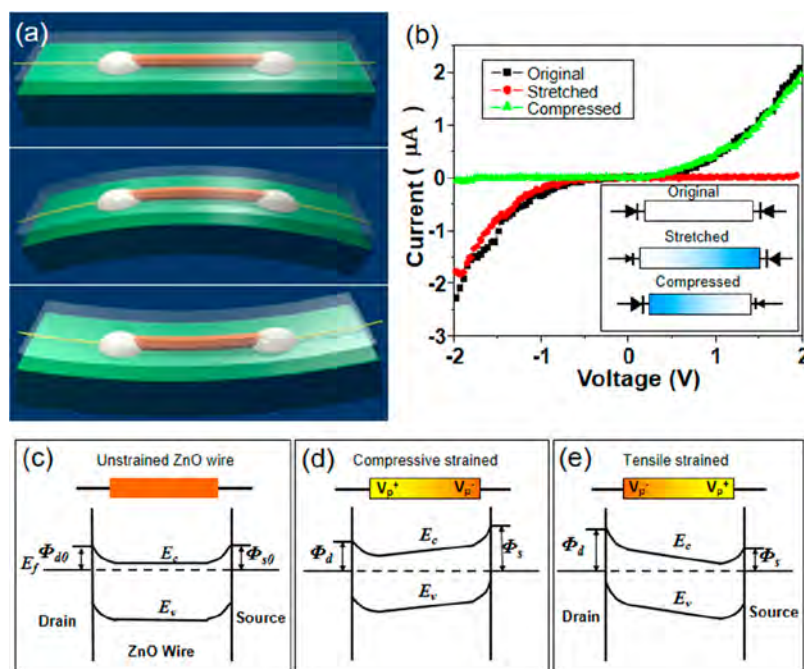


**Figure 26.** (a) Illustration of a single ZnO NW device. (b)  $I$ – $V$  performance of the ZnO NW device under a compressive strain (green), after strain release (black), and under tensile strain (red). (c–e) Energy band diagrams demonstrating the changes in the SBH at the two contacts of (c) unstrained, (d) compressive strained, and (e) tensile strained NWs. Reproduced from ref 23. Copyright 2008 American Chemical Society.

In this section, a new kind of strain sensor by using the piezotronic effect is introduced.<sup>160,161</sup> In 2008, Zhou, Wang, and co-workers presented the fabrication and application of a fully packaged strain sensor based on an individual ZnO NW.<sup>24</sup> This strain sensor was fabricated by laterally bonding a single piezoelectric ZnO NW onto a polystyrene (PS) substrate. A schematic of the strain sensor is demonstrated in Figure 25a, along with a photograph of the strain sensor in Figure 25b. The corresponding measurement setup is illuminated in Figure 25c.

The  $I$ – $V$  curves (Figure 25d) are very sensitive to strain because of the change in the SBH because of the piezotronic

effect, with a linear relationship with the applied external strain. The inset shows that  $\ln I$  scales linearly with the external strain as well. A gauge factor of as high as 1250 has been demonstrated (Figure 25e). For comparison, the gauge factors of commercial alloy strain gauges, semiconductor Si strain sensors, and CNT based strain gauges are 2, 200 and 1000, respectively.

#### 4.2. Piezotronic Strain-Gated Piezoelectric Electromechanical Switches

In section 3.1, we introduced the fundamentals of a piezoelectric transistor, whose basic principle is to tune the

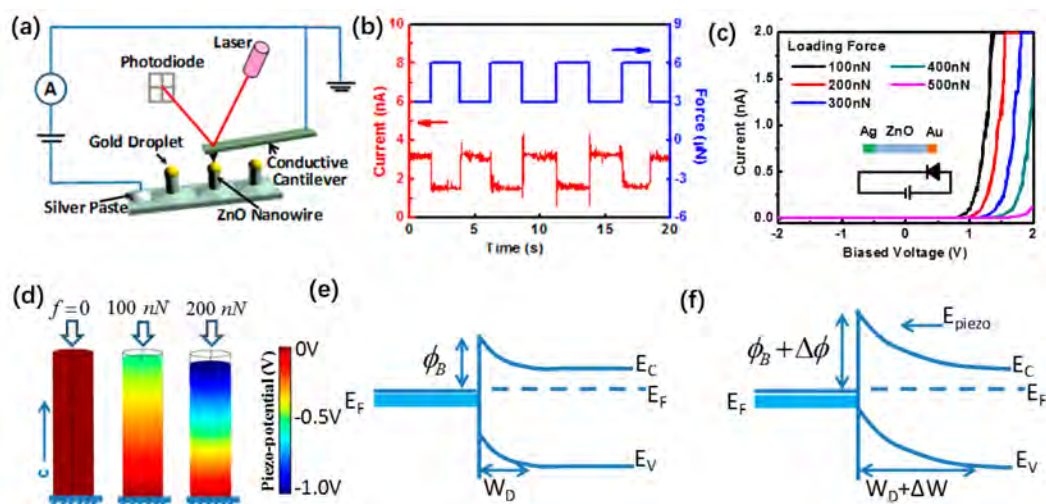


**Figure 27.** (a) Schematic diagram of the AFM system used to measure vertical piezotronic transistors. (b) Current changes with a periodic applied force of  $3 \mu\text{N}$  and  $6 \mu\text{N}$ . (c)  $I$ – $V$  properties of a vertical piezotronic transistor with a single Schottky junction under different compressive forces. (d) Finite element simulation of the piezoelectric potential distribution in a ZnO NW (width: 50 nm and length: 100 nm) under three uniaxial forces of 0 nN (left), 100 nN (middle), and 200 nN (right). (e–f) Energy band diagrams showing the SBH change before and after a strain is applied to the top of the NW. Reproduced from ref 171. Copyright 2008 American Chemical Society.

carrier transport at the interface of M–S by changing the local barrier through a piezopotential which is applied by external strain. In this section, we demonstrate how to use the strain to modulate the transportation of an NW device, from rectification to the realization of a diode.<sup>162,163</sup>

In 2008, Zhou, Wang, and co-workers reported a piezopotential-tuned ZnO NW switch based on two back-to-back Schottky diodes.<sup>23</sup> The fabrication of such a piezoelectric electromechanical switch is similar to that of the previous piezotronic strain sensor in section 4.1, as shown in Figure 26a. Different from the devices we focused on in the previous section, here, we only consider the devices which shows symmetric or relative symmetric  $I$ – $V$  behavior, which can have either ohmic contact or symmetric Schottky contacts at both of the two ends (as in Figure 26b). If a tensile strain is applied to this switch, upward diode-like  $I$ – $V$  properties are obtained (red line); on the contrary, downward diode-like  $I$ – $V$  behavior (green line) is obtained when the switch is subjected to a compressive strain. The  $I$ – $V$  curve (black line) fully recovers when the external strain is released. Thus, a new kind of switch based on piezotronics with an “on”/“off” ratio as high as 120 has been designed and fabricated.

The operation mechanism of this device comes from the piezopotential generated asymmetric modulation of the SBH at both the drain and source electrodes, which can be illustrated with schematic energy band diagrams; see Figure 26d–e. Supposing that the  $c$ -axis of the ZnO NW is pointing toward the source, the drain side has a larger piezopotential if the switch is under a compressive strain (Figure 26e); thus, a higher SBH is generated at the source side. On the other hand, in the case of switching the compressive strain to a tensile strain through tuning the bending direction of the flexible substrate, the piezopotential decreases (Figure 26d), resulting in a higher SBH at the drain side.

#### 4.3. Piezotronic Transistors Based on Vertical NWs

In addition to the lateral ZnO NW-based piezotronic transistor, vertically aligned ZnO NWs based piezotronic strain-gated transistor arrays have been demonstrated, which may have great application in 3D integrations.<sup>8,25,164–170</sup> In

2012, Han, Wang, and co-workers reported a piezotronic transistor based on vertical ZnO NWs with Au nanoparticle catalysts on top. The  $I$ – $V$  characteristics of the transistor were recorded in contact mode in a conductive AFM system under different strains (Figure 27a).<sup>171</sup> Taking Figure 27b as an example, the output signal of the current has a very good and reversible response with an on/off ratio of approximately 7 when the external applied strain varies between 3 and  $6 \mu\text{N}$ . Figure 27c shows the  $I$ – $V$  characteristics of the transistor under different strains. By increasing the applied stress from 100 nN to 500 nN, the current sharply increases. Such strain-dependence of  $I$ – $V$  characteristics is attributed to the piezotronic effect, including the reverse and forward modes. We simulated the potential distribution using the finite element method and plot it in Figure 27d. To simply demonstrate the piezotronic effect in this case, the energy band diagrams are illustrated in Figure 27e–f. If the  $c$ -axis of the ZnO NW is along the direction from Au toward ZnO NW, then a piezoelectric potential will be generated whenever an external strain is applied to the NW, thus changing the carriers and tuning the local contact properties. The strain-dependence of piezopotential dramatically modulates the local contact characteristics and gates the carrier transportation processing at the interface of M–S.

Zhou and Wang et al. also reported similar vertical piezotronic transistors based on CdSe NWs, with the  $c$ -axis along the  $\langle 0001 \rangle$  direction.<sup>172</sup> Since CdSe has the same crystal structure as ZnO, when an external stress is applied to the CdSe NW, the piezotronic effect can elevate the Schottky barrier between CdSe and Pt. Even under a small change (0.12%) of strain, the current decreases from 84 to 17 pA upon a 2 V bias voltage.

#### 4.4. Piezotronic Transistor Arrays and Tactile Imaging

Design, fabrication, and integration of functional systems by using nanodevice arrays are key to transforming nanoscience into applied nanotechnology.<sup>173</sup> The traditional FETs, which have three-terminals (source, drain, and gate), based on voltage-gated operation limit the spatial resolution when they are used as tactile sensor arrays. Therefore, a new device

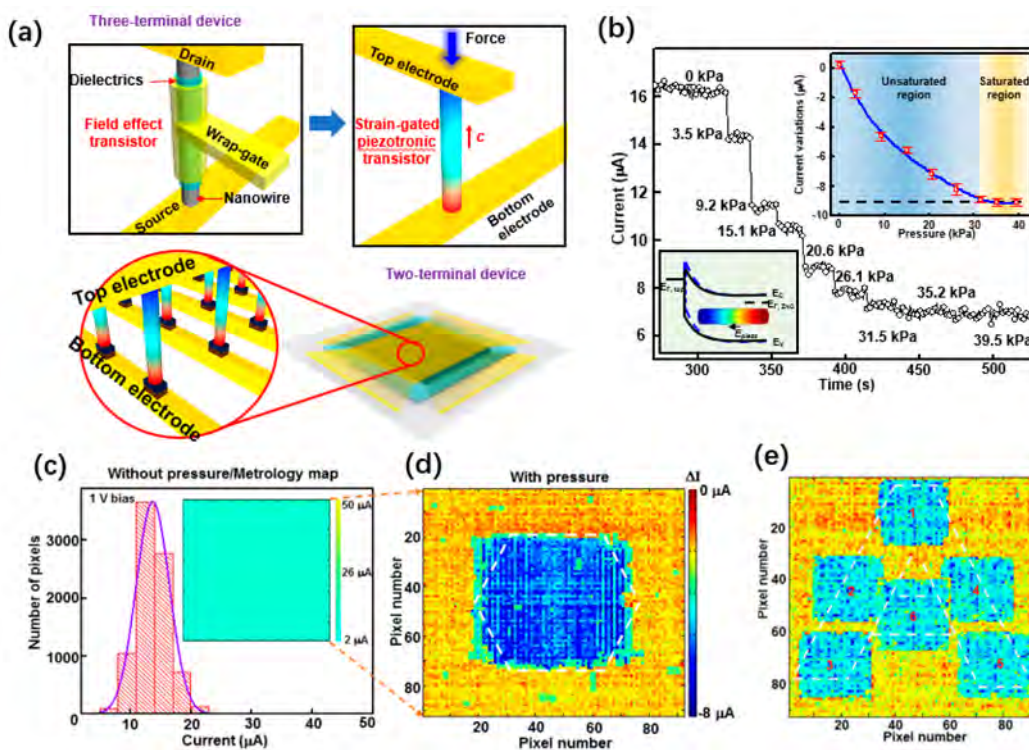


**Figure 28.** (a) Comparison between the traditional three-terminal FET devices and a two-terminal piezotronic transistor. Illustration of the design of a large-scale cross-bar array device. The performance of an individual vertical piezotronic transistor unit under different strains. (c–e) High-resolution tactile e-skin sensor array with the ZnO NW piezotronic transistors. Reproduced with permission from ref 174. Copyright 2013 American Association for the Advancement of Science.

structure needs to be designed and fabricated to obtain a high-resolution tactile e-skin sensor which is comparable with the spatial resolution of our human skin. To realize an e-skin with very high spatial resolution, a good way is to remove the gate-electrode and change the traditional 3-terminal FET structured devices to 2-terminal crossbar electrodes devices

In sections 4.1–4.3, we have introduced a series of single NW piezotronic effect-based strain sensors based on wurtzite structure semiconductors, which can detect the pressure/strain very sensitively. In 2013, Wu, Wang, and co-workers reported a 2-dimensional, large-scale piezotronic transistor array based integrated circuit by using vertically aligned ZnO NWs as the active pressure sensor unit for real time tactile imaging. When a pressure is apply to the ZnO NW array, a piezopotential is created along the NW due to the noncentrosymmetry wurtzite structure, which can be used to serve as the driving force (similar to the gate voltage) and to control the charge transport properties at the interface, or the junction between the NWs and the electrodes (Figure 28a). Thus, it offers the possibility to decrease the number of electrodes and also can reduce the fabrication processes of fabricating a high-resolution tactile e-skin device with piezotronic effect. In this work, they reported  $92 \times 92$  tactile e-skin devices with a spatial resolution of  $100 \mu\text{m}$  and a lowest pressure sensitivity about 3.6 kPa. Each pixel is consisted with an individual Au-ZnO NW-Au transistor, as show in Figure 28.<sup>174</sup> Such a 8464 piezotronic transistors tactile e-skin device can map the strain or pressure directly by addressing each pixel with a scanning multichannel measurement system. Thus, a pressure distribution mapping can be acquired by measuring the current change for each pixel. Furthermore, the devices can be fabricated on flexible substrate and can also be used to map the strain on a flexible

device. The authors also firmly proved the devices are working with the principle of the piezotronic effect, not the piezo-resistive effect. The reason is that the  $I-V$  curves of the piezotronic transistors tactile pixel change asymmetrically before and after applying the strain, while the  $I-V$  curves of a typical piezo-resistive device change linearly and symmetrically.

#### 4.5. Piezotronic Effect-Enhanced Schottky-Contact Nanosensors

1D semiconductor nanomaterials have been extensively studied as basic building blocks for various sensor applications since they have large specific surface area, ultraflexibility, and easy surface functionalization. Surface adsorption of analytes induces carrier depletion or accumulation and changes the device electrical properties.<sup>129,175–182</sup> Earlier studies focused on the use of ohmic contacts for low dimensional nanostructures, and Schottky contacts were usually avoided to enhance the contribution made by NWs or nanotubes to the detected signal.<sup>183–191</sup> The surface energy states of a semiconductor are influenced by the electrostatic gating effect of the adsorption, resulting in electrical conductivity changes.<sup>97,192–201</sup> The sensitivity of ohmic-contact sensors depends on the interaction of analyte molecules and semiconductor properties. Carrying out precise structure control and assembly of sensors to achieve both high sensitivity and low contact resistance is difficult.<sup>79,202–208</sup> In this section, we will introduce various new types of sensors (UV sensors, biosensors, and gas sensors) based on the use of Schottky contacts to achieve a supersensitive and fast response; then, we will discuss how to further improve the performance of such

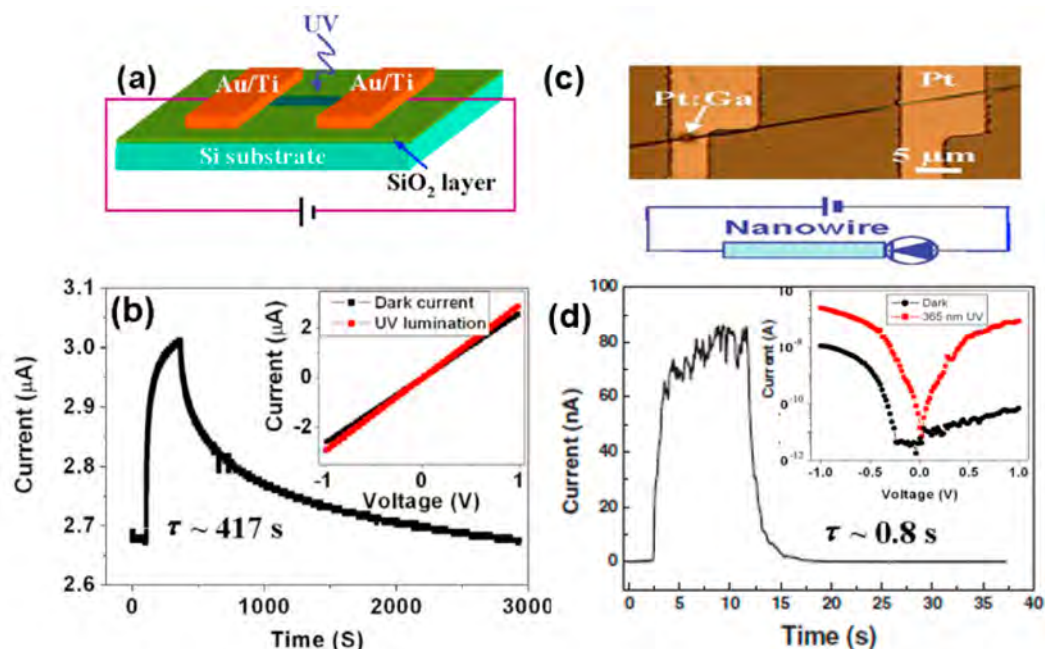


**Figure 29.** Schematic of ohmic-contact (a) and Schottky-contact (c) UV sensors. (b) Photoresponse properties of the ohmic-contact UV sensor. (d) Photoresponse properties of the Schottky-contact UV sensor. Reproduced with permission from ref 209. Copyright 2009 AIP Publishing.

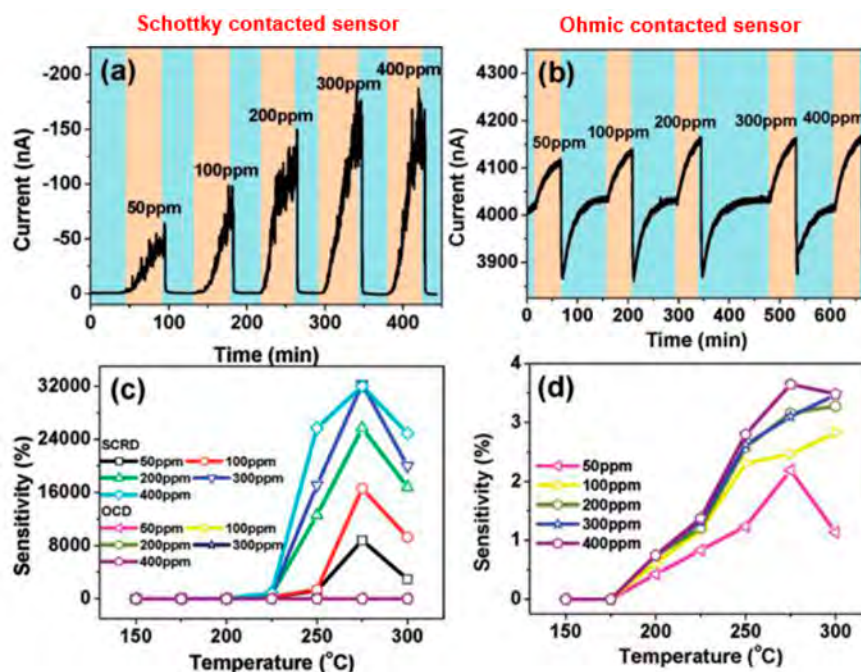


**Figure 30.** *I*–*V* characteristics and corresponding sensitivity of Schottky-contact (a and c) and ohmic-contact (b and d) gas sensors. Reproduced from ref 210. Copyright 2009 American Chemical Society.

Schottky contact NW based sensors via the piezotronic effect and piezophotonic effect.

**4.5.1. Highly Sensitive, Fast-Response NW Sensors with Schottky Contacts.** **4.5.1.1. Schottky-Contact ZnO NW UV Sensors.** Jun Zhou et al. demonstrated a Schottky contact UV detector based on ZnO NW with extremely high sensitivity, very fast response speed, and short reset recovery time.<sup>209</sup> By choosing different metal electrodes, we can make a Schottky contact or ohmic contact between the metal and a semiconductor. Thus, to give a direct comparison, Zhou et al. developed an ohmic-contact ZnO NW based UV detector with

Ti/Au electrodes at the two ends using shadow mask technology and a Schottky-contact ZnO NW UV detector with a Schottky barrier at the ZnO NW/Pt interface and the other contact at the ZnO/Pt:Ga interface remaining ohmic. Typical optical images of the two UV detectors are demonstrated in Figure 29a and c, in which Ti/Au electrodes and the Pt:Ga electrode make good ohmic contacts.

The photoresponses of the devices both in the dark (dark curves) and under  $\sim 30$  W/cm<sup>2</sup> UV light illumination (red curves) are displayed in the insets of Figure 29b and d. The Schottky-contact UV detector has a much higher responsivity

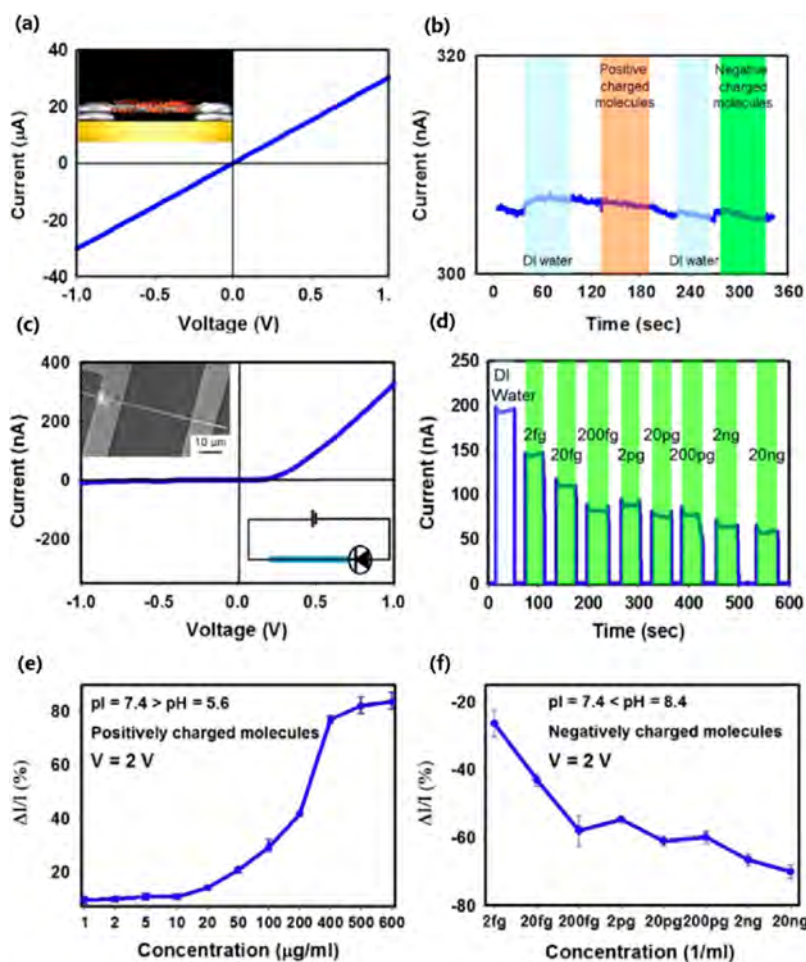


**Figure 31.** (a) Ohmic-contact device showing a very small response to biomolecules (the inset is a photograph of the device). (b) Electrical signal of the ohmic-contact device to either negatively or positively charged molecules. (c)  $I$ – $V$  characteristics of a Schottky-contact device and its corresponding SEM image (upper-left inset). (d) Responses of the Schottky-contact device to various concentrations of negatively charged molecules ( $pI$  7.4 <  $pH$  8.4). (e–f) Responses of the conductance of the device to positively charged and negatively charged molecules. Reproduced with permission from ref 211. Copyright 2009 John Wiley and Sons.

and faster response and recovery times. As seen in Figure 29b, the current of the ohmic-contact sensor only changes by approximately 9%, with a recovery time of 417 s. In contrast, for the Schottky-contact ZnO NW UV detector, the current increases approximately 1500-fold from 0.04 nA to 60 nA within 0.6 s. If the UV light is turned off, the current decreases to its initial state within 6 s, with a recovery time of 0.8 s. Therefore, the difference in device performance between the two types of nanosensors can be attributed to the Schottky barrier at the interface of ZnO/Pt heterostructure.

**4.5.1.2. Schottky-Contact ZnO NW Gas Sensors.** In 2009, Wei et al. also demonstrated ohmic contact gas sensors and Schottky-contact gas sensors using ZnO NWs. Similar to the UV detector in the last section, the two ends of the NW were fixed as ohmic contacts or Schottky contacts through focused ion beam (FIB) technology on a pair of Pt patterned electrodes.<sup>210</sup> The performance of gas sensing based on two types of gas sensors can be verified by the relevant  $I$ – $V$  curves at different temperatures and under different concentrations of gas, as shown in Figure 30. Taking CO as an example, the Schottky-contact gas sensors clearly have a very high sensitivity even when the starting concentration of CO is 50 ppm, with the current greatly changing and the sensitivity increasing with increasing CO concentration. Such reverse bias Schottky-

contact sensors clearly show high sensitivity and good temperature-dependent behavior, reaching the highest sensitivity of 32000% under a CO concentration of 400 ppm at 275  $^{\circ}\text{C}$ , as shown in Figure 30c. There is a drop-in sensitivity with a further increase of the environment temperature due to the difference of activation energies corresponding to the gas adsorption and desorption processes. For the ohmic-contact gas sensors, the current of the devices also increases with increasing concentration of CO. However, the current only changes by approximately 2–4%, which is much lower than the sensitivity of the Schottky-contact sensors.

**4.5.1.3. Schottky-Contact Molecular Sensors.** Yeh and Wang introduced an asymmetric Schottky contact at the end of an individual VLS-fabricated ZnO NWs nanodevice and investigated its response to biomolecules. Similar to the previously introduced devices, a long single crystal ZnO NW was transferred onto a Pt patterned electrode with one or two ends fixed using the FIB technique.<sup>211</sup>

For the ohmic-contact molecular sensors, the conductance of the NW device changes when the target molecule is absorbed onto the NW. A digital photo and a typical  $I$ – $V$  curve of the ohmic-contact device are given in Figure 31a. Hemoglobin was used as the target molecule, and the response of the ohmic contact molecular sensors was measured. When

negatively (green colored) or positively (brown colored) charged molecules were added at a concentration of  $800 \text{ mg mL}^{-1}$ , the conductance of the device showed little change, as shown in Figure 31b.

In contrast, for the Schottky-contact device, the two electrodes contacted by the ZnO NW were a Pt electrode (Schottky contact) and a Pt–Ga electrode (ohmic contact). A typical  $I$ – $V$  curve of the Schottky-contact molecular sensor and its effective circuit diagram are given in Figure 31c. The molecules were dispersed in deionized water at different concentrations, under a fast reaction, and with significant current changes, as shown in Figure 31d. Only a few molecules are needed to change the SBH. The device was also immersed in DI water for calibration and reference.

The electrical response of a Schottky-contact device was characterized for a series of concentrations of charged molecules. For hemoglobin with an isoelectric point (pI) of 7.4, the conductance increased if the molecules were positively charged (pH 5.6), as shown in Figure 31e. The lower detection limit of the device is  $10$ – $20 \text{ mg mL}^{-1}$ , and the upper detection limit is ca.  $500 \text{ mg mL}^{-1}$ . On the contrary, the conductance decreased when the molecules were negatively charged at pH 8.4 (Figure 31f). The detected concentrations range from  $2 \text{ fg mL}^{-1}$  to  $20 \text{ ng mL}^{-1}$ , with the conductance displaying a distinct decrease due to the presence of negatively charged molecules. Both measurements were taken under a fixed bias voltage of  $2 \text{ V}$ .

The electrical response of the Schottky-contact molecular sensors is evidently much larger compared to that of the ohmic-contact molecular sensors for the same type of ZnO NWs. Owing to the nature of the charge and potential profile at the junction region, the Schottky-contact device is likely to exhibit some selectivity in detecting positively charged molecules versus negatively charged molecules because only a few molecules can change the barrier width and height that can effectively tune the conductance.

**4.5.2. Piezotronic Effect-Enhanced Schottky-Contact Sensors.** In section 4.5.1, we demonstrated that three types of Schottky-contact sensors (UV, gas, and biochemical sensors) exhibit an enhanced sensitivity and a rapid response time simply because the performance of the Schottky-contact devices is determined by the local contact, instead of the size or length of NW (Figure 32a–b).<sup>212</sup> In such a case, a Schottky-contact device with a relatively large and long NW is much easier to fabricate without sacrificing the sensitivity. Since the barrier width and height are easily tuned by the adsorbed species, a superhigh sensitivity Schottky-contact sensor can be realized by controlling the carrier transport process.

Now the key question is what is the optimized height of the SBH in such Schottky-contact devices? A very high SBH will block the current from flowing, while an ultralow SBH device is close to an ohmic-contact one. A small change of the SBH will greatly change the transport current, following an exponential relationship. As shown in Figure 32d–e, for materials with wurtzite structure, the SBH can be modulated through the piezotronic effect. In the following section, we will introduce how to further improve the device performance of Schottky-contact sensors with the piezotronic effect by applying a strain/stress to the sensor.

**4.5.2.1. Piezotronic Effect-Enhanced Schottky-Contact pH Sensors.** In 2013, Pan and Wang and co-workers reported an M–S–M Schottky-contact ZnO NW pH sensor to demonstrate how the piezotronic effect modulates the performance

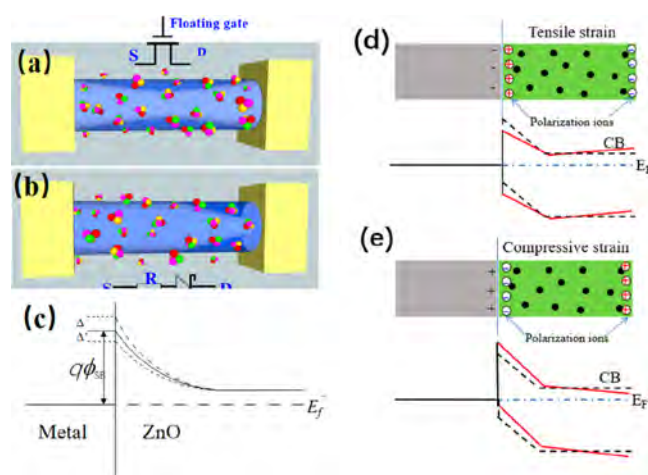


**Figure 32.** (a–b) Comparison of the principles of an ohmic-contact NW sensor and a Schottky-contact NW sensor. Reproduced from ref 212. Copyright 2013 American Chemical Society. (c) Energy band diagram showing the dependence of the transport property on the variation in the SBH at the interface of an M–S contact. (d–e) Energy band diagram showing the piezotronic effect at the interface of an M–S contact. Reproduced with permission from ref 6. Copyright 2012 John Wiley and Sons.

and sensitivity. The fabrication of the ZnO NW pH sensor followed the method reported in section 4.5.1. A long ZnO NW was transferred onto a PET substrate. Two ends of the NW were connected with silver paste and then covered by an epoxy layer. An optical microscopy image and a photograph of the as-fabricated device is presented in Figure 33a1 and a2, respectively. The performance of the NW pH sensor was examined through testing the transportation properties in various solutions with pH 3–12. When no strain was applied, the response of the pH sensor decreases stepwise in the nA range with discrete changes in pH from 3 to 12.

As shown in Figure 33b, both the signal and the sensitivity of the pH sensor are increased upon external strain due to the piezotronic effect. If a pH sensor was tested in a pH 5 buffer solution with a bias of  $0.5 \text{ V}$ , the current was  $1.2 \text{ nA}$  in strain-free condition and then increased to  $1.75 \mu\text{A}$  upon the applied compressive strain ( $\epsilon = -0.92\%$ ), showing a very large enhancement. The signals of the pH sensor under various solutions with different pH ranges with an applied strain of  $\epsilon = -0.92\%$  (blue curve) and without strain (red curve) are shown in Figure 33c. The results can be attributed to the SBH at both the source and drain ends being tuned by the piezotronic effect.

**4.5.2.2. Piezotronic Effect-Enhanced Schottky-Contact Protein Sensors.** Yu, Wang, and co-workers reported how the piezotronic effect controlled the response of a ZnO NW-based protein sensor using an M–S–M Schottky contact.<sup>213</sup> Figure 34a shows the SEM images of the as-fabricated ZnO NWs. To form a flexible Schottky-contact device, a single ZnO NW was transferred to a PET substrate with two ends connected with gold nanoparticle-anti-immunoglobulin G conjugates (Au NP-anti-IgG) (Figure 34b). It can be seen from Figure 34c, the response of the device significantly increased from nA to several  $\mu\text{A}$  under higher concentrations, and more target protein IgGs were connected to the surface of the ZnO NW, thus demonstrating the anti-IgG-decorated ZnO NW protein sensor is sensitive to IgG concentration.

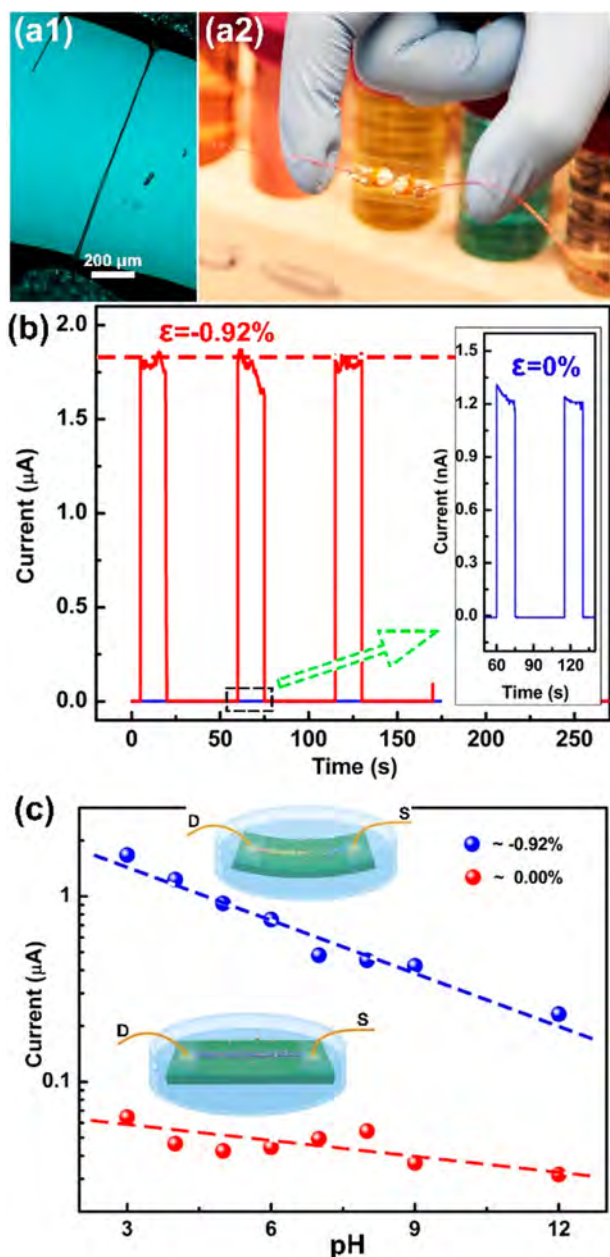


**Figure 33.** (a1, a2) Optical microscopy of a ZnO NW and photograph of a ZnO NW based pH sensor. (b) Performance of a pH sensor in a solution of pH = 5 (blue: strain-free condition, red: applied strain with  $\epsilon = -0.92\%$ ). (c) Signals of the pH sensor to the full pH range. The sensor has a much better performance when it is strained (blue) compared to the strain-free state (red). Reproduced from ref 212. Copyright 2013 American Chemical Society.

The modulation of these ZnO NW protein sensors by the piezotronic effect was examined when the ZnO NW device was compressively strained. The results of a systematic investigation on the sensor response to different external strains and target protein concentrations are shown in Figure 34d, which depicts the current responses of the ZnO NW protein sensor under specific strains and IgG concentrations. The current clearly increases as the IgG concentration or external strain increases. Detailed data are shown in four 2D graphs (Figure 34e–h). Higher sensitivities of the ZnO NW device are observed at increased compressive strain and IgG concen-

tration, indicating that the use of the piezotronic effect is a potential approach to enhance the performance of a biosensor.

In addition to the two above-mentioned demonstrations, several other Schottky-contact sensors have been reported. In 2014, Hu, Pan, Wang, and co-workers produced a piezotronic effect-enhanced humidity sensor.<sup>108</sup> The sensitivity and signal level of the ZnO NW humidity sensor were dramatically increased when an external strain was applied by the piezotronic effect. An optimum compressive strain of 0.22% can improve the performance of the humidity sensing around 1,240%. In 2015, Zhou, Pan, Wang, and co-workers reported a piezotronic effect-enhanced gas sensor for H<sub>2</sub> and NO<sub>2</sub> sensing.<sup>107</sup> By applied external strain, both the resolution and sensitivity were largely enhanced, besides there being dramatic improvement of the output current by 238.8% for NO<sub>2</sub> and 5,359% for H<sub>2</sub> detection. In 2013, Yu, Pan, Wang, and co-workers reported a piezotronic effect-enhanced glucose sensor, whose sensitivity and sensing resolution were enhanced over 300% and 200%, respectively, when applying a  $-0.79\%$  compressive strain to the device.<sup>214</sup> In 2015, Han, Cao, Wang, and co-workers reported a piezotronic effect-enhanced chemical sensor for sensing the H<sub>2</sub>O<sub>2</sub> released by cells.<sup>215</sup> Their results showed that the piezotronic effect can dramatically increase both the sensitivity and the sensing resolution of the H<sub>2</sub>O<sub>2</sub> sensor. The determination limit was as low as 2 nM, which could be used for the detection of the trace amount of H<sub>2</sub>O<sub>2</sub> released by cells. In 2016, Cao, Wang, and co-workers demonstrated a piezotronic effect-enhanced label-free DNA sensor, in which the signal level could be greatly enhanced by 454% when a small  $-0.59\%$  compressive strain was applied to the ZnO NW-based DNA sensor.<sup>216</sup> These demonstrations indicate that piezotronic effect enhanced Schottky-contact ZnO NW sensors may have a bright future, are promising for many applications to improve the sensing resolution, the sensitivity, and the signal of NW sensors, and could possibly provide a way to build self-powered device systems.

## 5. PIEZO-PHOTOTRONICS AND ITS APPLICATIONS

### 5.1. Piezo-phototronic Effect in Solar Cells

Solar cells are one of the best optoelectronic applications. With application potential in the fields of energy and mobile devices, solar cells have been widely studied by researchers in recent years.<sup>138</sup> Using semiconductor NWs to fabricate PV cells is an important way to increase the energy conversion efficiency because of the advantages of NWs, such as good charge collection ability, large specific surface, and increased absorption ability by light trapping.<sup>136,217–222</sup> Additionally, new means to decrease the nonradiative recombination of the photoinduced carriers and thus enhance the device efficiency of such NW devices are emerging. Similar to the optical carrier separation and transport processes, the solar cell efficiency can also be regulated through the energy band at the junction area of the device, which is reduced by the piezoelectric potential through the piezo-phototronic effect. Therefore, we will show the principles of the piezo-phototronic effect and its influence on the NW solar cells performance.<sup>223–228</sup>

**5.1.1. Fundamentals of Piezo-phototronics in Solar Cells.** III–V zinc blende (ZB) or III–V wurtzite (WZ) core-shell NWs, consisting of different piezoelectric materials, have been investigated as a new means to obtain radial p–n junctions. In the epitaxial growth process,<sup>229</sup> the lattice

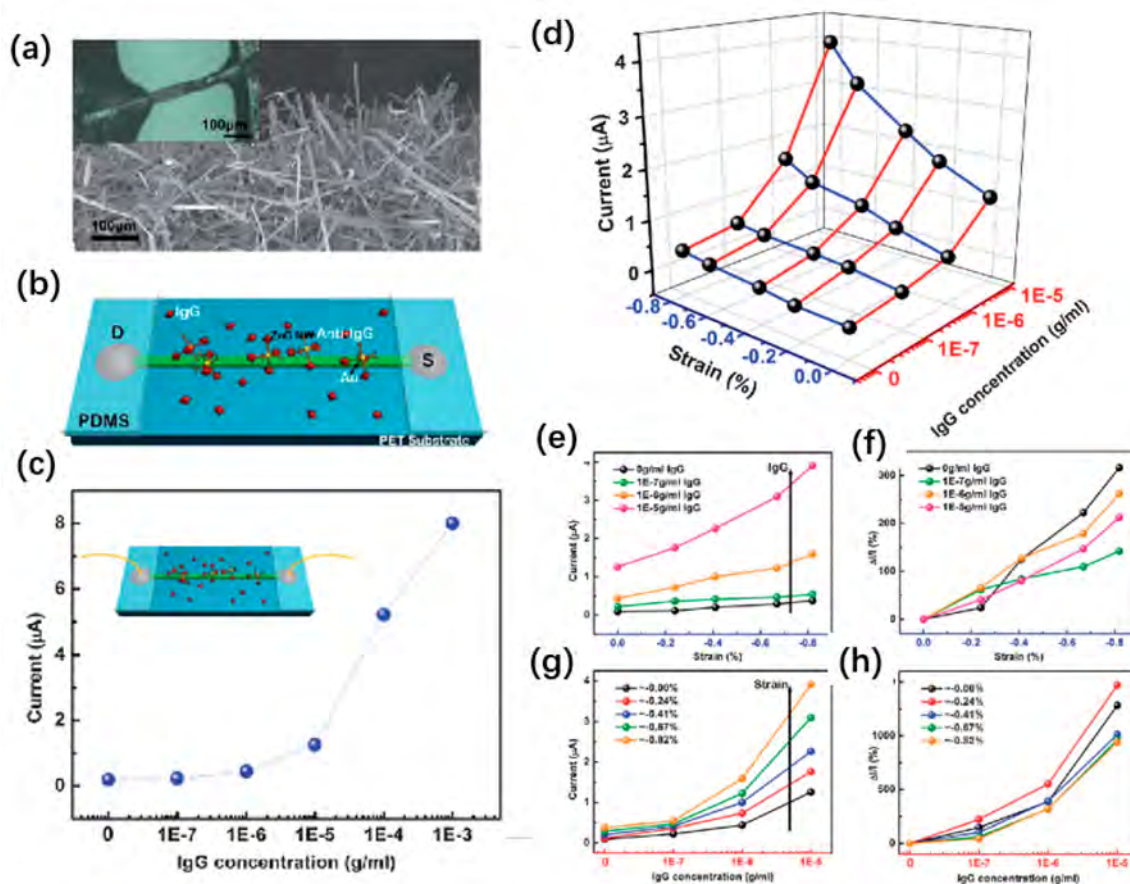


**Figure 34.** (a) SEM image of VLS-fabricated ZnO NWs. (b) Cartoon illustration showing a Au-NP-anti-IgG-surface-decorated ZnO NW protein sensor. (c) Current signal responses to the target protein IgG concentration (varying from 0 to  $10^{-3}$  g mL $^{-1}$ ) of a strain-free single ZnO NW sensor. (d–h) Influence of the piezotronic effect on the response of ZnO NW protein sensors under different strains and IgG concentrations. Reproduced with permission from ref 213. Copyright 2013 Royal Society of Chemistry.

mismatch between the shell and core materials will introduce an elastic strain at the interface of the core–shell NW, resulting in piezoelectric polarization and thus generating an internal piezoelectric field through the radial direction of the NW p–n junctions. According to the electroelastically coupled continuum elasticity equations, Xu's group studied the analytical model and performed numerical simulations of the piezoelectric polarization in a InAs/InP core–shell NW, where the core–shell NW was grown along the [111] crystallographic orientation.<sup>230</sup> The length ( $L_z$ ) of the NW was approximately 350 nm, the core radius ( $r_c$ ) was 30 nm, while the outer shell radius ( $r_s$ ) was 50 nm. Subsequently, a similar analytical model and numerical simulations of the GaAs/GaP core/shell NW were also investigated.

Figure 35a–b shows the numerically computed distributions of the strain components  $\epsilon_{xx}$  and  $\epsilon_{zz}$  at the  $x$ – $z$  cross section of the ZB InAs/InP core–shell NW. The strain component  $\epsilon_{yy}$  is omitted because it is similar to  $\epsilon_{xx}$  with a rotation of  $\pi/2$  around the  $z$  axis. The strain components  $\epsilon_{xx}$  and  $\epsilon_{yy}$  are constant and are only nonzero in the core area, whereas  $\epsilon_{zz}$  gradually becomes constant along the  $z$  axis. Figure 35c illustrates the numerically computed effective piezoelectric charge density, which is discontinuous at the interface of core/shell materials due to the discontinuous relative permittivities of the different materials. Figure 35d clearly shows that the axial piezoelectric field induced by the inner strain of compound semiconductor core–shell NWs can be used to

modulate the photocurrent through the NW. In addition, the magnitude of the piezoelectric field depends on not only the shell and core materials but also the ratio of the core and shell radii. Figure 35e shows large-area core–shell NW array based solar cells, in which the back contact is a heavily doped semiconductor substrate and the top contact is a transparent conducting film. If the solar cell is exposed to sunlight, photogenerated carriers (electrons and holes) will be separated by the piezoelectric potential generated in the core–shell NWs, and therefore, a photocurrent will be created in the circuit. These proposed core–shell NWs possess an inherent piezoelectric property, which can be efficiently employed for solar energy conversion. In addition, the new design of a core–shell NW-based solar cell has obvious advantages in terms of device fabrication compared with previous PV devices based on NWs, for which a p–n junction is essential.

InGaN, with a high carrier mobility, a high absorption coefficient ( $10^5$  cm $^{-1}$ ), a large saturation velocity, and strong radiation resistance, is a potentially good candidate for high-performance solar cells since it has a wide direct bandgap (0.7–3.4 eV), which covers most of the solar spectrum. Since the synthesis of ideal p-InGaN for application in solar cells is limited by several key factors, a p-GaN/n-In $_x$ Ga $_{1-x}$ N junction was proposed to replace the homojunction. However, the large amount of piezoelectric charges ( $P_{pz}$ ) in the GaN/In $_x$ Ga $_{1-x}$ N heterojunction will generate a piezoelectric field, which opposes the built-in electric field arising from the p–n

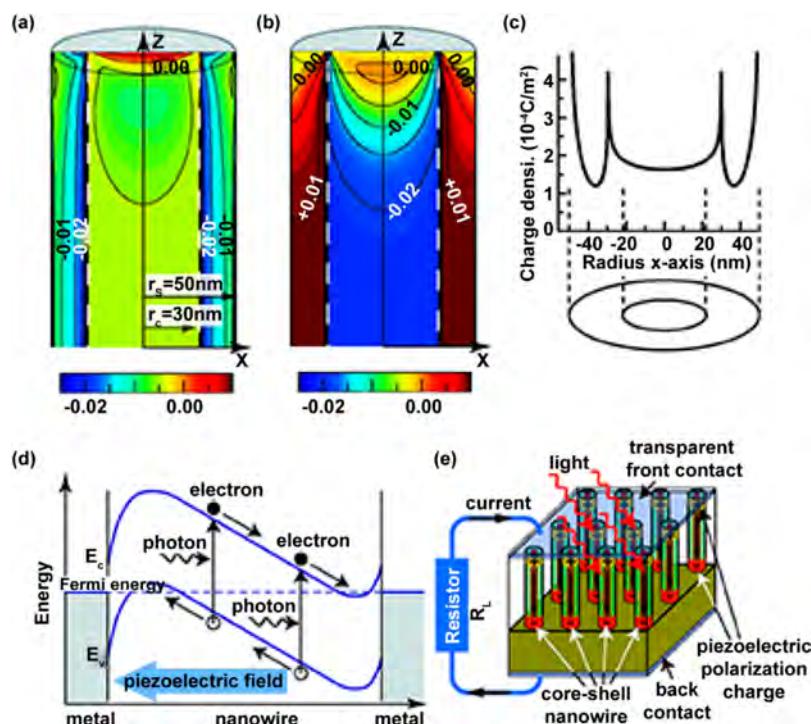


**Figure 35.** Components of strain (a)  $\epsilon_{xx}$  and (b)  $\epsilon_{zz}$  at the  $x$ - $z$  cross section of a cylindrical InAs/InP core-shell NW along the  $[111]$  direction. (c) Effective surface charge density in the InAs/InP core-shell NW. (d) Schematic illustration of the band diagram and the PV characteristics of a PSC based on the InAs/InP core-shell NW. (e) Schematic diagram of a solar cell device based on a piezoelectrically polarized core-shell NW array grown on a conductive substrate. Reproduced from ref 230. Copyright 2010 American Chemical Society.

junction and thus decreases the carrier collection efficiency. A. T. M. Golam Sarwar and co-workers demonstrated that for a p-GaN/unintentionally doped (UID)-In<sub>0.3</sub>Ga<sub>0.7</sub>N NW-based solar cell, the maximum numerically simulated strain components  $\epsilon_{xx}$  and  $\epsilon_{zz}$  are 1.69% and 1.11%, respectively.<sup>231</sup> Figure 36a illustrates that the valence band at the p-GaN/n-InGaN interface is discontinuous and that the increased energy barrier impedes hole transport, resulting in a degraded performance of the solar cell. To avoid this deterioration, a buffer layer was inserted between the n-InGaN and p-GaN absorption layers, as shown in Figure 36b. The strain in the graded NW junction is smaller compared to that in the abrupt NW junction due to the spontaneous polarization charge ( $P_{sp}$ ) of the NW uniformly distributed in this graded junction. Here, the maximum strain components  $\epsilon_{xx}$  and  $\epsilon_{zz}$  are 0.18% and 0.48%, respectively, which are approximately 6 times smaller than those in the abrupt heterostructure. Meanwhile, the conduction band and valence band from p-GaN to UID n-InGaN become smooth, as shown in Figure 36c. In this structure, the UID-InGaN buffer layer becomes p-type under the effect of  $P_{sp}$ . In addition, the strain-induced piezoelectric charge  $P_{pz}$  can increase the hole concentration and the built-in potential, accordingly enhancing the efficiency and power density of the graded NW solar cell, as can be seen from the black line in Figure 36d. This work investigated the effect of piezoelectric charges on two different solar cells and proposed a new mean to increase the overall performance of NW solar cells through exploiting piezoelectric charges in the p-type InGaN graded region.

### 5.1.2. Piezo-phototronics in Thin Film Solar Cells.

Organic/inorganic solar cells have become one of the promising and most interesting research fields due to their special properties arising from the combination of organics

with semiconductors. Wen, Wang, and co-workers reported a solar cell system with the structure of ZnO/P3HT and demonstrated that the performance of the solar cells was influenced by the piezo-phototronics.<sup>141</sup> As the band structure under strain in Figure 37a shows, when an external strain/stress is applied to the ZnO thin film, the negative piezoelectric charges at the ZnO/P3HT interface increase not only the conduction band but also the valence band at the junction area and decrease the value of the built-in field, which will tune the performance of such film solar cells.<sup>141</sup> Furthermore, five series of samples fabricated under various conditions were tested and compared. The enhancement of the solar cell performance was determined to be due to the efficient piezo-phototronic effect under the optimized parameters. Another organic/inorganic structure using a ZnO micro/NW and poly(3,4-ethylenedioxythiophene)/polystyrenesulfonate (PEDOT:PSS) on a flexible PS substrate was studied by Yue Zhang and co-workers as a solar cell device controlled by the piezo-phototronics. Steve Dunn and co-workers investigated the influence of acoustic vibration on the characteristics of PV devices using a polymer/ZnO nanorod system.<sup>232</sup> They prepared five types of ZnO nanorods with different aspect ratios and fabricated P3HT/ZnO nanorod heterojunction solar cells. An obviously enhanced performance and a longer decay lifetime (from 0.34 to 0.88 ms) were observed in the device under external vibration ( $\sim 10\text{ kHz}$ ), and analogous properties were also found in other polymer/ZnO systems, which means that the enhancement observed under acoustic stress is due to charge separation at the polymer/ZnO heterojunction interface.

Furthermore, the piezo-phototronics adjusts the energy band structure of the junction such that the performances of ZnO/PbS quantum dot (QD) film PV solar cells are modulated, as reported by Xudong Wang's group (Figure 37b).<sup>226</sup> They

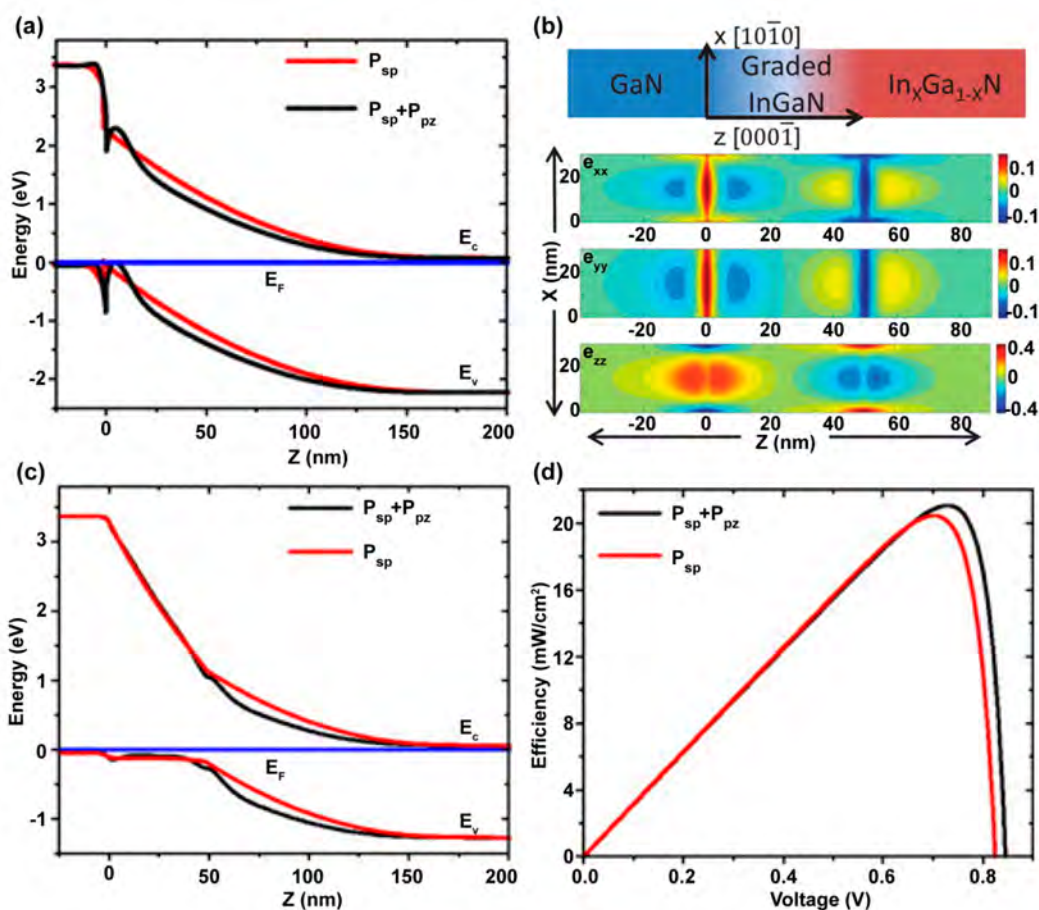


**Figure 36.** (a) Schematic illustration of the equilibrium energy band diagram of a p-GaN/UID-InGaN NW solar cell. (b) Schematic diagram and distribution (In%) of the strain components ( $e_{xx}$  and  $e_{zz}$ ) of a GaN/graded-InGaN/InGaN NW solar cell. (c) Equilibrium energy band diagram of a p-GaN/UID-graded InGaN/UID-InGaN NW solar cell. (d) Power density as a function of voltage of a GaN/UID-graded InGaN/UID-InGaN NW solar cell. Reproduced with permission from ref 231. Copyright 2012 AIP Publishing.

discovered enhanced characteristics of n-ZnO/p-PbS-based QD PV devices by introducing  $P_{pz}$  at the heterojunction interface. The results clearly show that the efficiency of the QD solar cell under both illumination cases can be increased by an external compressive strain. The interfacial band structure of the ZnO/QD device is modulated by the potential, which thus induces charge redistribution at the ZnO/PbS QD interface, leading to the enhancement of  $J_{sc}$  and efficiency. This research provides a new means to enhance the PV efficiency of QD based solar cells and improve the electrical transport performance of heterojunction solar cells. Similar to the studies discussed above, Tang and co-workers reported an InGaN QD-based PV device and performance modulation through the piezo-phototronic effect (Figure 37c).<sup>233</sup> The best energy conversion efficiency was 55.4% with the  $\text{In}_{0.4}\text{Ga}_{0.6}\text{N}$ : barrier/ $\text{In}_{0.8}\text{Ga}_{0.2}\text{N}$ : QD-based IBSC structure. The presented results demonstrate a new method for designing InGaN-based solar cells with ultrahigh energy conversion efficiency.

**5.1.3. Piezo-phototronic Effect in NW Solar Cells.** Solar cells based on piezo-phototronic NWs (ZnO) have been recently reported by researchers. Such reports offer a new method to improve the solar energy conversion efficiency by using piezo-phototronic NW devices. First, we will introduce a new n-CdS/p-Cu<sub>2</sub>S coaxial NW PV device with the properties of the devices controlled by the piezo-phototronics, as demonstrated by Pan, Wang, and co-workers. The device

fabrication process is shown in Figure 38. A CdS (blue) NW with a metal contact at one end is partially immersed into CuCl solution to form a layer of Cu<sub>2</sub>S (pink) shell, and then, a metal contact at the other end is fabricated on the Cu<sub>2</sub>S shell.<sup>234</sup> The polymer masking step is not shown. The piezo-phototronics can modulate the generation, transport, separation, and recombination processes of electron–hole pairs, thereby enhancing the output properties of the PV devices by at least 70% when a  $-0.4\%$  external compressive strain is applied to the NW.

Tremendous efforts have been recently made to enhance the power conversion efficiencies (PCEs) of hybrid organic–inorganic PSCs. Currently, the best reported value is now over 20%. However, further improvement of the PCEs of PSCs is hindered by the material properties, device stability, and packaging technologies. In 2016, Hu, Pan, Wang, and co-workers reported a flexible ZnO/perovskite solar cell. The direction of the  $c$ -axis of ZnO plays a very important role in such piezo-solar cells, and the  $c$ -axis pointing from the perovskite to the ZnO side is taken as an example (see the inset of Figure 39a–b).<sup>235</sup>

Benefiting from the piezo-phototronic effect due to the application of an external static mechanical strain, we can see that the performance (mainly the short-circuit current) is increased with increasing external compressive strain (Figure 39a and c) and decreased with increasing external tensile strain

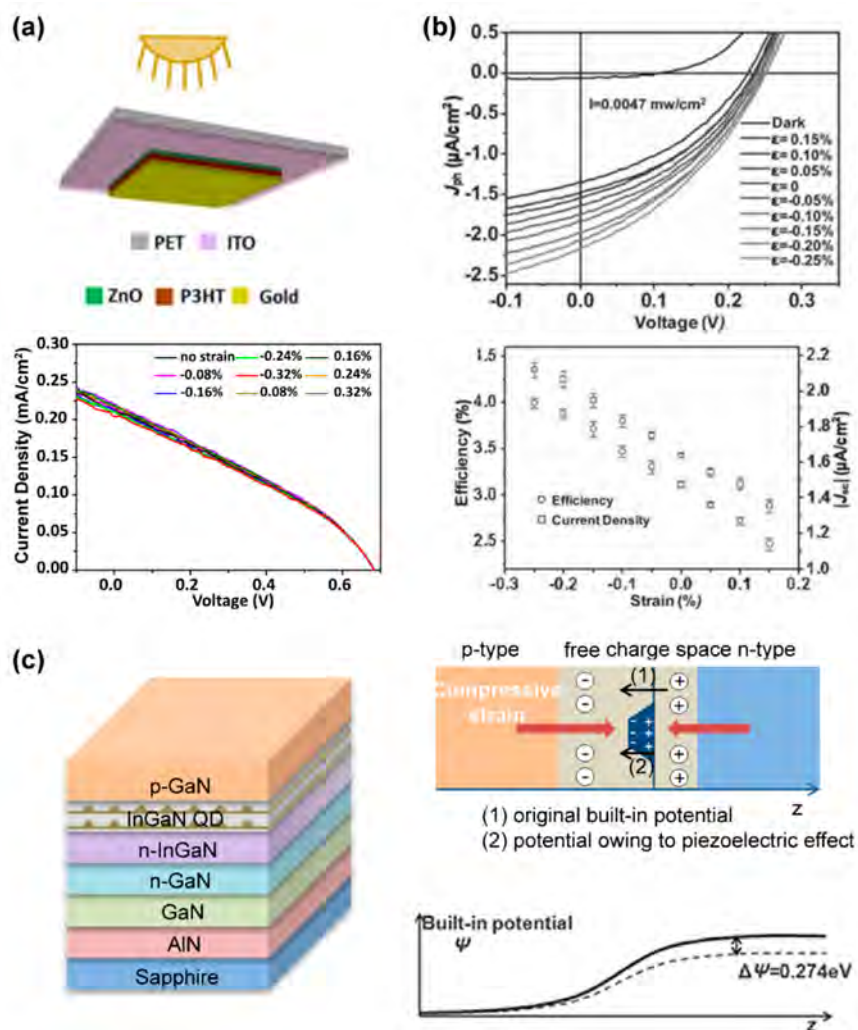


**Figure 37.** Piezo-phototronics in a film-based solar cell. (a) Schematic graph of the ZnO/P3HT film solar cell structure and  $J$  as a function of voltage under different applied external strains at a fixed illumination. Reproduced with permission from ref 141. Copyright 2013 Elsevier Ltd. (b)  $J$  as a function of voltage for a ZnO/PbS QD solar cell under light illumination subjected to various external tensile and compressive strains, and plot of the strain-tuned QD solar cell efficiency (open circles) and  $J_{sc}$  (open squares). Reproduced with permission from ref 226. Copyright 2012 John Wiley and Sons. (c) Schematic diagram of the electric fields in the p–n junction of an InGaN QD-based solar cell and the built-in potential. The solid line corresponds to consideration of the piezoelectric fields, while the dashed line corresponds to neglect of the piezoelectric fields. Adapted with permission from ref 233. Copyright 2015 IOP Publishing Ltd.

(Figure 39b and d). The related open-circuit voltage, short-circuit current, and efficiency were increased by 25.42%, 629.47% and 1280% under an external compressive strain of  $-0.8\%$ , respectively, without changing the components of the materials or device structure. Alternatively, if the  $c$ -axis points from the ZnO to the perovskite side, then a tensile strain will improve the performance of such a solar cell. This work offers an effective method to further improve the performance of such solar cells, even after the solar cell fabrication process has been finished.

**5.1.4. Piezo-phototronic Effect in NW Array Solar Cells.** The piezoelectric potential of a ZnO NW array can promote the separation and transport of photoinduced carriers via the adjustment of the band structure at the heterojunction in a core–shell NW. Zhu, Wang, and co-workers first reported a large-scale flexible n-ZnO/p-SnS core–shell NW array PV device with improved properties due to the piezo-phototronic effect.<sup>236</sup> This kind of NW array based solar cells has an enhanced efficiency over 37% by applying a moderate vertical

pressure through the piezo-phototronics effect. More importantly, the results of this research show a new way to dramatically improve the performance of large-scale flexible NW based solar cells via the piezo-phototronics (Figure 40).

Furthermore, a new nanoheterostructure PV device based on silicon, the most widely used material in industry, was fabricated by Zhu, Wang, and co-workers.<sup>237</sup> The performance of the (p+-Si/p-Si/n+-Si and n-Si)/n-ZnO NW array device was improved by the piezo-phototronic effect via dramatic enhancement of the light absorption of the NW array and charge carrier separation. The strain-induced piezopotential at the n-doped Si-ZnO interface can dramatically tune the related band structure and the electron trapping in the n+-Si/n-ZnO NW heterostructure. Therefore, this process enhances the transport process of local charge carriers. The efficiency of the Si solar cell is increased from 8.97% to 9.51% when applying an external compressive strain. This work shows that piezo-phototronics has not only a very large economic impact but also practical importance in the Si-based device industry.

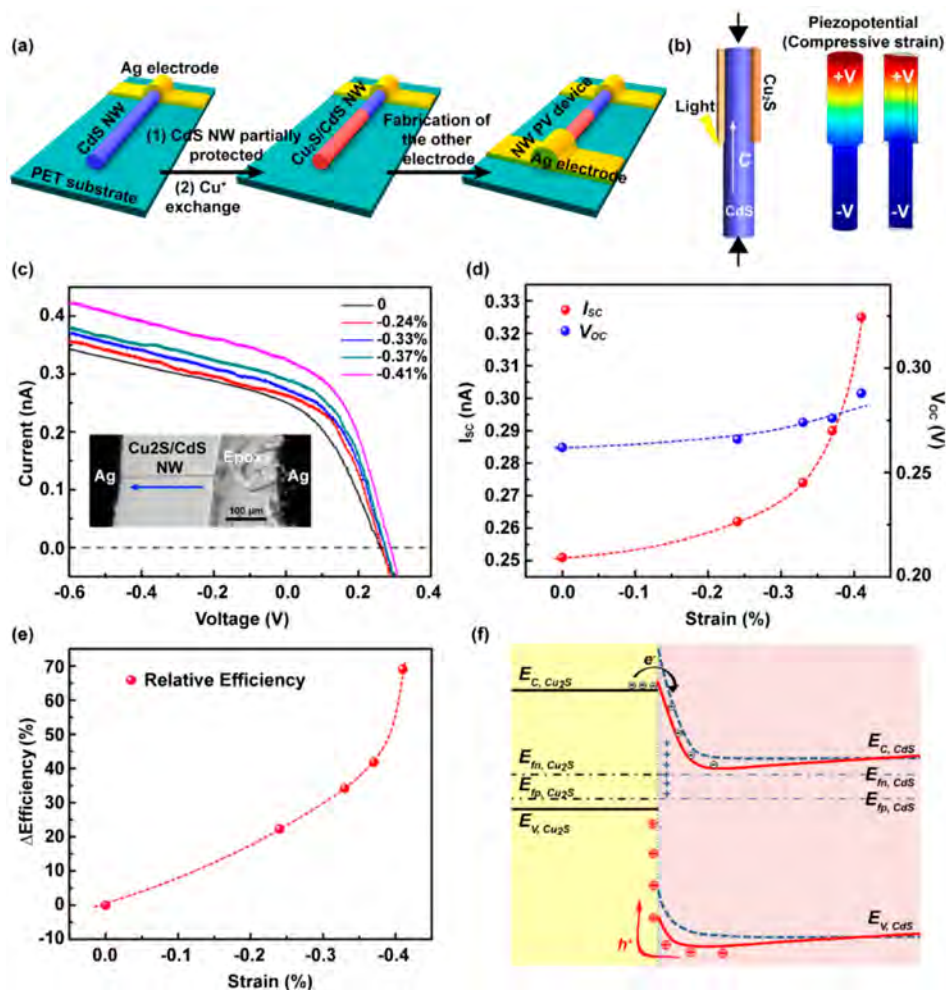


**Figure 38.** (a) Schematic of the fabrication process for a CdS/Cu<sub>2</sub>S coaxial NW solar cell. (b) Schematic and COMSOL simulation of the piezopotential distribution of a core–shell NW solar cell under external compressive strain. (c) *I*–*V* characteristics of the CdS/Cu<sub>2</sub>S coaxial NW solar cell under various external compressive strains, and the inset shows an image of the Cu<sub>2</sub>S/CdS coaxial NW solar cell obtained by optical microscopy. *V*<sub>oc</sub>, *I*<sub>sc</sub> (d), and relative energy efficiency (e) changes as a function of the applied external strain. (f) Energy band diagram of a CdS/Cu<sub>2</sub>S coaxial NW solar cell under compressive strain. Reproduced from ref 234. Copyright 2012 American Chemical Society.

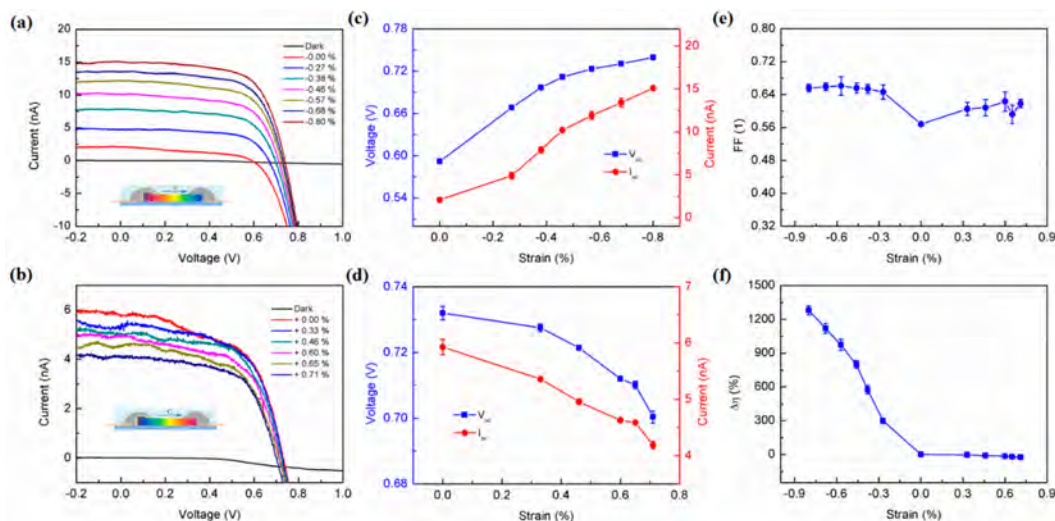


**Figure 39.** Piezo-phototronics-tuned flexible ZnO/perovskite solar cell. (a, b) *I*–*V* characteristics of the solar cell under applied external compressive strain (a) and applied external tensile strain (b). (c, d) Relationship between the short-circuit current and the open-circuit voltage upon application of an external compressive strain (c) and an external tensile strain (d). (e, f) Strain-induced fill factor (e) and relative efficiency change (f). Reproduced with permission from ref 235. Copyright 2016 Elsevier Ltd.

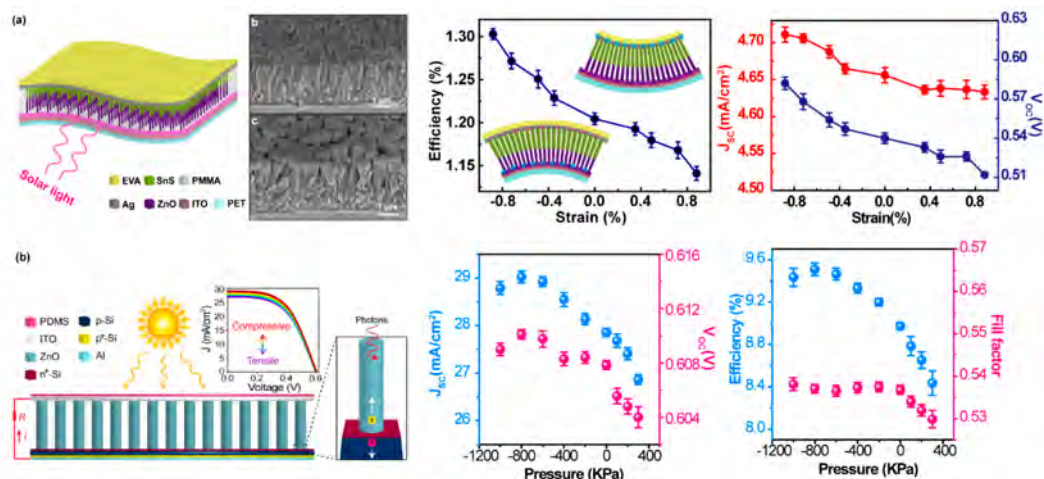


**Figure 40.** Piezo-phototronics in two kinds of NW array solar cells: (a) The structure design, an SEM image, and the performance (efficiency,  $V_{oc}$  and  $I_{sc}$ ) of a flexible n-ZnO/p-SnS core-shell NW array solar cell under different strains. Adapted with permission from ref 237. Copyright 2017 John Wiley and Sons. (b) The structure design and performance (FF, efficiency,  $V_{oc}$  and  $I_{sc}$ ) of an n<sup>+</sup>-Si/n-ZnO NW heterostructure solar cell under different strains. Reproduced from ref 236. Copyright 2017 American Chemical Society.

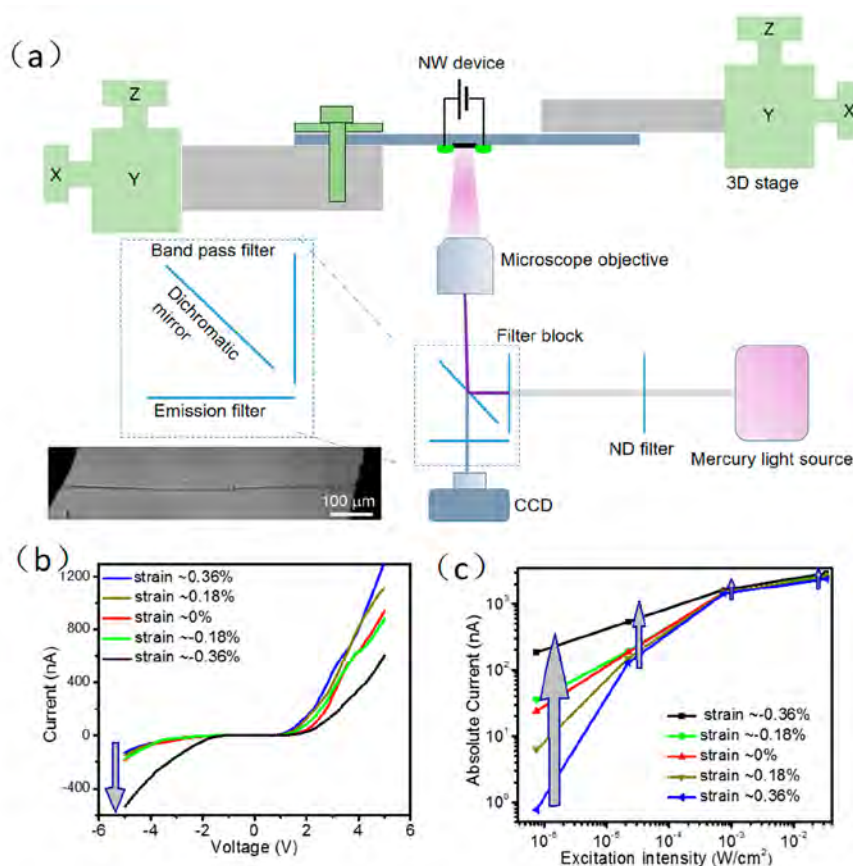


**Figure 41.** (a) Schematic graph of the testing setup for measuring the influence of the piezo-phototronic effect on photodetectors. The inset is a photograph of an individual ZnO NW-based photodetector. (b) For an excitation light intensity of  $2.2 \times 10^{-5}$  W/cm<sup>2</sup>, the  $I$ - $V$  characteristic of the ZnO NW sensor under different strains. (c) Absolute photoresponse corresponding to illumination under various strains. Reproduced from ref 243. Copyright 2010 American Chemical Society.

## 5.2. Piezo-phototronic Effect in Photodetectors

The core of piezo-phototronic optoelectronics is tuning the charge generation, transportation, separation, and recombination processes at the interface to enhance the optoelectronic performance by piezoelectric potential.<sup>126,127,238–242</sup> In this section, we discuss how the piezo-phototronic effect affects the

performance of a NW-based photodetector. This research field began with the first work of Yang, Wang, and co-workers in 2010.<sup>48</sup> The ZnO NW photodetector has an M-S-M structure, and the measurement setup is illustrated in Figure 41a.<sup>125</sup> The responsivity of the ZnO NW-based photodetector is enhanced up to 530% under 4.1 pW UV light illumination of

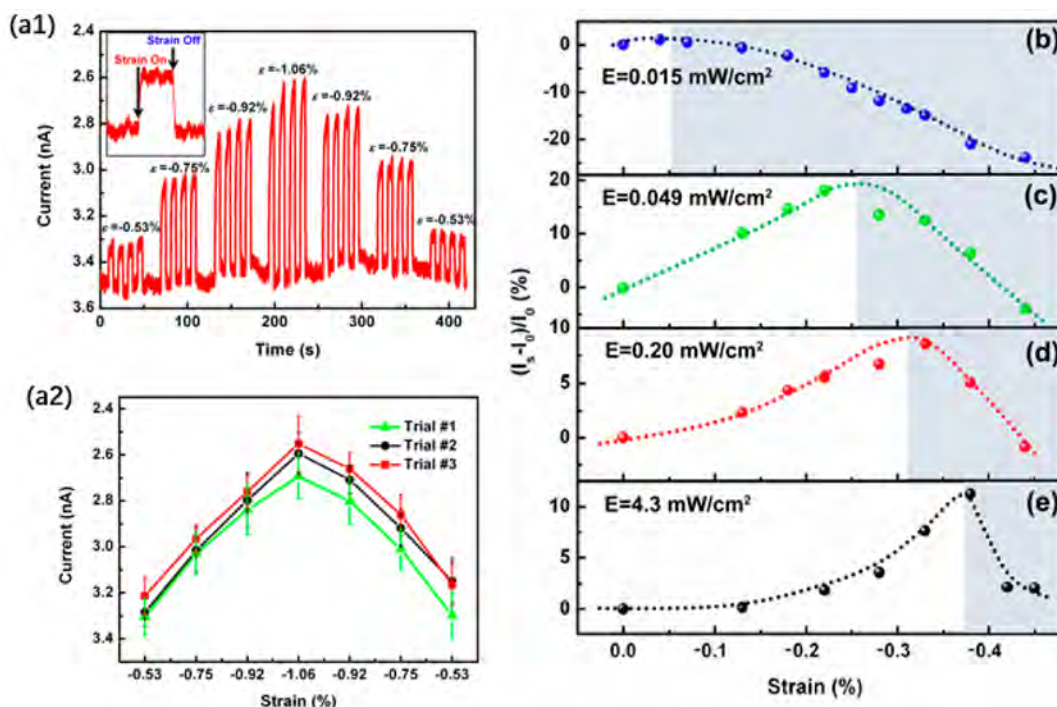


**Figure 42.** (a) Repeatability and stability test of a CdSe NW photodetector under a series of strains. (b–e) Relative current change of the photodetector when the CdSe NW photodetector is subjected to different light illuminations and different strains to determine the optimized working conditions. Reproduced with permission from ref 244. Copyright 2012 John Wiley and Sons.

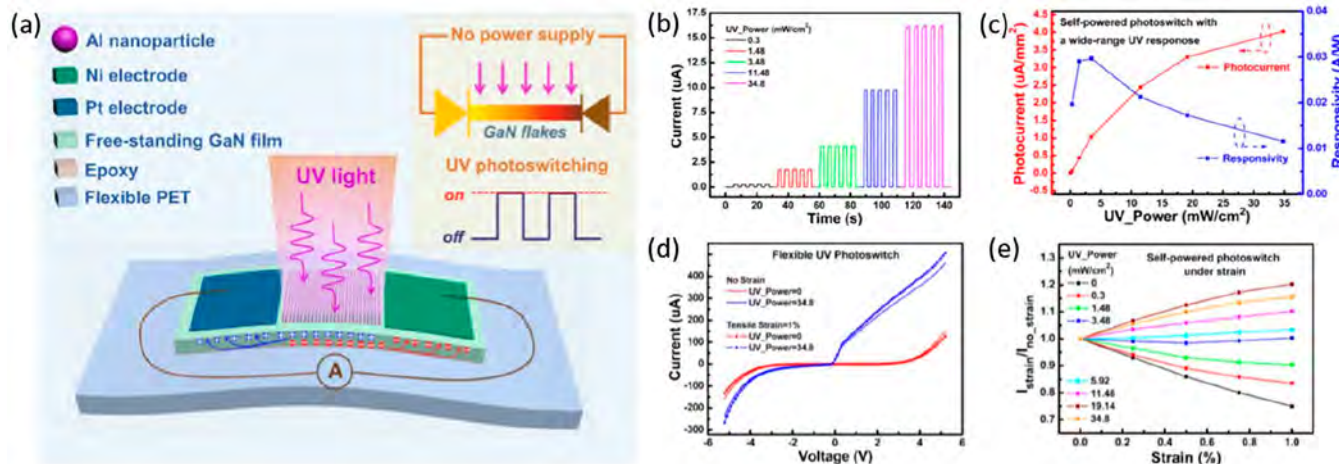


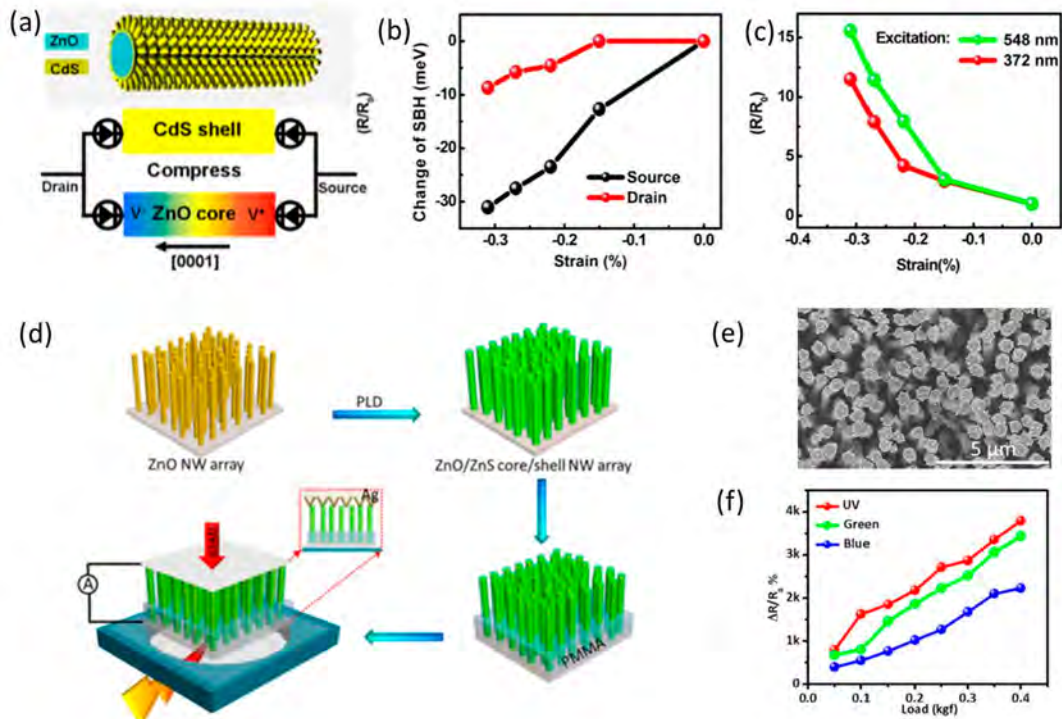
**Figure 43.** (a) Schematic of the structure of a GaN-based flexible M–S–M photo switch. (b) On/off switching, (c) photocurrent and responsivity with changing UV illumination. (d)  $I$ – $V$  characteristics as a function of external strain. (e) The current ratio with/without strain. Reproduced from ref 245. Copyright 2016 American Chemical Society.

the wire due to the introduction of a  $-0.36\%$  compressive strain in the NW. Following this work, several works on photodetectors with high-performance owing to the piezophototronic effect were performed.

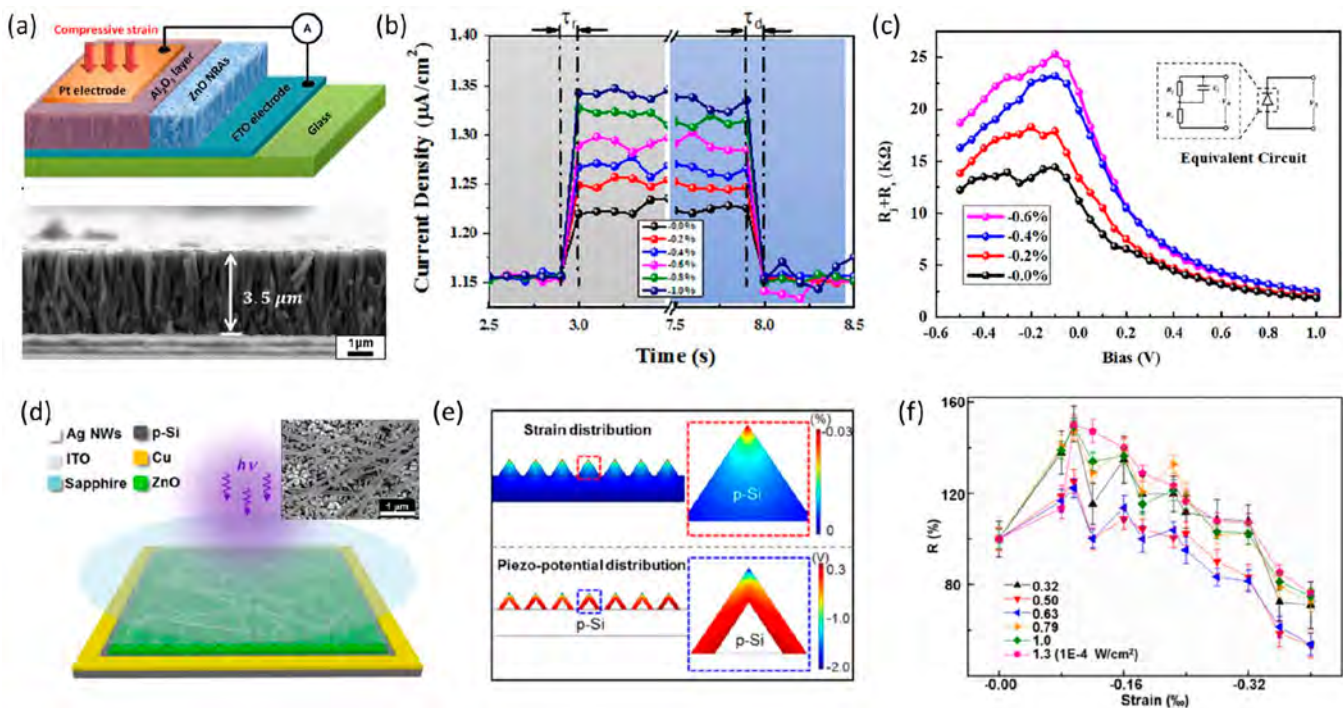
**5.2.1. Single NW Photodetector Based on the Piezophototronic Effect.** The CdSe NW photodetector responsivity can be improved through the piezophototronic effect as a result of modulating SBH by the piezoelectric potential at the interface of the photodetector. Dong, Pan, Wang, and co-workers reported a single NW photodetector based on a CdSe NW along with the theoretical model to show how the piezophototronic effect affects the device characteristics.<sup>244</sup> The performance of the CdSe NW photodetector is shown in

Figure 42a. This detector clearly has a very good sensitivity and a very good stability/repeatability. Figure 42b–d demonstrates that the piezophototronic effect can optimize the response of the detector. When the photodetector is under a compressive strain, the piezophototronic effect would increase the internal electric field of the SBH and accelerate the separation of the photoinduced electron–hole pairs, leading to the enhancement of photocurrent. Therefore, the flexible CdSe NW device sensitivity can be optimized through both the external strain and illumination intensity.

A self-powered UV M–S–M photo switch device based on GaN flexible film with high sensitivity and an ultrahigh on/off ratio was developed by Zhai, Wang, and co-workers (Figure



**Figure 44.** Two types of piezo-phototronic effect-enhanced core-shell hybrid photodetectors. (a–c) Illustration of the structure, the SBH changes, and the responsivity enhancement of a ZnO/CdS core/shell NW photodetector. Reproduced from ref 246. Copyright 2012 American Chemical Society. (d–f) The fabrication process, the device design, and the characteristic of a ZnO/ZnS core/shell NW array photodetector. Reproduced from ref 248. Copyright 2015 American Chemical Society.



**Figure 45.** Two types of piezo-phototronic effect-improved NW-based heterojunction photodetectors. (a–c) Illustration of the structure and design, current density in the response and recovery processes, and piezo-phototronic effect under different compressive strains of an MIS structure photodetector. Reproduced with permission from ref 249. Copyright 2014 Elsevier Ltd. (d–f) Illustration of the device design, simulation of the strain distribution, and photodetection enhancement of a p–n junction structure photodetector under various illumination and strain conditions. Reproduced from ref 252. Copyright 2010 American Chemical Society.

43).<sup>245</sup> With external pressure and deformation, the device can be driven by the force of UV photogenerated carriers via not

only the piezoelectric polarization field but also the built-in electric field arising from the two Schottky contacts with

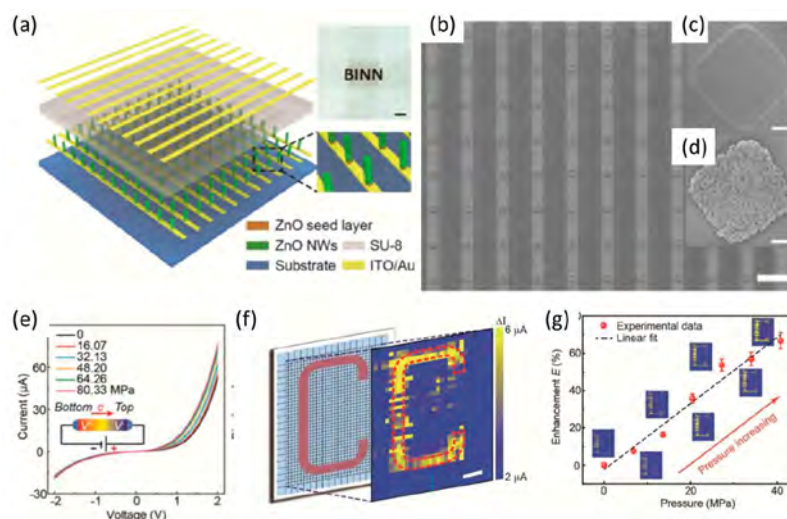


**Figure 46.** Piezo-phototronic effect in a NW photodetector array. (a–d) Schematic of the device design and SEM images of a ZnO NW-based UV photodetector array. The scale bar in (b) is 100  $\mu\text{m}$ , and the scale bars in (c and d) are 5  $\mu\text{m}$ . (e)  $I$ – $V$  curve of an individual ZnO NW photodetector pixel under different compressive strains. (f) Image of the distribution of UV illumination at a strain of 40.38 MPa. (g) Enhancement of the photodetection performance vs applied strain. Reproduced with permission from ref 253. Copyright 2015 John Wiley and Sons.

different metals. Since the GaN film is very thin, the device demonstrates excellent flexibility, thus generating a large piezoelectric field with the bending of the GaN membrane. The induced piezopotential can easily modulate the PV characteristics due to the piezo-phototronics effect. With an applied external strain (1%), the depletion region becomes stronger and broader, thus dramatically enhancing the UV on/off ratio. This work provides a new means to realize self-powered optoelectronic detection through local built-in electric fields.

**5.2.2. Core–Shell NW Photodetector Based on the Piezo-phototronic Effect.** A flexible visible/UV sensor fabricated on a ZnO–CdS core–shell NW with performance tuning by the piezo-phototronic effect was reported by Zhang, Wang, and co-workers.<sup>246,247</sup> Using a facile hydrothermal method, CdS NW arrays were fabricated on the surface of a ZnO NW, forming a ZnO–CdS core/shell nanostructure. Then, both ends of the core–shell NW were bonded onto a polymer substrate to fabricate the flexible photodetector. With the visible light sensitivity of the CdS NW and the UV sensitivity of the ZnO NW, this device is simultaneously sensitive to both UV light (372 nm) and green light (548 nm). When the device is under pressure, the strain-induced piezopotential will increase the ratio of the photocurrent to dark current by tuning the SBHs at the drain and source contacts.

Similar to this device structure, a flexible UV/visible photodetector based on a ZnO/ZnS core/shell NW was also successfully reported by Zhou and co-workers (Figure 44).<sup>248</sup> The characteristic of this photodetector can be improved through the piezo-phototronic effect since the piezoelectric potential will lower the barrier height, allowing easier charge carrier transport across the ZnO/ZnS interface, thus leading to a 3 orders of magnitude enhanced relative responsivity at excitation wavelengths of 385, 465, and 520 nm.

**5.2.3. Piezo-phototronic Effect in NW-Based Heterojunction Photodetectors.** In this section, we will discuss how to build an MIS junction- or a p–n junction-based photodetector and then how to realize the modulation of the detectivity by the piezo-phototronic effect. This type of device

is important for the applications of optoelectronics. In 2014, Yue Zhang and co-workers demonstrated a ZnO NW MIS junction-based self-powered photodetector, as can be seen in Figure 45a.<sup>249</sup> A ZnO NWs film was fabricated on a commercial glass/ITO substrate with a thickness of 3.5  $\mu\text{m}$ . Then, a thin layer of  $\text{Al}_2\text{O}_3$  was deposited onto the ZnO NW film, and a Pt electrode was formed on the top side. The performance of such an MIS self-powered photodetector is shown in Figure 45b. This self-powered device could work at power free condition and has very fast response and recovery times. The authors also demonstrated an enhancement achieved by the piezo-phototronic effect. Figure 45c shows when an external strain of  $-0.6\%$  was applied, the response of the photodetector device was greatly increased.<sup>250,251</sup>

We will now introduce a very important device, that is, Si p–n junction-based photodetector with state-of-the-art integrated circuit technique. An enhancement of the performance occurs due to the external strain generated piezoelectric charges at the interface from n-ZnO. The optoelectronic performance is modulated by optimizing the charge carriers which pass through the interface of the Si/ZnO heterojunction. The best photoresponsivity  $R$  was 7.1A/W when a 0.1% compressive external strain is applied to the ZnO NW layer, that is about 177% improvement in  $R$ . At the same time, the response time decreases to 87%.

**5.2.4. Piezo-phototronic Effect in NW Photodetector Arrays.** As a requirement for many practical applications, device arrays are essential. Based on the study of single NW piezo-phototronic effect-enhanced photodetector sensors, Pan, Wang, and co-workers designed a UV photodetector array based on  $32 \times 40$  pixels which are made up of ZnO NWs, as shown in Figure 46a.<sup>253</sup> Each NW bunch is a pixel of the UV photodetector array, constituted of Au nanopatterns and ZnO NWs (for the Schottky contact requirement). The as-fabricated photodetector is shown in Figure 46b–d. Similar to those of the single NW devices, the  $I$ – $V$  curves of each ZnO NW photodetector pixel are presented in Figure 46e, showing a very clear enhancement of the photocurrent under a compressive strain. When a planar light source with a shape of “C” and an excited light illumination of 1.38  $\text{mW}/\text{cm}^2$

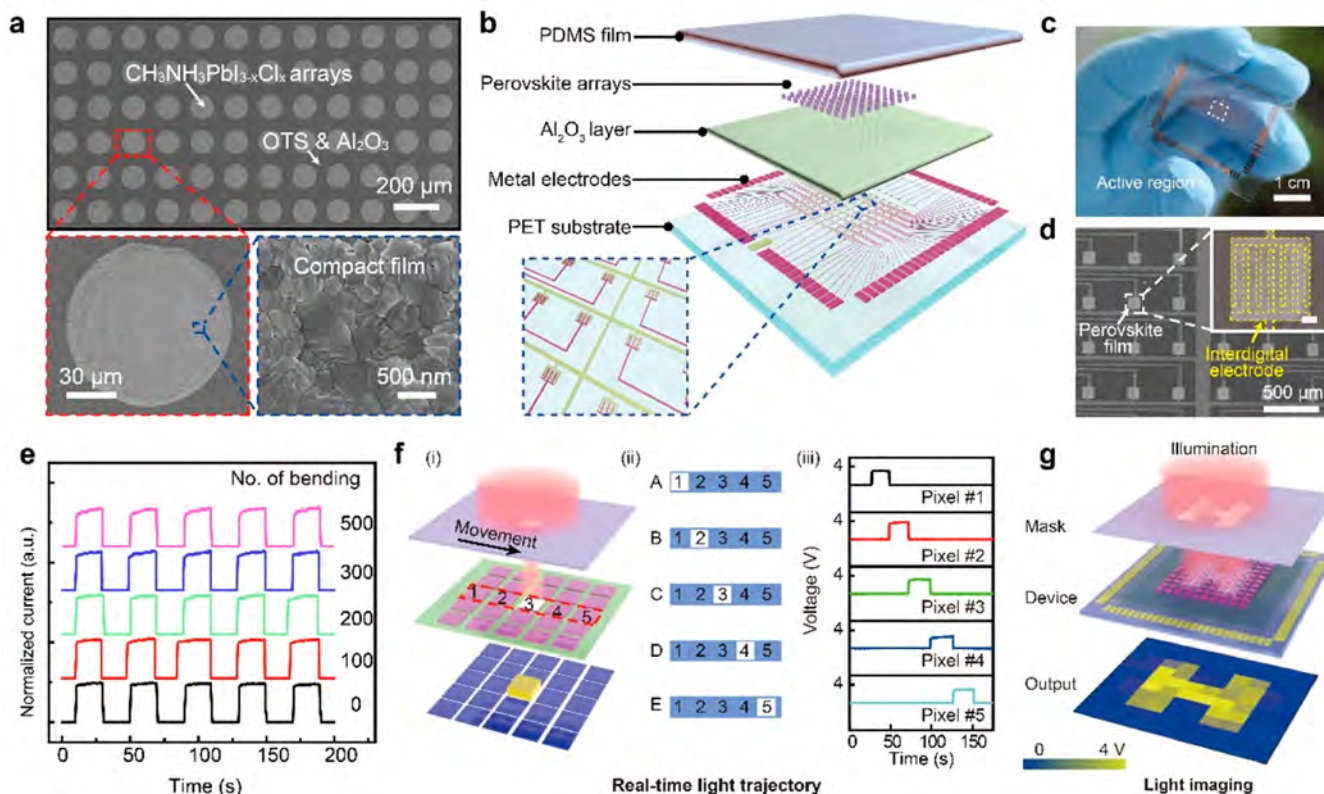


**Figure 47.** Flexible photodetector arrays. (a) SEM images of patterned  $\text{CH}_3\text{NH}_3\text{PbI}_{3-x}\text{Cl}_x$  perovskite arrays. (b–d) Device structure and photograph of the designed device, and corresponding SEM image of the active region. (e)  $I-t$  curves of an individual photodetector pixel after different bending cycles. (f) Demonstration of a real-time trajectory, including the light spot moving process and the change in the terminal voltage when the light spot illuminated the corresponding pixel. (g) Schematic illustration of the imaging capability of the photodetector arrays. Reproduced with permission from ref 254. Copyright 2018 John Wiley and Sons.

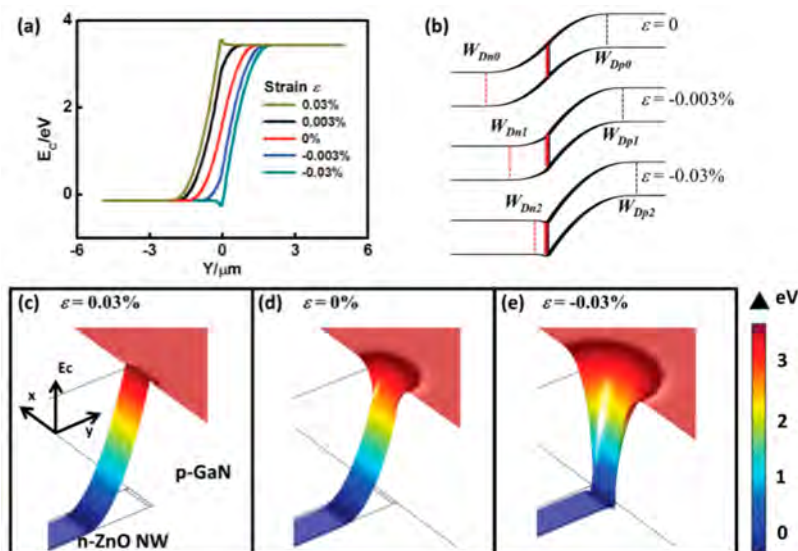


**Figure 48.** Simulation of heterogeneous p–n junctions. (a–b) Conduction band deformation and formation of the charge channel of the n-ZnO/p-ZnO heterostructure upon various external strains. (c–e) Conduction band simulation in the n-ZnO/p-ZnO heterostructure under different strains on the n-type side. Reproduced with permission from ref 262. Copyright 2014 John Wiley and Sons.

illuminated the device array, the distribution of the UV illumination was successfully imaged by the photodetector array (Figure 46f). By using the piezo-phototronic effect, the external strain generated piezoelectric charges dramatically improve the performance of the UV photodetector array by

600% for the sensitivity, 700% for the characteristic, and 280% for the detection range.

To develop deformable image sensors, novel flexible photodetector arrays must be exploited. To fabricate high-performance flexible photodetector arrays with large-scale

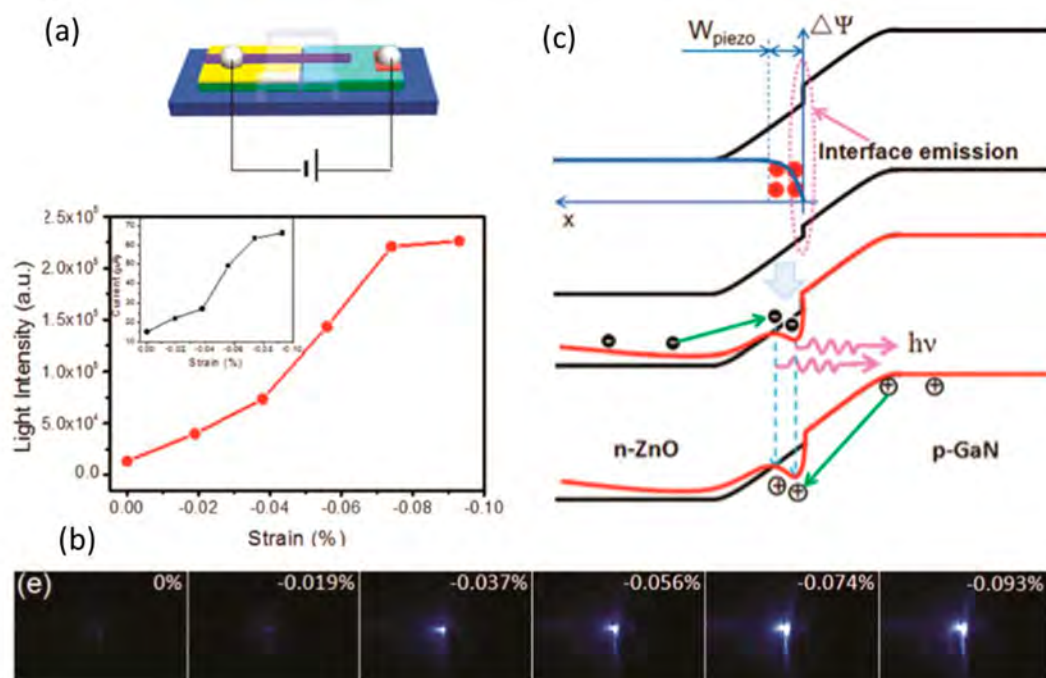


**Figure 49.** Piezo-phototronic effect in a single NW p–n junction LED. (a) Illustration of the single NW p–n junction LED. (b) Improvement of the light emission intensity of the single NW p–n junction LED under different strains. (c) Illustration of the energy band diagram of the p–n junction with (lower, red line) and without (upper) compressive strain. Reproduced from ref 45. Copyright 2011 American Chemical Society.

integration, Pan and co-workers first synthesized  $\text{CH}_3\text{NH}_3\text{PbI}_{3-x}\text{Cl}_x$  perovskite arrays with controllable morphology on a PET substrate using a two-step sequential deposition method along with a hydrophilic–hydrophobic surface treatment process, as shown in Figure 47a.<sup>254</sup> Based on the patterned perovskite material,  $10 \times 10$  pixelated flexible photodetector arrays were fabricated, as presented in the device design and the corresponding SEM image of the active region in Figure 47b–d. The  $I$ – $t$  curves of individual pixels in the flexible photodetector arrays after different bending cycles are displayed in Figure 47e, showing excellent bending endurance and flexibility. In addition, the photodetector arrays could capture the light trajectory in real time when the light spot was moved from pixel #1 to pixel #5 through tuning the mask in a straight line (Figure 47f). As shown in Figure 47g, by applying parallel white light through a designed mask to the active region of photodetector arrays, the light distribution can be identified from the obtained clear letter “H” observed in the mapping results, demonstrating good imaging performance.

### 5.3. Piezo-phototronic Effect in Light-Emitting Diodes

In our modern life, LEDs are required in many applications and have attracted a lot of research interest. Recently, many researchers have been working to enhance the luminescence efficiency of LEDs. In this section, we will introduce a series of works on improving the luminous efficiency and intensity of nano-LED devices through the piezo-phototronic effect of semiconductor NWs. These reports will provide new technology and potential approaches for the preparation of highly luminescent semiconductor nano-LED devices.<sup>255–261</sup>

**5.3.1. Theoretical Study of p–n Junction Piezo-phototronic Nano-LEDs.** The most typical device structure is the p–n junction NW LED. As shown in Figure 48a, the authors built a low-doped ZnO p–n homogeneous junction model using finite element analysis (FEA) and by solving the

Poisson equation.<sup>262</sup> The p–n junction LED light emission performance can be tuned through adjustment of the recombination, carrier injection, and light extraction efficiencies by the piezoelectric charges at the material interfaces of the LED device. When under a tensile strain, positive piezoelectric charges lead to the depletion zone shrinking on the n-type side and expanding on the p-type side. Conversely, under a compressive strain, the depletion zone on the p-type side shrinks and that on the n-type side expands. This process affects the carrier injection in the p–n junction and further results in changes in the electroluminescence intensity. Beyond nano-LEDs, the methodology reported by this article can also be expanded to other types of p–n junction photoelectronic devices. Such numerical modeling and theoretical calculations provide guidance for piezo-phototronic LED device design and optimization.

**5.3.2. Single NW LED Based on the Piezo-phototronic Effect.** By using the piezo-phototronic effect to tune the transport, separation, and recombination processes of carriers in the depletion area of a p–n junction, a NW p–n junction LED with performance enhancement under external mechanical stress/strain can be designed. Figure 49 shows that, a p–n junction single NW LED on a trench substrate was fabricated with a Mg-doped p-type GaN film and an n-type ZnO NW.<sup>45</sup> The ZnO NW was put over the gap and contact with the GaN substrate, and packaged by PS tape. If an external strain is applied to the LED, bending will occur at the gap of the GaN substrate, and the ZnO NW will undergo tensile deformation. Local bias voltage band modification is coming from the piezoelectric potential. These phenomena lead to enhancements of the light emission intensity and injection current under a fixed applied voltage. Under a compressive strain of 0.093%, the light intensity and device efficiency factors are increased to 4 and 17, respectively. This study demonstrated that the efficiency of a piezoelectric semiconductor-based LED

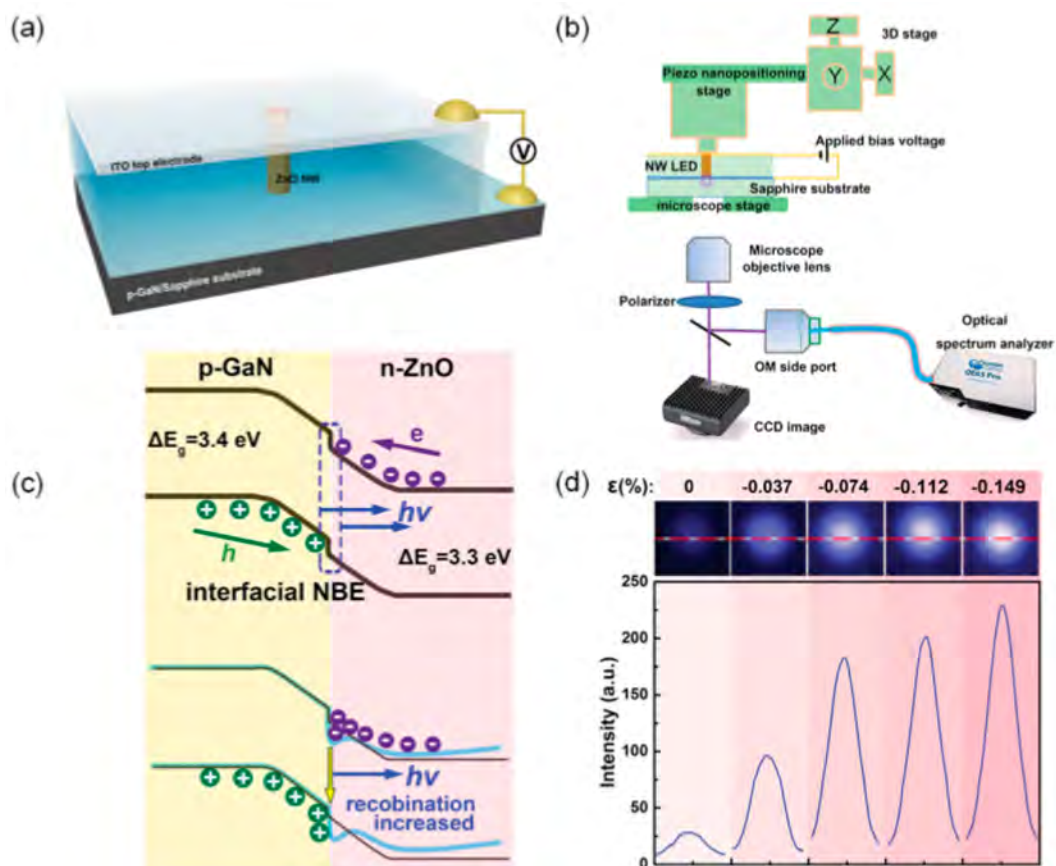


**Figure 50.** Schematic graph of vertical n-ZnO NW/p-GaN LED. (a) Schematic diagram of the vertically grown p-n junction single NW LED. (b) Testing process of the piezoelectric effect applied to the p-n junction LED. (c) Energy band structure of the p-n junction under compressive strain. (d) Images and light emission intensity of the single-wire LED under different applied strains. Reproduced with permission from ref 263. Copyright 2015 John Wiley and Sons.

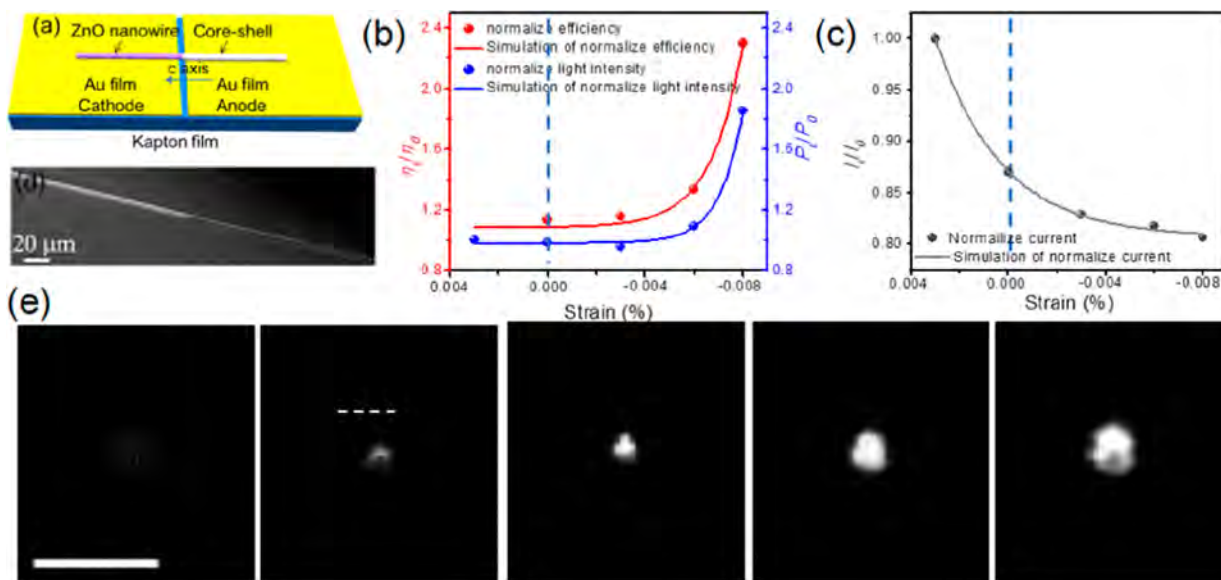


**Figure 51.** Piezo-phototronic effect enhancement of the light emission in a hybrid organic/inorganic single NW LED. (a) Illustration of the device, and (d) SEM image of the hybrid LED structure. (b) External efficiency and light intensity as a function of strains. (c) Relative injection current change under different strains. (e) CCD images of a packaged single NW LED under different applied strains, scale bar 10  $\mu\text{m}$ . Reproduced from ref 47. Copyright 2013 American Chemical Society.

can be effectively improved through the piezo-phototronic effect.

Similarly, when ZnO NWs were grown vertically on GaN substrates to form a p-n junction LED, the characteristic of

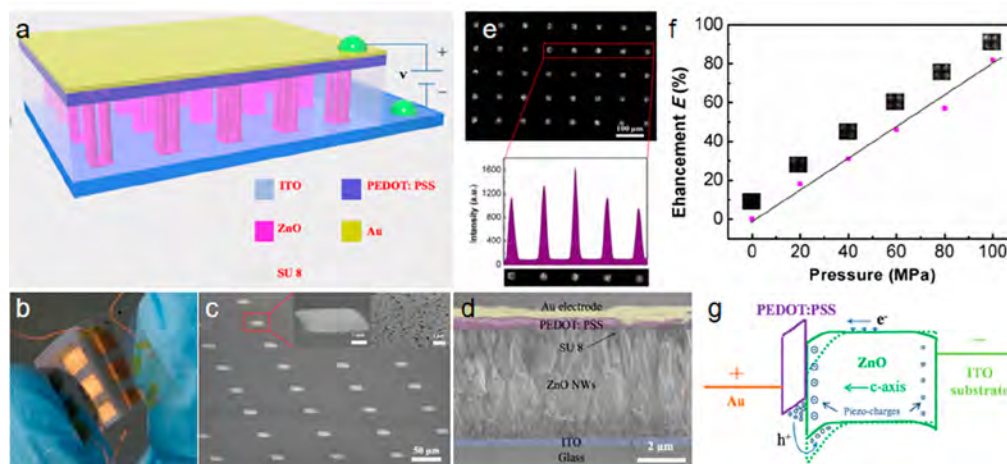


**Figure 52.** Flexible piezo-phototronic effect-enhanced hybrid NW array. (a) Schematic diagram and (b) photograph of this flexible hybrid device array. (c) SEM images and (d) cross-sectional SEM image of the hybrid device array (false color for better identification). (e) Optical image of the ZnO NW/p-polymer LED array when the device is electrically lit up. (f) Enhancement of the LED light emission under different pressures. (g) Schematic band diagram of this hybrid device before (dashed line) and after (solid line) applying a pressure. Reproduced with permission from ref 264. Copyright 2015 Elsevier Ltd.

the LED can also be controlled by the piezo-phototronics effect. Pan, Wang, and co-workers reported an LED device fabricated by growing a ZnO NW on a p-GaN thin film through a hydrothermal process. The space around the ZnO NW was filled by the insulator material of PMMA, with the NW tip exposed. The luminescence properties of devices under pressure were observed through the transparent top electrode (ITO) of the device on a piezo-nanopositioning stage (shown in Figure 50).<sup>263</sup> The light emission intensity was enhanced by 9 times when applying a compressive strain of  $-0.149\%$  along its *c*-axis. This process was contributed to trapping of holes from the p-type side and an increase in the recombination efficiency of carriers; more photons are produced in this process, and the light emission is therefore enhanced.

Furthermore, the piezo-phototronic effect can not only enhance an inorganic p–n junction LED but also dramatically improve that of a hybrid inorganic/organic LED by using ZnO NW/p-polymer heterostructure (Figure 51).<sup>47</sup> When the hybrid LED is under external pressure, the electron current can be tuned by the piezoelectric potential on the ZnO side to match the hole current near the interface of the p–n junction through the piezo-phototronic effect. The efficiency of this hybrid LED can be increased more than 2 times with an optimal strain was applied. The results of this article provide a new way to enhance the characteristic of organic devices and show its wide application in the fabrication of flexible optoelectronic devices.

**5.3.3. Piezo-phototronic Effect in LED Arrays.** Based on the study of piezo-phototronic effect-enhanced NW LEDs, flexible n-ZnO NW/p-polymer heterostructures were chosen to fabricate ordered NW array LEDs. Pan's group reported a piezo-phototronic effect-modulated n-ZnO NW/PEDOT:PSS LED array with ultrahigh light emission based on a flexible transparent ITO/PET substrate. The device structure and the fabrication progress were similar to those of the hard piezo-phototronic n-ZnO/p-GaN film device introduced in the last section. The electroluminescence of the device has a broad defect induced emission from 450 to 780 nm and a near band defect emission centered at 400 nm. To show how the piezo-

phototronic effect controls the light emission intensity of the hybrid LED array at a fixed forward bias, different pressures were applied to the upper-surface of the ZnO NW. The piezocharges produced by the compressive stress on the NW LED array reduce the barrier height for hole transportation and lead to an enhanced balance between the hole current and electron current. It can be seen from Figure 52 that the luminescence intensity of the LED linearly increases with the increasing of compressive stress.<sup>264</sup>

To eliminate deficiencies (poor emission efficiency and uncontrollable emission) in ZnO NWs based LEDs, a flexible ZnO/organic LED array was designed and fabricated which has both the piezoelectric effect of ZnO NWs and the advantages of organic LEDs (Figure 53).<sup>265,266</sup> The spatial

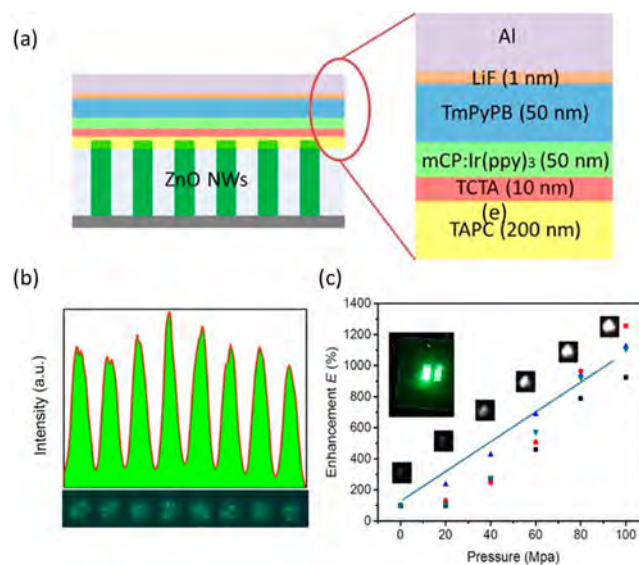


**Figure 53.** ZnO NW/organic LED piezo-phototronic effect-enhanced array. (a) Illustration of the device. (b) Light emission image of 8 adjacent pixels in the LED array. (c) The enhancement factor  $E$  as a function of external pressures. Reproduced from ref 265. Copyright 2017 American Chemical Society.

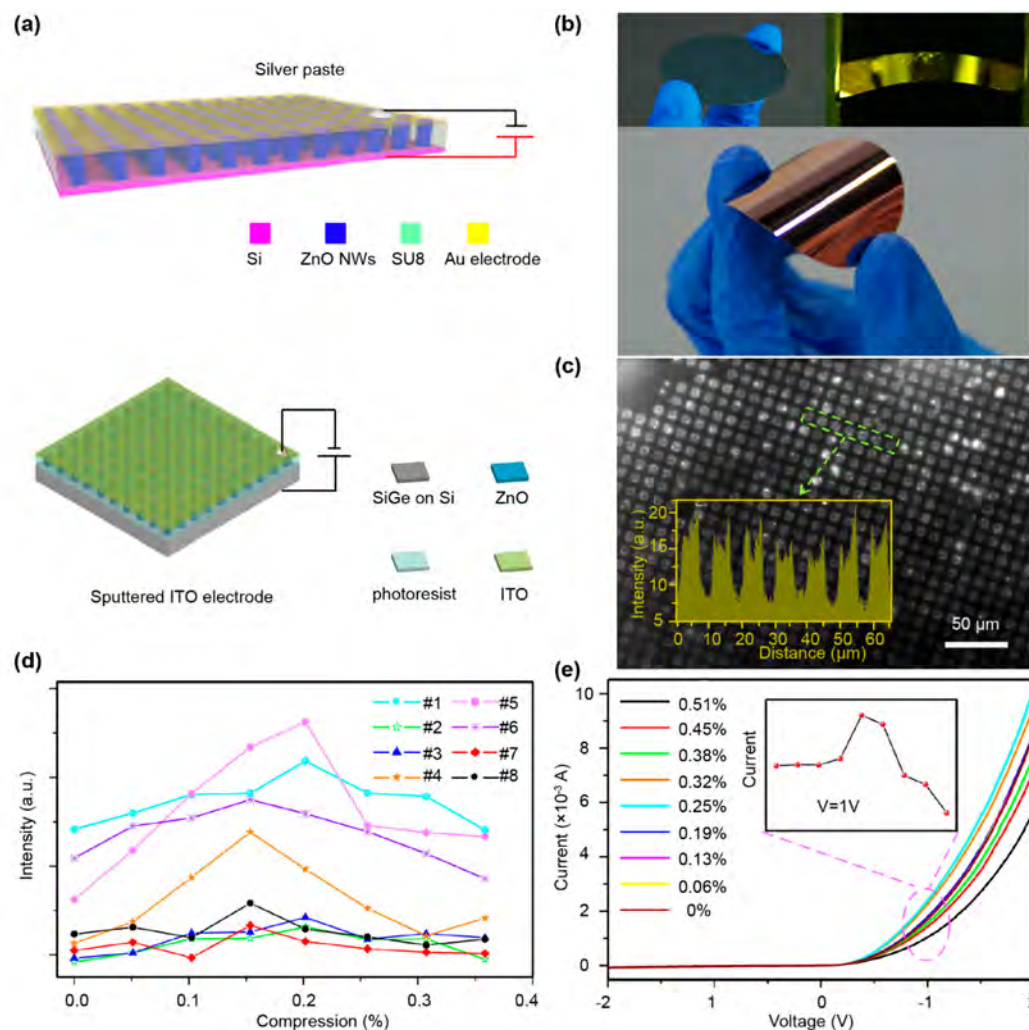


**Figure 54.** ZnO/Si LED nanodevice array: (a) Photograph of two-device. (b) The ZnO/Si LED on a soft Si wafer. (c) CCD images taken with a microscope of the device when lit up. (d) Changes in the light intensity of the ZnO/Si LED under increasing applied strain. (e)  $I$ - $V$  curve of the LED under various external strains, which show a similar regulated performance as the light emission shown in (d). (a) Reproduced with permission from ref 268. Copyright 2015 Springer Nature. (a-e) Reproduced from ref 267. Copyright 2016 American Chemical Society.

resolution of this NW based hybrid LED is determined by distance between two adjacent ZnO NWs while the light emission property is mainly coming from the organic LED part. The intensity of light emission can be tuned via the piezoelectric transistors of the ZnO NWs, which were connected in series with the organic LEDs to modify the energy band of the device.

ZnO/Si LED nanodevices tuned through the piezo-phototronic effect have been widely studied because Si is a traditional and the most important semiconductor material in the integrated circuit industry. A p-Si<sub>1-x</sub>Ge<sub>x</sub> alloy/n-ZnO p-n junction infrared light LED was built, and the light emission intensity affected by the piezo-phototronic effect has been studied (Figure 54).<sup>267,268</sup> The light emission wavelength of this device can be tuned via controlling the Ge composition in the Si<sub>1-x</sub>Ge<sub>x</sub> alloy. With the Ge composition increasing from 0.18 to 0.23 and 0.29, the average EL peak wavelength of the LED red shifts from 1144 to 1162 and 1185 nm. Then, a pressure-sensitive ZnO/Si NWs heterostructure LED array was fabricated. When the device is under compressive strain, the light emission of this Si-based LED first increases and then decreases with increasing strain. The maximum intensity was

achieved by applying an external strain of 0.2%. Such phenomenon, explained by the strain-induced piezoelectric charges, can modulate the energy band diagrams at the interface of the heterojunction thus tuning the photoelectric processing.

**5.3.4. Piezo-phototronic Effect in Visible Mechano-sensory Electronics.** The design of the next generation of tactile sensor matrix or electronic skins is important to human-machine interfaces and multifunctional robotics. The key requirements of these devices are high sensitivity, a fast response, and high spatial resolution. A classic design of electronic skins is using strain-sensitive capacitors or resistances arrays, which basically involve electrical signals. To read signals from this matrix, the electrical signal needs to be measured on each pixel one by one. It will cost a lot of time to record the pressure distribution when the matrix has too many sensor pixels. Thus, this design of tactile sensor matrix is not suitable for real time dynamic pressure/strain imaging. As reviewed in the previous sections, the light emission of piezoelectric semiconductor-based LEDs can be modulated by the piezo-phototronic effect. In other words, the light emission intensity is sensitive to externally applied strain. By this means,

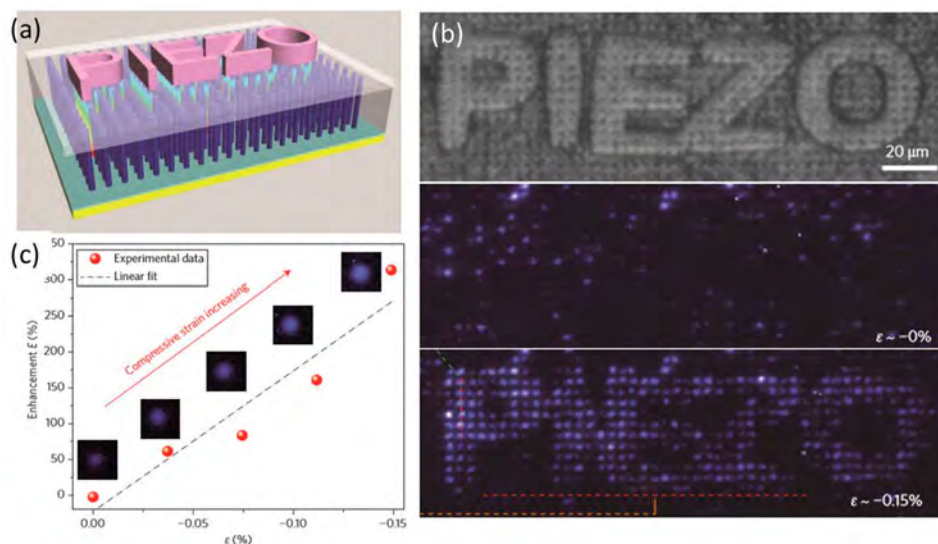


**Figure 55.** (a) Schematic graph of the working principle. (b) Photo of the sensor matrix, and the electroluminescence images of the sensor matrix without/with applied external pressure. (c) Enhancement factor as a function of the external compressive strain. Reproduced with permission from ref 269. Copyright 2013 Springer Nature.

a light-based pressure sensor was developed via a NW LED array. Additionally, the electroluminescence is suited for real time measurement and high-resolution pressure mapping simultaneously.

A visualized pressure mapping system with the structure of ordered ZnO NWs was reported, obtained by using low-temperature wet chemical methods and photolithographic patterning. The *c*-axis points away from the GaN thin film grown on a sapphire substrate. This pressure sensor array composed of n-ZnO NW/p-GaN was demonstrated to be able to map 2D pressure distributions with a pixel density of 6,350 dpi, or in other words, a spatial resolution of 2.7 mm. The gaps between the ZnO NWs were filled with PMMA as a buffer and an insulating material, with their tips exposed through oxygen plasma etching (Figure 55).<sup>269</sup> The bottom electrodes and top electrodes were fabricated separately by a Ni/Au layer and an ITO layer. The blue-white emission of the LED device was ascribed to the transition between shallow donor and deep acceptor levels in p-GaN, the recombination of electrons from holes from the p-type side and the n-type side at the interfaces and the near band edge (NBE) emission of ZnO NWs. If a compressive strain is applied to ZnO NWs, a negative piezopotential will be induced at the local heterostructure area of the ZnO/GaN p–n junction that increases the recombination speed of holes and electrons at the interface, resulting in an improvement of electroluminescent intensity. The pressure distribution can be read out by imaging the electroluminescent signals from all pixels in parallel. The time resolution is as low as 90 ms.

For use as a flexible electronic skin, a LED array composed of a flexible p-polymer layer and a n-ZnO NWs matrix was fabricated on a prepatterned PET substrate (Figure 56).<sup>147</sup> The spatial resolution for this device is 7  $\mu\text{m}$ . The ZnO NWs are used to transport electrons, and the PEDOT:PSS layer is used to transport holes. The hole injection barrier of the p–n junction of the device from the HOMO of the p-polymer to the valence band of ZnO is approximately 2.4 eV. The piezopotential induced by a compressive strain will decrease the barrier and increase the carrier recombination and emission intensity of the LED device. Moreover, the modulation of the

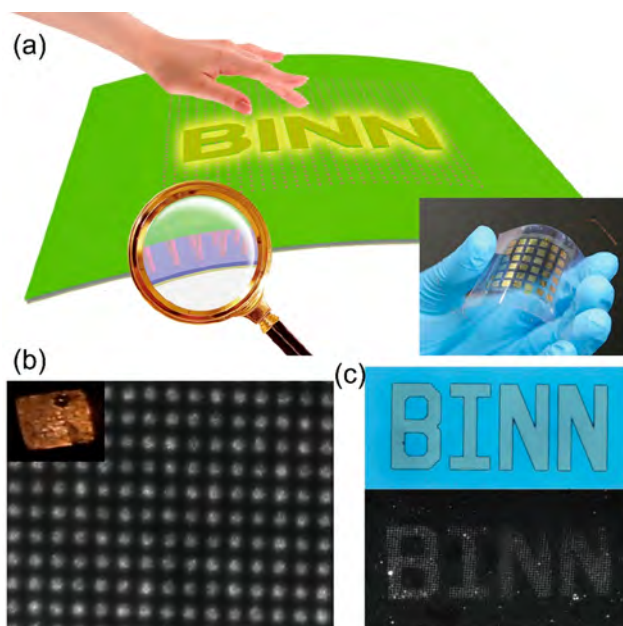


**Figure 56.** (a) Illustration of the device design and optical image of a flexible hybrid NW-LED-based pressure sensor. (b) Optical images of a flexible hybrid NW LED array device. (c) Optical image and electroluminescence images of the convex character pattern “BINN”. Reproduced with permission from ref 147. Copyright 2015 John Wiley and Sons.

growth conditions and the morphologies of the ZnO NW at each pixel on the range of pressures measured by the device were researched in this paper. A wide pressure measurement range (40–100 MPa) can be realized via tuning the growth conditions of the ZnO NWs.

Similar LED array pressure sensors have also been studied with other piezo-materials and device structures. Due to its nonlinear nature, piezoelectric effect, and potential for nano-LED applications, CdS has attracted a lot of attention in the last two decades. A p-polymer/n-CdS junction LED array and a Au-SiO<sub>2</sub>-CdS MIS LED were demonstrated by Pan's group

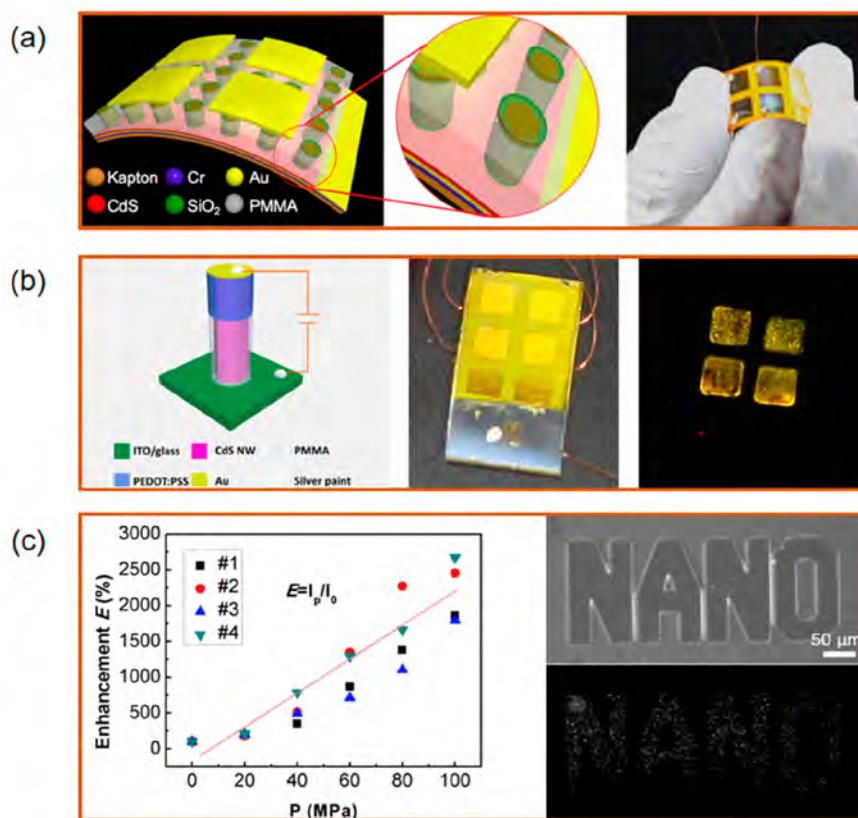


**Figure 57.** (a) Schematic and optical image of the Au-SiO<sub>2</sub>-CdS MIS LED device structure. (b) Schematic and optical image of the p-polymer/n-CdS junction LED array, and a photograph of when the device is lit up. (c) Enhancement factor  $E$  of several nanorod LEDs with applying compressive strains. The light-emitting image of the device at a strain of 100 MPa showing the stamp with the pattern “NANO” made by SU 8. Reproduced with permission from ref 266. Copyright 2016 Royal Society of Chemistry.

(Figure 57).<sup>266</sup> The intensity of light-emission is modulated by the recombination rate of electron–hole at the interface of Au/CdS. Such recombination processing could be controlled by the piezo-phototronic effect through the piezoelectric potential. This device array can map the pressure distribution a spatial resolution less than 2 μm.

Notably, the rigidity of the GaN/sapphire structures comes from the 500-μm-thick sapphire substrate, while the 5 μm GaN layer is flexible. Compared with GaN-based sensors, the flexible inorganic/organic hybridized pressure sensors exhibit some drawbacks, such as poorer stability. Therefore, we hope to separate the GaN film from the sapphire substrate and fabricate it into a flexible strain sensor with a ZnO NW array, thus realizing high-resolution pressure mapping through a soft GaN/ZnO LED array and potentially promoting the development of a prospective human-machine interface system. Aiming to combine the advantages of GaN-based and organic–inorganic pressure sensors, a flexible, high-resolution, fast-response, and stable pressure sensor with orderly and uniformly patterned *c*-axis direction ZnO NW arrays directly grown on a GaN film (after a laser lift-off process) through low-temperature hydrothermal methods was reported, which may potentially promote the development of a prospective human-machine interface system (Figure 58).<sup>270</sup> The pressure sensor array is composed of GaN/ZnO NW heterostructure LEDs, whose light-emission intensity can be improved by a local compressive strain based on the piezo-phototronic effect. A two-dimensional (2D) pressure distribution mapping is acquired by reading the illumination intensities from all LED

pixels in parallel, with a high spatial resolution of 2.6 μm. A compressive strain applied on the flexible LED array sensor tunes the energy band near the interface at the ZnO side, which enhances the recombination rate of holes and electrons in the p–n junction, resulting in an improvement of the emission intensity. Moreover, the flexible LED-based pressure sensors also possess a fast response time of 180 ms, good repeatability, and good stability and can still function well after 4000 bending circles or after being stored at normal temperature and atmosphere for over half a year.

Silicon, as the basic material of semiconductor devices, is widely used in the field of optoelectronic devices. The indirect bandgap structure of Si makes it difficult for photon generation and carrier recombination. Silicon-based LED arrays act as strain sensors that represent pressure distributions through the light emission intensities for electronic skin. Pan’s group reported an LED array obtained by ICP etching of a ZnO thin film and a Si wafer to produce ZSH for light emission at room temperature (Figure 59).<sup>271</sup> The EL spectrum of this device was measured and characterized in both the visible and near-infrared regions. The n-ZnO nanofilm/p-Si junction LED array exhibited white light emission, and the intensity was increased over 120% upon a compressive strain of 0.05%. This Si-based light-emitting device with high performance has potential applications in electronic skin and may be totally compatible with the dominate silicon microelectronic industry.

#### 5.4. Piezo-phototronic Effect in Electrochemical Processes

The photoelectron-chemical (PEC) water splitting process can be effectively enhanced through modulating the barrier height

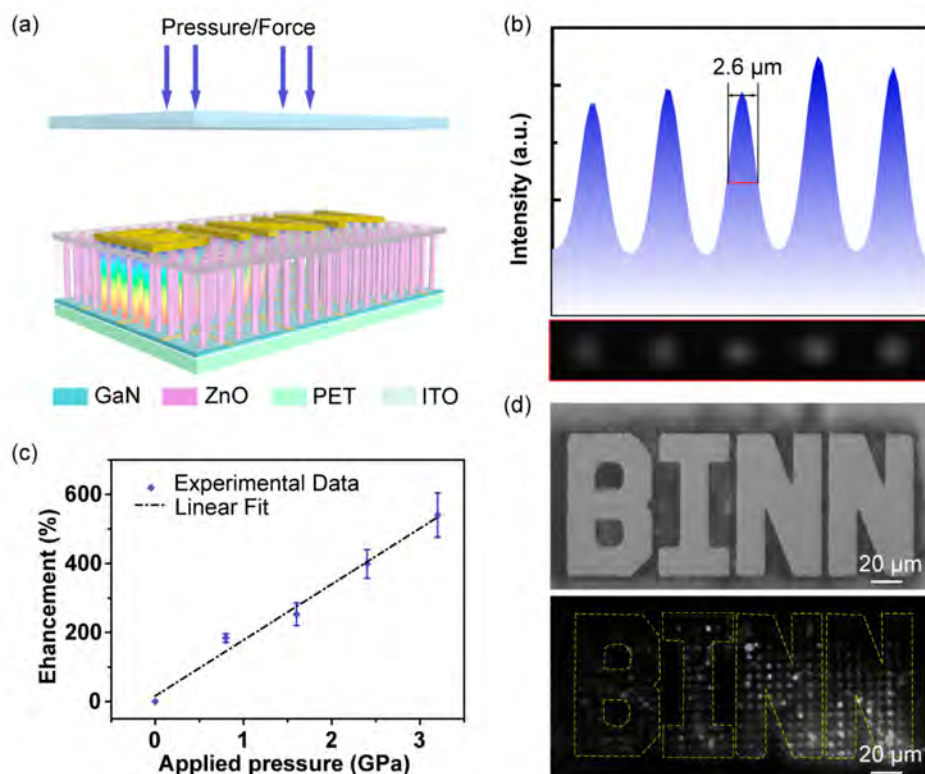


**Figure 58.** (a) Schematic illustration of pressure mapping performance of a flexible LED array. (b) Five typical lit NW LEDs and their related line profile of the light emission intensity. (c) Enhancement factor  $E$  as a function of applied pressure. (d) Photo of the convex character seal "BINN" and electroluminescence image at high pressure. Reproduced with permission from ref 270. Copyright 2019 Elsevier Ltd.

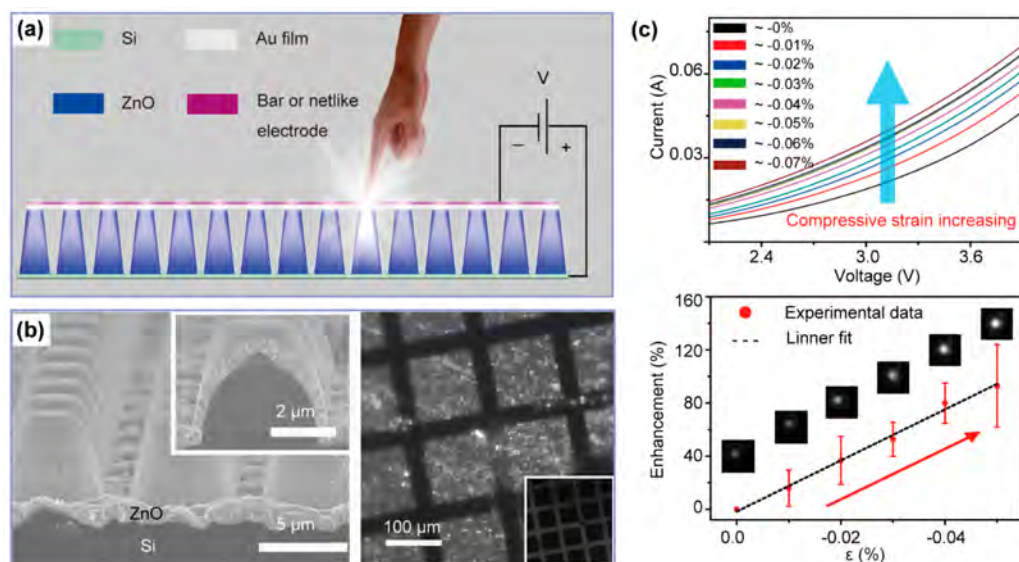


**Figure 59.** (a) Schematic of a Si-based LED array with the performance enhanced by the piezo-phototronic effect under strain. (b) Cross-sectional SEM images of ZnO-covered Si micropillars. Optical images of the as-fabricated device when lit up. (c)  $I$ - $V$  curve and enhancement of the light emission of the device (the insets are the corresponding images) under various applied strains. Reproduced with permission from ref 271. Copyright 2015 John Wiley and Sons.

of the semiconductor junction interface via a strain-induced piezo-polarization, so-called the piezo-phototronic effect (Figure 60).<sup>272,273</sup> A consistent reduction or enhancement in the photoinduced current can be realized through external compressive or tensile strain, respectively. Here, the variation in the photocurrent arises from the change in the barrier height at the ZnO/ITO junction area due to the remnant

piezopotential through the interface of the junction.<sup>274–282</sup>

In this system, a 0.1% applied external strain can induce an approximately 1.5 mV barrier height change, and a 0.21% external tensile strain generates a 10% enhancement of the PEC efficiency. Such a strain-modulated PEC process is similar to the piezo-phototronic-enhanced PV conversion.

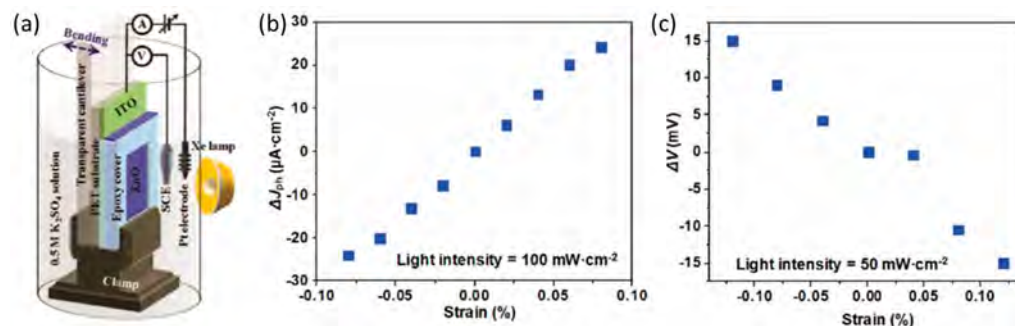


**Figure 60.** (a) Schematic of the piezotronic effect-enhanced photoelectrochemical measurement setup. Strain modulated (b) photocurrent density change and (c) applied bias change under light illumination. Reproduced from ref 272. Copyright 2011 American Chemical Society.

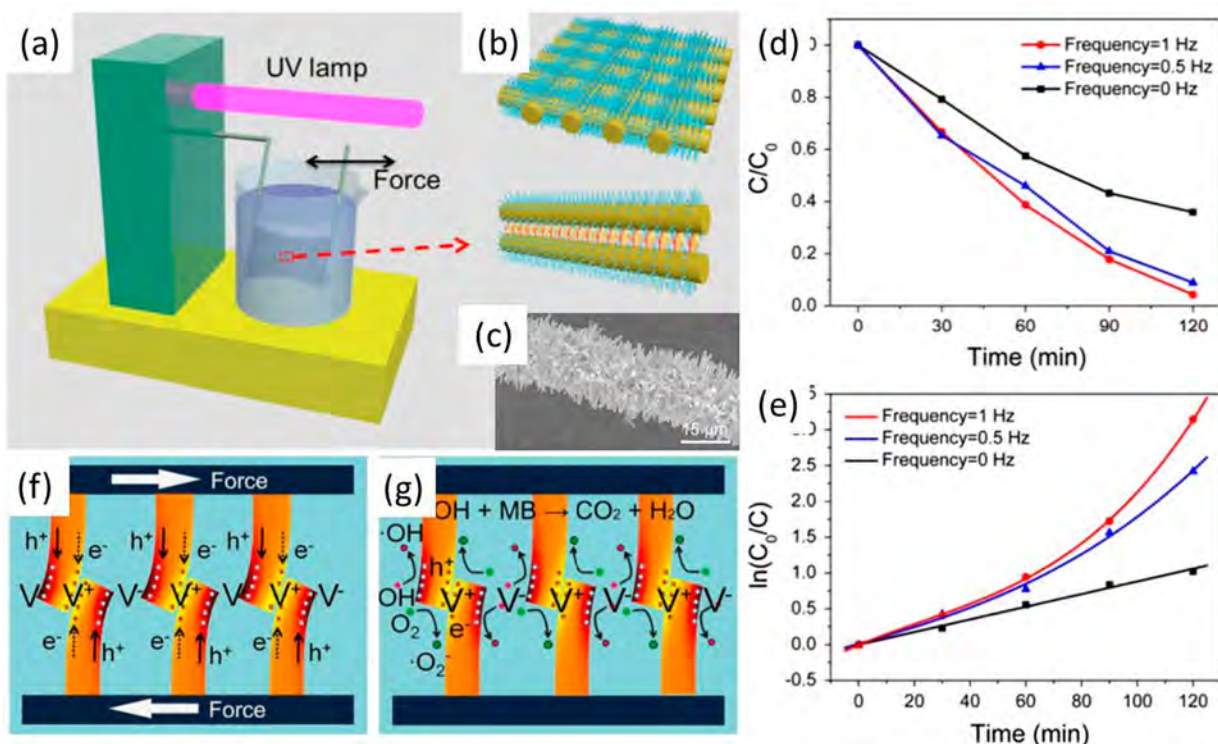


**Figure 61.** (a) Schematic graph of the experimental setup. (b) Fabrication processing and (c) SEM image of ZnO NWs on carbon fibers. (d, e) Photodegradation properties of ZnO NWs on carbon fibers. (f, g) Mechanism of piezoelectric effect-enhanced photocatalysis. Reproduced with permission from ref 283. Copyright 2015 Elsevier Ltd.

For wurtzite structure piezoelectric semiconductors, such as ZnO, the photoinduced holes and electrons can be separated by the driving force arising from the strain-generated piezoelectric field. Thus, the photocatalytic property of ZnO NWs for degrading organic pollution can be improved through the coupling of piezoelectric-generated separation and photoinduced carriers. With the combination of the photocatalytic and piezoelectric properties of ZnO NWs, a basic principle for piezoelectric effect-enhanced photocatalysis has been demonstrated.<sup>283</sup>

Compared to the pure piezoelectric semiconductor ZnO, hybrid semiconductors have better photocatalytic performance.<sup>284,285</sup> For example, when assembling TiO<sub>2</sub> nanodots on ZnO monocrystalline nanoplatelets, a piezoelectric potential can be induced in ZnO by applying a thermal stress to the piezoelectric ZnO nanoplatelets via cooling of the hybrid semiconductor from high temperature to room temperature at various cooling rates (Figure 62).<sup>143,286</sup> Because of the thermal

expansion mismatch between these two materials, the lattice parameter of ZnO will change, thus tuning the band structure of the heterojunction and effectively enhancing the photocatalytic rate by enhancing the charge separation. For the first time, this work utilized the piezoelectric polarization charges induced by a thermal stress to achieve effective photocatalysis regulation. This approach is a large step toward the application of the piezotronic effect and has great potential to enhance the photocatalytic performance on a large scale. This work offers a new method to apply an internal strain instead of an external strain to enhance the photocatalytic performance, which is very useful and can lead to energy savings.

## 6. CONCLUSION AND PERSPECTIVE

By utilizing wurtzite structure materials with both semiconductor and piezoelectric properties, such as ZnO, GaN, and CdS, the couplings between the piezoelectric, semiconductor, and photoexcitation properties have created a series of new

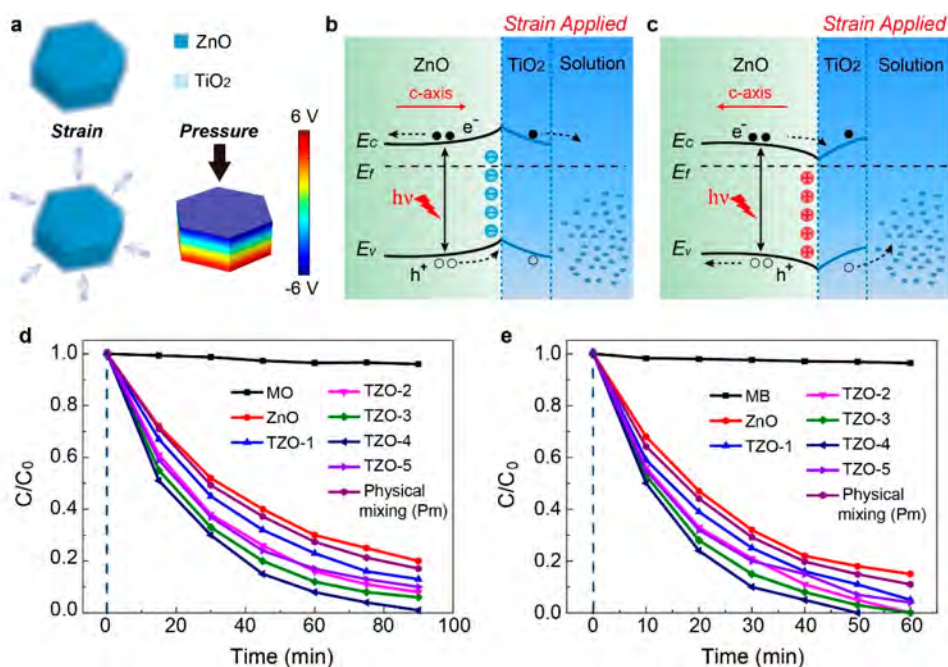


**Figure 62.** (a) Schematic and mechanism (b, c) of a ZnO/TiO<sub>2</sub> hybrid photocatalyst under an applied external strain. (d, e) Photocatalytic degradation as a function of the irradiation time for various photocatalysts. Reproduced from ref 286. Copyright 2016 American Chemical Society.

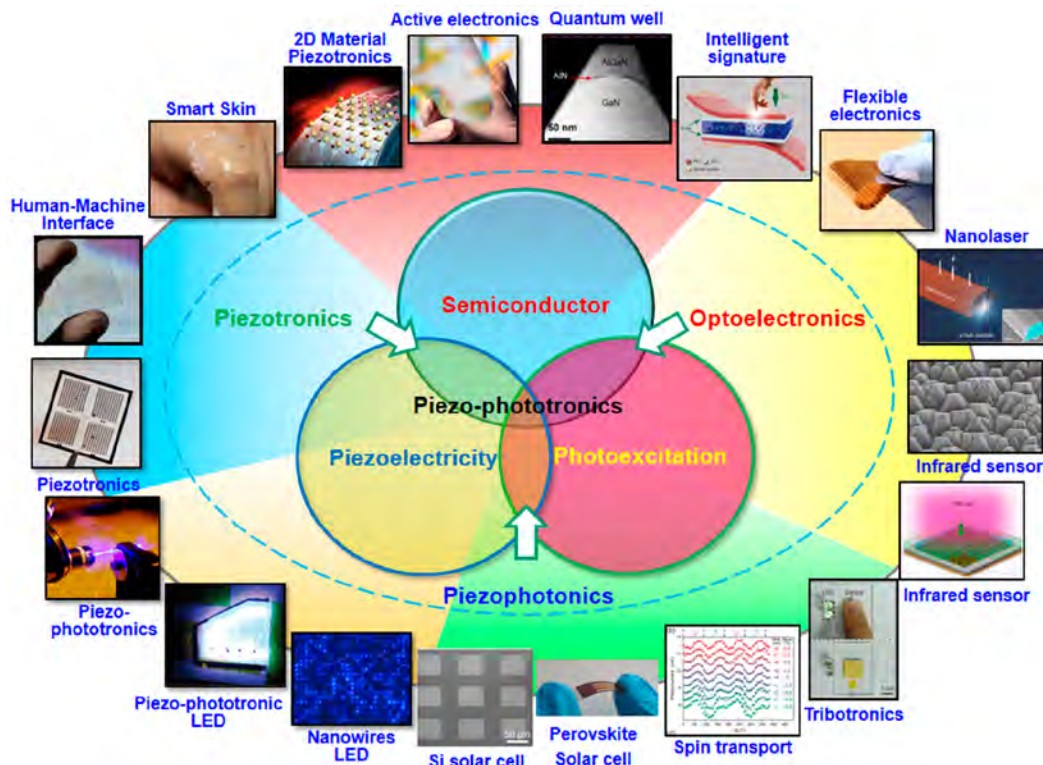


**Figure 63.** Potential applications of piezotronics, piezophotonics, and piezo-phototronics. *Middle:* Schematic graph showing the multiway couplings between piezoelectricity, semiconductivity, and photoexcitation. These couplings are the fundamental principles of piezotronics (coupling of piezoelectricity and semiconductivity), piezophotonics (coupling of piezoelectricity and photoexcitation), optoelectronics, and piezo-phototronics (coupling of piezoelectricity, semiconductivity, and photoexcitation). Reproduced with permission from ref 28. Copyright 2018 Materials Research Society.

research areas (Figure 63). The core of these studies and applications lies in the piezoelectric potential induced by the polarization of ions in the crystal when the piezoelectric material is stressed. Piezotronics is the discipline that uses the

piezoelectric potential as a gate voltage to regulate the transport of carriers in junction regions to study new electronic devices.<sup>135,287–291</sup> The piezo-phototronic effect involves the application of the piezoelectric potential to control the

generation, separation, transport, and recombination of carriers to improve the characteristics for optoelectronic applications such as solar cells, photodetectors, and LEDs. Piezotronics and piezo-phototronics are new and promising means to design new types of electronic and optoelectronic devices.<sup>292–297</sup>

Piezotronics will likely generate important applications in the areas of sensors, human-to-silicon-based interfaces, MEMS, logic devices, nanorobots, and active flexible electronics. Piezotronic devices can play an important role in the human-machine interface connected to silicon-based technology, similar to mechanical stimulation sensors in physiology. Mechanical excitation is the physiological basis for the conversion of electrical stimuli into the tactile, auditory, body balance perception, and pain sensations of neural signals.<sup>44,109,117,118,298–312</sup> Piezo-phototronics can be used to improve the efficiency of solar cells, the light intensity of LEDs, and the sensitivity of photodetectors; each area is important with a very large market. Moreover, the introduced piezoelectric potential provides a new method to improve the efficiency of photocatalysts. Although piezotronics and piezo-phototronics as effective methods to further improve electronic and photoelectric devices have drawn much attention, we expect the application of these effects to be further expanded through coupling with other research areas, such as sensor networks, life sciences, human-machine interface integration, and energy science (Figure 61).

During the last 12 years, much research has proven that piezoelectric charges induced by external strain/stress can effectively modify the barrier of a semiconductor-based interface and thus tune either the electronic or phototronic properties of semiconductor heterostructure devices. However, some fundamental questions regarding this type of modulation remain, such as the following:

- 1 What is the size limit of the interface and/or piezoelectric semiconductor at which piezoelectric charges can be generated and modify the properties of the interface? Will a quantum effect occur when the size of the semiconductor is less than 1 nm?
2. What is the response time of this external strain/stress-induced modulation?
3. In addition to the piezoelectric constant, do other factors affect the piezotronics and piezo-phototronics, such as the thickness of the depletion zone, defects at the interface and the contact potential of the heterostructure?
4. Is there an easy and effective means to apply external strain/stress to fabricated devices?
5. Can the piezotronic or piezo-phototronic processes (carrier generation, separation, and recombination tuned by piezoelectric charges) be directly observed in real time through in situ measurements?
6. Importantly, how can the performance of the devices improved by the piezotronic or piezo-phototronic effect be standardized, and how can a figure of merit be defined to evaluate the modulation of the piezotronics and piezo-phototronics in different applications?

Although most research on piezotronics and piezo-phototronics has been performed using 1D wurtzite materials, these effects can also be realized in 2D and bulk materials.<sup>46,115,131,313–317</sup> Inspired by the successful investigations of graphene, 2D semiconductor materials with unique electronic and optoelectronic properties have been widely

investigated. Among 2D semiconductor materials, transition metal dichalcogenides (TMDCs) demonstrate a large in-plane piezoelectricity due to the lack of charge concentration along their armchair direction, which offers a good material system for piezotronics and piezo-phototronics research on ultrathin materials for flexible applications. In addition, the semiconductor properties of 2D materials can easily be tuned by the surface states of the substrate due to the atomic-scale thickness. By using a piezoelectric substrate, the piezotronics and piezo-phototronics in 2D materials/piezoelectric substrates can be largely improved by optimizing the piezoelectric properties of the substrate and semiconductor properties of the 2D materials.<sup>298,318</sup>

## AUTHOR INFORMATION

### Corresponding Authors

\*E-mail: [cfpan@binn.cas.cn](mailto:cfpan@binn.cas.cn) .

\*E-mail: [jyzhai@binn.cas.cn](mailto:jyzhai@binn.cas.cn).

\*E-mail: [zlawng@binn.cas.cn](mailto:zlawng@binn.cas.cn) or [Zhong.wang@mse.gatech.edu](mailto:Zhong.wang@mse.gatech.edu).

### ORCID

Caofeng Pan: 0000-0001-6327-9692

Junyi Zhai: 0000-0001-8900-4638

Zhong Lin Wang: 0000-0002-5530-0380

### Notes

The authors declare no competing financial interest.

### Biographies

Caofeng Pan received his B.S. degree (2005) and his Ph.D. (2010) in Materials Science and Engineering from Tsinghua University, China. Then he joined the group of Professor Zhong Lin Wang at the Georgia Institute of Technology as a postdoctoral fellow. He is currently a full professor and a group leader at Beijing Institute of Nanoenergy and Nanosystems, Chinese Academy of Sciences since 2013. His research interests mainly focus on the fields of piezotronics/piezophototronics for fabricating new electronic and optoelectronic devices, nanopower source, hybrid nanogenerators, and self-powered nanosystems. He has authored over 140 journal papers and over 10 patents. Details can be found at <http://www.piezotronics.cn/>.

Junyi Zhai completed his Ph.D. degree in Materials Science and Engineering in 2009 from Virginia Tech. After postdoctoral training at Los Alamos National Laboratory, he was appointed as a professor in Beijing Institute of Nanoenergy and Nanosystems, Chinese Academy of Science at 2012, leading the group of Micro/Nano Piezoelectric Materials and Devices. His main research interests are fundamental and technological investigation of functional materials and multifields coupling for applications in electronics, sensors, and energy. He has authored over 90 journal articles and 10 patents.

Zhong Lin Wang received his Ph.D. from Arizona State University in physics. He now is the Hightower Chair in Materials Science and Engineering, Regents' Professor, Engineering Distinguished Professor and Director, Center for Nanostructure Characterization, at Georgia Tech. His research on self-powered nanosystems has inspired the worldwide effort in academia and industry for study in energy for micronano-systems, which is now a distinct disciplinary in energy research and future sensor networks. He coined and pioneered the field of piezotronics and piezo-phototronics by introducing piezoelectric potential gated charge transport process in fabricating new electronic and optoelectronic devices.

## ACKNOWLEDGMENTS

The authors acknowledge the support of national key R & D project from Minister of Science and Technology, China (2016YFA0202703 and 2016YFA0202704), National Natural Science Foundation of China (No. 51872031, 51622205, 61675027, 51432005, 61505010, 11704032, 5151101243, 51702017, 51561145021, and 51502018), Beijing City Committee of science and technology (Z171100000317001, Z171100002017019, and Z181100004418004), Natural Science Foundation of Beijing Municipality (4181004, 4182080, 4184110, 2184131, and Z180011), and the University of Chinese Academy of Sciences.

## REFERENCES

- (1) Jeon, Y. B.; Sood, R.; Jeong, J. h.; Kim, S. G. Mems Power Generator with Transverse Mode Thin Film PZT. *Sens. Actuators, A* **2005**, *122*, 16–22.
- (2) Shen, D.; Park, J. H.; Ajitsaria, J.; Choe, S. Y.; Wickle, H. C., Iii; Kim, D. J. The Design, Fabrication and Evaluation of a Mems Pzt Cantilever with an Integrated Si Proof Mass for Vibration Energy Harvesting. *J. Micromech. Microeng.* **2008**, *18*, No. 055017.
- (3) Yu, R. M.; Wang, X. F.; Peng, W. B.; Wu, W. Z.; Ding, Y.; Li, S. T.; Wang, Z. L. Piezotronic Effect in Strain-Gated Transistor of a-Axis Gan Nanobelt. *ACS Nano* **2015**, *9*, 9822–9829.
- (4) Yu, R. M.; Dong, L.; Pan, C. F.; Niu, S. M.; Liu, H. F.; Liu, W.; Chua, S.; Chi, D. Z.; Wang, Z. L. Piezotronic Effect on the Transport Properties of Gan Nanobelts for Active Flexible Electronics. *Adv. Mater.* **2012**, *24*, 3532–3537.
- (5) Wang, X. F.; Peng, W. B.; Pan, C. F.; Wang, Z. L. Piezotronics and Piezo-Phototronics Based on a-Axis Nano/Microwires: Fundamentals and Applications. *Semicond. Sci. Technol.* **2017**, *32*, No. 043005.
- (6) Wang, Z. L. Progress in Piezotronics and Piezo-Phototronics. *Adv. Mater.* **2012**, *24*, 4632–4646.
- (7) Wang, Z. L. Towards Self-Powered Nanosystems: From Nanogenerators to Nanopiezotronics. *Adv. Funct. Mater.* **2008**, *18*, 3553–3567.
- (8) Wang, Z. L. Zno Nanowire and Nanobelt Platform for Nanotechnology. *Mater. Sci. Eng., R* **2009**, *64*, 33–71.
- (9) Qin, Y.; Wang, X.; Wang, Z. L. Microfibre-Nanowire Hybrid Structure for Energy Scavenging. *Nature* **2008**, *451*, 809–813.
- (10) Wang, Z. L.; Song, J. Piezoelectric Nanogenerators Based on Zinc Oxide Nanowire Arrays. *Science* **2006**, *312*, 242–246.
- (11) Wang, X.; Song, J.; Liu, J.; Wang, Z. L. Direct-Current Nanogenerator Driven by Ultrasonic Waves. *Science* **2007**, *316*, 102.
- (12) Xu, S.; Qin, Y.; Xu, C.; Wei, Y.; Yang, R.; Wang, Z. L. Self-Powered Nanowire Devices. *Nat. Nanotechnol.* **2010**, *5*, 366–373.
- (13) Han, X.; Kou, L.; Lang, X.; Xia, J.; Wang, N.; Qin, R.; Lu, J.; Xu, J.; Liao, Z.; Zhang, X.; et al. Electronic and Mechanical Coupling in Bent Zno Nanowires. *Adv. Mater.* **2009**, *21*, 4937–4941.
- (14) Sun, C.; Shi, J.; Wang, X. Fundamental Study of Mechanical Energy Harvesting Using Piezoelectric Nanostructures. *J. Appl. Phys.* **2010**, *108*, No. 034309.
- (15) Gao, Y.; Wang, Z. L. Electrostatic Potential in a Bent Piezoelectric Nanowire. The Fundamental Theory of Nanogenerator and Nanopiezotronics. *Nano Lett.* **2007**, *7*, 2499–2505.
- (16) Xu, S.; Wei, Y.; Kirkham, M.; Liu, J.; Mai, W.; Davidovic, D.; Snyder, R. L.; Wang, Z. L. Patterned Growth of Vertically Aligned Zno Nanowire Arrays on Inorganic Substrates at Low Temperature without Catalyst. *J. Am. Chem. Soc.* **2008**, *130*, 14958.
- (17) Gao, Z.; Zhou, J.; Gu, Y.; Fei, P.; Hao, Y.; Bao, G.; Wang, Z. L. Effects of Piezoelectric Potential on the Transport Characteristics of Metal-Zno Nanowire-Metal Field Effect Transistor. *J. Appl. Phys.* **2009**, *105*, 113707.
- (18) Fan, Z.; Wang, D.; Chang, P.-C.; Tseng, W.-Y.; Lu, J. G. Zno Nanowire Field-Effect Transistor and Oxygen Sensing Property. *Appl. Phys. Lett.* **2004**, *85*, 5923–5925.
- (19) Goldberger, J.; Sirbully, D. J.; Law, M.; Yang, P. Zno Nanowire Transistors. *J. Phys. Chem. B* **2005**, *109*, 9.
- (20) Heo, Y. W.; Tien, L. C.; Kwon, Y.; Norton, D. P.; Pearton, S. J.; Kang, B. S.; Ren, F. Depletion-Mode Zno Nanowire Field-Effect Transistor. *Appl. Phys. Lett.* **2004**, *85*, 2274–2276.
- (21) He, J. H.; Hsin, C. L.; Liu, J.; Chen, L. J.; Wang, Z. L. Piezoelectric Gated Diode of a Single Zno Nanowire. *Adv. Mater.* **2007**, *19*, 781–784.
- (22) Wang, X.; Zhou, J.; Song, J.; Liu, J.; Xu, N.; Wang, Z. L. Piezoelectric Field Effect Transistor and Nanoforce Sensor Based on a Single Zno Nanowire. *Nano Lett.* **2006**, *6*, 2768–2772.
- (23) Zhou, J.; Fei, P.; Gu, Y.; Mai, W.; Gao, Y.; Yang, R.; Bao, G.; Wang, Z. L. Piezoelectric-Potential-Controlled Polarity-Reversible Schottky Diodes and Switches of Zno Wires. *Nano Lett.* **2008**, *8*, 3973.
- (24) Zhou, J.; Gu, Y.; Fei, P.; Mai, W.; Gao, Y.; Yang, R.; Bao, G.; Wang, Z. L. Flexible Piezotronic Strain Sensor. *Nano Lett.* **2008**, *8*, 3035–3040.
- (25) Wang, Z. L. Nanopiezotronics. *Adv. Mater.* **2007**, *19*, 889–892.
- (26) Wang, Z. L. The New Field of Nanopiezotronics. *Mater. Today* **2007**, *10*, 20–28.
- (27) Wang, Z. L. Piezopotential Gated Nanowire Devices: Piezotronics and Piezo-Phototronics. *Nano Today* **2010**, *5*, 540–552.
- (28) Wang, Z. L.; Wu, W.; Falconi, C. Piezotronics and Piezo-Phototronics with Third-Generation Semiconductors. *MRS Bull.* **2018**, *43*, 922–927.
- (29) Zhang, Y.; Leng, Y.; Willatzen, M.; Huang, B. Theory of Piezotronics and Piezo-Phototronics. *MRS Bull.* **2018**, *43*, 928–935.
- (30) Wen, X. N.; Wu, W. Z.; Pan, C. F.; Hu, Y. F.; Yang, Q.; Wang, Z. L. Development and Progress in Piezotronics. *Nano Energy* **2015**, *14*, 276–295.
- (31) Wang, X. D.; Zhang, H. L.; Yu, R. M.; Dong, L.; Peng, D. F.; Zhang, A. H.; Zhang, Y.; Liu, H.; Pan, C. F.; Wang, Z. L. Dynamic Pressure Mapping of Personalized Handwriting by a Flexible Sensor Matrix Based on the Mechanoluminescence Process. *Adv. Mater.* **2015**, *27*, 2324–2331.
- (32) Wong, M. C.; Chen, L.; Bai, G.; Huang, L. B.; Hao, J. Temporal and Remote Tuning of Piezophotonic-Effect-Induced Luminescence and Color Gamut Via Modulating Magnetic Field. *Adv. Mater.* **2017**, *29*, 1701945.
- (33) Wong, M. C.; Chen, L.; Tsang, M. K.; Zhang, Y.; Hao, J. H. Magnetic-Induced Luminescence from Flexible Composite Laminates by Coupling Magnetic Field to Piezophotonic Effect. *Adv. Mater.* **2015**, *27*, 4488–4495.
- (34) Hao, J.; Xu, C.-N. Piezophotonics: From Fundamentals and Materials to Applications. *MRS Bull.* **2018**, *43*, 965–969.
- (35) Zhang, Y.; Jie, W. J.; Chen, P.; Liu, W. W.; Hao, J. H. Ferroelectric and Piezoelectric Effects on the Optical Process in Advanced Materials and Devices. *Adv. Mater.* **2018**, *30*, 1707007.
- (36) Zhang, Y.; Gao, G. Y.; Chan, H. L. W.; Dai, J. Y.; Wang, Y.; Hao, J. H. Piezo-Phototronic Effect-Induced Dual-Mode Light and Ultrasound Emissions from Zns:Mn/Pmn-Pt Thin-Film Structures. *Adv. Mater.* **2012**, *24*, 1729–1735.
- (37) Zhang, H. L.; Peng, D. F.; Wang, W.; Dong, L.; Pan, C. F. Mechanically Induced Light Emission and Infrared-Laser-Induced Upconversion in the Er-Doped Caznos Multifunctional Piezoelectric Semiconductor for Optical Pressure and Temperature Sensing. *J. Phys. Chem. C* **2015**, *119*, 28136–28142.
- (38) Wong, M. C.; Chen, L.; Bai, G. X.; Huang, L. B.; Hao, J. H. Temporal and Remote Tuning of Piezophotonic-Effect-Induced Luminescence and Color Gamut Via Modulating Magnetic Field. *Adv. Mater.* **2017**, *29*, 1701945.
- (39) Wei, X. Y.; Wang, X. D.; Kuang, S. Y.; Su, L.; Li, H. Y.; Wang, Y.; Pan, C. F.; Wang, Z. L.; Zhu, G. Dynamic Triboelectrification-Induced Electroluminescence and Its Use in Visualized Sensing. *Adv. Mater.* **2016**, *28*, 6656.
- (40) Wang, X. D.; Que, M. L.; Chen, M. X.; Han, X.; Li, X. Y.; Pan, C. F.; Wang, Z. L. Full Dynamic-Range Pressure Sensor Matrix Based

on Optical and Electrical Dual-Mode Sensing. *Adv. Mater.* **2017**, *29*, 1605817.

(41) Wang, X. D.; Ling, R.; Zhang, Y. F.; Que, M. L.; Peng, Y. Y.; Pan, C. F. Oxygen-Assisted Preparation of Mechanoluminescent ZnS:Mn for Dynamic Pressure Mapping. *Nano Res.* **2018**, *11*, 1967–1976.

(42) Wang, W.; Peng, D. F.; Zhang, H. L.; Yang, X. H.; Pan, C. F. Mechanically Induced Strong Red Emission in Samarium Ions Doped Piezoelectric Semiconductor Caznos for Dynamic Pressure Sensing and Imaging. *Opt. Commun.* **2017**, *395*, 24–28.

(43) Fang, H. J.; Wang, X. D.; Li, Q.; Peng, D. F.; Yan, Q. F.; Pan, C. F. A Stretchable Nanogenerator with Electric/Light Dual-Mode Energy Conversion. *Adv. Energy Mater.* **2016**, *6*, 1600829.

(44) Pan, C. F.; Niu, S. M.; Ding, Y.; Dong, L.; Yu, R. M.; Liu, Y.; Zhu, G.; Wang, Z. L. Enhanced Cu<sub>2</sub>S/Cds Coaxial Nanowire Solar Cells by Piezo-Phototronic Effect. *Nano Lett.* **2012**, *12*, 3302–3307.

(45) Yang, Q.; Wang, W.; Xu, S.; Wang, Z. L. Enhancing Light Emission of ZnO Microwire-Based Diodes by Piezo-Phototronic Effect. *Nano Lett.* **2011**, *11*, 4012–4017.

(46) Wu, W. Z.; Wang, L.; Yu, R. M.; Liu, Y. Y.; Wei, S. H.; Hone, J.; Wang, Z. L. Piezophototronic Effect in Single-Atomic-Layer MoS<sub>2</sub> for Strain-Gated Flexible Optoelectronics. *Adv. Mater.* **2016**, *28*, 8463–8468.

(47) Yang, Q.; Liu, Y.; Pan, C.; Chen, J.; Wen, X.; Wang, Z. L. Largely Enhanced Efficiency in ZnO Nanowire/P-Polymer Hybridized Inorganic/Organic Ultraviolet Light-Emitting Diode by Piezo-Phototronic Effect. *Nano Lett.* **2013**, *13*, 607–613.

(48) Yang, Q.; Guo, X.; Wang, W. H.; Zhang, Y.; Xu, S.; Lien, D. H.; Wang, Z. L. Enhancing Sensitivity of a Single ZnO Micro-/Nanowire Photodetector by Piezo-Phototronic Effect. *ACS Nano* **2010**, *4*, 6285–6291.

(49) Hu, Y. F.; Pan, C. F.; Wang, Z. L. Recent Progress in Piezo-Phototronics with Extended Materials, Application Areas and Understanding. *Semicond. Sci. Technol.* **2017**, *32*, No. 053002.

(50) Liu, C.; Peng, M.; Yu, A.; Liu, J.; Song, M.; Zhang, Y.; Zhai, J. Interface Engineering on P-Cu/N-ZnO Heterojunction for Enhancing Piezoelectric and Piezo-Phototronic Performance. *Nano Energy* **2016**, *26*, 417–424.

(51) Wu, W. Z.; Wang, Z. L. Piezotronics and Piezo-Phototronics for Adaptive Electronics and Optoelectronics. *Nat. Rev. Mater.* **2016**, *1*, 16031.

(52) Bao, R.; Hu, Y.; Yang, Q.; Pan, C. Piezo-Phototronic Effect on Optoelectronic Nanodevices. *MRS Bull.* **2018**, *43*, 952–958.

(53) Kulkarni, A. J.; Zhou, M.; Sarasamak, K.; Limpijumnong, S. Novel Phase Transformation in ZnO Nanowires under Tensile Loading. *Phys. Rev. Lett.* **2006**, *97*, 105502.

(54) Agrawal, R.; Peng, B.; Espinosa, H. D. Experimental-Computational Investigation of ZnO Nanowires Strength and Fracture. *Nano Lett.* **2009**, *9*, 4177.

(55) Agrawal, R.; Espinosa, H. D. Giant Piezoelectric Size Effects in Zinc Oxide and Gallium Nitride Nanowires. A First Principles Investigation. *Nano Lett.* **2011**, *11*, 786–790.

(56) Zhao, M.; Zhonglin Wang, A.; S. X. M. Piezoelectric Characterization of Individual Zinc Oxide Nanobelt Probed by Piezoresponse Force Microscope. *Nano Lett.* **2004**, *4*, 587–590.

(57) Pan, Z. W.; Wang, Z. L. Nanobelts of Semiconducting Oxides. *Science* **2001**, *291*, 1947–1949.

(58) Wang, X.; Summers, C. J.; Wang, Z. L. Large-Scale Hexagonal-Patterned Growth of Aligned ZnO Nanorods for Nano-Optoelectronics and Nanosensor Arrays. *Nano Lett.* **2004**, *4*, 423.

(59) Zhang, Y.; Zhai, J. Y.; Wang, Z. L. Piezo-Phototronic Matrix Via a Nanowire Array. *Small* **2017**, *13*, 1702377.

(60) Yu, R. M.; Niu, S. M.; Pan, C. F.; Wang, Z. L. Piezotronic Effect Enhanced Performance of Schottky-Contacted Optical, Gas, Chemical and Biological Nanosensors. *Nano Energy* **2015**, *14*, 312–339.

(61) Wang, Z. L.; Wu, W. Z. Piezotronics and Piezo-Phototronics: Fundamentals and Applications. *Nat.l Sci. Rev.* **2014**, *1*, 62–90.

(62) Liu, Y.; Zhang, Y.; Yang, Q.; Niu, S. M.; Wang, Z. L. Fundamental Theories of Piezotronics and Piezo-Phototronics. *Nano Energy* **2015**, *14*, 257–275.

(63) Du, C. H.; Hu, W. G.; Wang, Z. L. Recent Progress on Piezotronic and Piezo-Phototronic Effects in Iii-Group Nitride Devices and Applications. *Adv. Eng. Mater.* **2018**, *20*, 1700760.

(64) Jana, N. R.; Gearheart, L.; Murphy, C. J. Wet Chemical Synthesis of High Aspect Ratio Cylindrical Gold Nanorods. *J. Phys. Chem. B* **2001**, *105*, 4065–4067.

(65) Caswell, K. K.; Bender, C. M.; Murphy, C. J. Seedless, Surfactantless Wet Chemical Synthesis of Silver Nanowires. *Nano Lett.* **2003**, *3*, 667–669.

(66) Jana, N. R.; Gearheart, L.; Murphy, C. J. Wet Chemical Synthesis of Silver Nanorods and Nanowires of Controllable Aspect Ratio. *Chem. Commun.* **2001**, *2001*, 617–618.

(67) Zheng, M. J.; Zhang, L. D.; Li, G. H.; Shen, W. Z. Fabrication and Optical Properties of Large-Scale Uniform Zinc Oxide Nanowire Arrays by One-Step Electrochemical Deposition Technique. *Chem. Phys. Lett.* **2002**, *363*, 123–128.

(68) Elias, J.; Tena-Zaera, R.; Lévy-Clément, C. Electrochemical Deposition of ZnO Nanowire Arrays with Tailored Dimensions. *J. Electroanal. Chem.* **2008**, *621*, 171–177.

(69) Elias, J.; Tena-Zaera, R.; Lévy-Clément, C. Electrodeposition of ZnO Nanowires with Controlled Dimensions for Photovoltaic Applications: Role of Buffer Layer. *Thin Solid Films* **2007**, *515*, 8553–8557.

(70) Tenazaera, R.; Elias, J.; Guillaume Wang, A.; Lévy-Clément, C. Role of Chloride Ions on Electrochemical Deposition of ZnO Nanowire Arrays from O<sub>2</sub> Reduction. *J. Phys. Chem. C* **2007**, *111*, 16706–16711.

(71) Yu, L.; Zhang, G.; Li, S.; Xi, Z.; Guo, D. Fabrication of Arrays of Zinc Oxide Nanorods and Nanotubes in Aqueous Solution under an External Voltage. *J. Cryst. Growth* **2007**, *299*, 184–188.

(72) Liu, B.; Zeng, H. C. Hydrothermal Synthesis of ZnO Nanorods in the Diameter Regime of 50 Nm. *J. Am. Chem. Soc.* **2003**, *125*, 4430.

(73) Xu, S.; Wang, Z. L. One-Dimensional ZnO Nanostructures: Solution Growth and Functional Properties. *Nano Res.* **2011**, *4*, 1013–1098.

(74) Vayssieres, L. Growth of Arrayed Nanorods and Nanowires of ZnO from Aqueous Solutions. *Adv. Mater.* **2010**, *15*, 464–466.

(75) Tak, Y.; Yong, K. Controlled Growth of Well-Aligned ZnO Nanorod Array Using a Novel Solution Method. *J. Phys. Chem. B* **2005**, *109*, 19263–19269.

(76) Greene, L. E.; Law, M.; Goldberger, J.; Kim, F.; Johnson, J. C.; Zhang, Y.; Saykally, R. J.; Yang, P. Low-Temperature Wafer-Scale Production of ZnO Nanowire Arrays. *Angew. Chem.* **2003**, *115*, 3139–3142.

(77) Wang, Z. L. Zinc Oxide Nanostructures: Growth, Properties and Applications. *J. Phys.: Condens. Matter* **2004**, *16*, R829–R858.

(78) Xu, S.; Lao, C.; Weintraub, B.; Wang, Z. L. Density-Controlled Growth of Aligned ZnO Nanowire Arrays by Seedless Chemical Approach on Smooth Surfaces. *J. Mater. Res.* **2008**, *23*, 2072–2077.

(79) Wei, Y.; Wu, W.; Guo, R.; Yuan, D.; Das, S.; Wang, Z. L. Wafer-Scale High-Throughput Ordered Growth of Vertically Aligned ZnO Nanowire Arrays. *Nano Lett.* **2010**, *10*, 3414–3419.

(80) Xiang, B.; Wang, P.; Zhang, X.; Dayeh, S. A.; Aplin, D. P. R.; Soci, C.; Yu, D.; Wang, D. Rational Synthesis of P-Type Zinc Oxide Nanowire Arrays Using Simple Chemical Vapor Deposition. *Nano Lett.* **2007**, *7*, 323.

(81) Wu, J. J.; Liu, S. C. Low-Temperature Growth of Well-Aligned ZnO Nanorods by Chemical Vapor Deposition. *Adv. Mater.* **2010**, *14*, 215–218.

(82) Bae, S. Y.; Seo, H. W.; Park, J. Vertically Aligned Sulfur-Doped ZnO Nanowires Synthesized Via Chemical Vapor Deposition. *J. Phys. Chem. B* **2004**, *35*, 5206–5210.

(83) Lyu, S. C.; Zhang, Y.; Ruh, H.; Lee, H. J.; Shim, H. W.; Suh, E. K.; Lee, C. J. Low Temperature Growth and Photoluminescence of Well-Aligned Zinc Oxide Nanowires. *Chem. Phys. Lett.* **2002**, *363*, 134–138.

- (84) Huang, M. H.; Mao, S.; Feick, H.; Yan, H.; Wu, Y.; Kind, H.; Weber, E.; Russo, R.; Yang, P. Room-Temperature Ultraviolet Nanowire Nanolasers. *Science* **2001**, *32*, 1897–1899.
- (85) Wang, X.; Song, J.; Li, P.; Ryou, J. H.; Dupuis, R. D.; Summers, C. J.; Wang, Z. L. Growth of Uniformly Aligned ZnO Nanowire Heterojunction Arrays on GaN, AlN, and Al<sub>0.5</sub>Ga<sub>0.5</sub>Sn Substrates. *J. Am. Chem. Soc.* **2005**, *127*, 7920–7923.
- (86) Kaidashev, E. M.; Lorenz, M.; von Wenckstern, H.; Rahm, A.; Semmelhack, H. C.; Han, K. H.; Benndorf, G.; Bundesmann, C.; Hochmuth, H.; Grundmann, M. High Electron Mobility of Epitaxial ZnO Thin Films on C-Plane Sapphire Grown by Multistep Pulsed-Laser Deposition. *Appl. Phys. Lett.* **2003**, *82*, 3901–3903.
- (87) Lorenz, M.; Kaidashev, E. M.; Rahm, A.; Nobis, T.; Lenzner, J.; Wagner, G.; Spemann, D.; Hochmuth, H.; Grundmann, M. Mg<sub>x</sub>Zn<sub>1-x</sub>O (0 < x < 0.2) Nanowire Arrays on Sapphire Grown by High-Pressure Pulsed-Laser Deposition. *Appl. Phys. Lett.* **2005**, *86*, 143113.
- (88) Cao, B. Q.; Lorenz, M.; Rahm, A.; von Wenckstern, H.; Czekalla, C.; Lenzner, J.; Benndorf, G.; Grundmann, M. Phosphorus Acceptor Doped ZnO Nanowires Prepared by Pulsed-Laser Deposition. *Nanotechnology* **2007**, *18*, 455707.
- (89) Tien, L. C.; Pearn, S. J.; Norton, D. P.; Ren, F. Synthesis and Microstructure of Vertically Aligned ZnO Nanowires Grown by High-Pressure-Assisted Pulsed-Laser Deposition. *J. Mater. Sci.* **2008**, *43*, 6925–6932.
- (90) Okada, T.; Agung, B. H.; Nakata, Y. ZnO Nano-Rods Synthesized by Nano-Particle-Assisted Pulsed-Laser Deposition. *Appl. Phys. A: Mater. Sci. Process.* **2004**, *79*, 1417–1419.
- (91) Lin, S. S.; Hong, J. I.; Song, J. H.; Zhu, Y.; He, H. P.; Xu, Z.; Wei, Y. G.; Ding, Y.; Snyder, R. L.; Wang, Z. L. Phosphorus Doped Zn(1-x)Mg(x)O Nanowire Arrays. *Nano Lett.* **2009**, *9*, 3877.
- (92) Park, I.; Li, Z.; Pisano, A. P.; Williams, R. S. Top-Down Fabricated Silicon Nanowire Sensors for Real-Time Chemical Detection. *Nanotechnology* **2010**, *21*, No. 015501.
- (93) Elibol, O. H.; Morissette, D.; Akin, D.; Denton, J. P.; Bashir, R. Integrated Nanoscale Silicon Sensors Using Top-Down Fabrication. *Appl. Phys. Lett.* **2003**, *83*, 4613–4615.
- (94) Hobbs, R. G.; Petkov, N.; Holmes, J. D. Semiconductor Nanowire Fabrication by Bottom-up and Top-Down Paradigms. *Chem. Mater.* **2012**, *24*, 1975–1991.
- (95) Koleske, D. D.; Wang, G. T.; Figiel, J. J.; Cross, K. C.; Westlake, K. R.; Crawford, M. H.; Li, Q.; Fatholouloumi, S.; Lee, S. R.; Mi, Z. Optical Performance of Top-Down Fabricated InGaN/GaN Nanorod Light Emitting Diode Arrays. *Opt. Express* **2011**, *19*, 25528.
- (96) Peng, M. Z.; Li, Z.; Liu, C. H.; Zheng, Q.; Shi, X. Q.; Song, M.; Zhang, Y.; Du, S. Y.; Zhai, J. Y.; Wang, Z. L. High-Resolution Dynamic Pressure Sensor Array Based on Piezo-Phototronic Effect Tuned Photoluminescence Imaging. *ACS Nano* **2015**, *9*, 3143–3150.
- (97) Zhang, Y.; Liu, Y.; Wang, Z. L. Fundamental Theory of Piezotronics. *Adv. Mater.* **2011**, *23*, 3004–3013.
- (98) Kanda, Y. Piezoresistance Effect of Silicon. *Sens. Actuators, A* **1991**, *28*, 83–91.
- (99) Wei, B.; Zheng, K.; Ji, Y.; Zhang, Y.; Zhang, Z.; Han, X. Size-Dependent Bandgap Modulation of ZnO Nanowires by Tensile Strain. *Nano Lett.* **2012**, *12*, 4595–4599.
- (100) Bykhovski, A. D.; Kaminski, V. V.; Shur, M. S.; Chen, Q. C.; Khan, M. A. Piezoresistive Effect in Wurtzite N-Type GaN. *Appl. Phys. Lett.* **1996**, *68*, 818–819.
- (101) Qi, J.; Lan, Y. W.; Stieg, A. Z.; Chen, J. H.; Zhong, Y. L.; Li, L. J.; Chen, C. D.; Zhang, Y.; Wang, K. L. Piezoelectric Effect in Chemical Vapour Deposition-Grown Atomic-Monolayer Triangular Molybdenum Disulfide Piezotronics. *Nat. Commun.* **2015**, *6*, 7430.
- (102) Wu, W. Z.; Wang, L.; Li, Y. L.; Zhang, F.; Lin, L.; Niu, S. M.; Chenet, D.; Zhang, X.; Hao, Y. F.; Heinz, T. F.; et al. Piezoelectricity of Single-Atomic-Layer Mos<sub>2</sub> for Energy Conversion and Piezotronics. *Nature* **2014**, *514*, 470–474.
- (103) Xue, F.; Zhang, J.; Hu, W.; Hsu, W. T.; Han, A.; Leung, S. F.; Huang, J. K.; Wan, Y.; Liu, S.; Zhang, J.; et al. Multidirection Piezoelectricity in Mono- and Multilayered Hexagonal Alpha-In<sub>2</sub>Se<sub>3</sub>. *ACS Nano* **2018**, *12*, 4976–4983.
- (104) Schottky, W. Halbleitertheorie Der Sperrschicht. *Naturwissenschaften* **1938**, *26*, 843–843.
- (105) Ikeda, T. *Fundamentals of Piezoelectricity*; Oxford University Press, 1990.
- (106) Guo, J. M.; Wen, R. M.; Liu, Y. D.; Zhang, K.; Kou, J. Z.; Zhai, J. Y.; Wang, Z. L. Piezotronic Effect Enhanced Flexible Humidity Sensing of Monolayer Mos<sub>2</sub>. *ACS Appl. Mater. Interfaces* **2018**, *10*, 8110–8116.
- (107) Zhou, R. R.; Hu, G. F.; Yu, R. M.; Pan, C. F.; Wang, Z. L. Piezotronic Effect Enhanced Detection of Flammable/Toxic Gases by ZnO Micro/Nanowire Sensors. *Nano Energy* **2015**, *12*, 588–596.
- (108) Hu, G. F.; Zhou, R. R.; Yu, R. M.; Dong, L.; Pan, C. F.; Wang, Z. L. Piezotronic Effect Enhanced Schottky-Contact ZnO Micro/Nanowire Humidity Sensors. *Nano Res.* **2014**, *7*, 1083–1091.
- (109) Wang, L. F.; Liu, S. H.; Gao, G. Y.; Pang, Y. K.; Yin, X.; Feng, X. L.; Zhu, L. P.; Bai, Y.; Chen, L. B.; Xiao, T. X.; et al. Ultrathin Piezotronic Transistors with 2 Nm Channel Lengths. *ACS Nano* **2018**, *12*, 4903–4908.
- (110) Zhang, Y.; Wang, Z. L. Theory of Piezo-Phototronics for Light-Emitting Diodes. *Adv. Mater.* **2012**, *24*, 4712–4718.
- (111) Liu, W.; Zhang, A. H.; Zhang, Y.; Wang, Z. L. Density Functional Studies on Wurtzite Piezotronic Transistors: Influence of Different Semiconductors and Metals on Piezoelectric Charge Distribution and Schottky Barrier. *Nanotechnology* **2016**, *27*, 205204.
- (112) Liu, W.; Zhang, A. H.; Zhang, Y.; Wang, Z. L. First Principle Simulations of Piezotronic Transistors. *Nano Energy* **2015**, *14*, 355–363.
- (113) Peng, M.; Zhang, Y.; Liu, Y.; Song, M.; Zhai, J.; Wang, Z. L. Magnetic-Mechanical-Electrical-Optical Coupling Effects in GaN-Based Led/Rare-Earth Terfenol-D Structures. *Adv. Mater.* **2014**, *26*, 6767–6772.
- (114) Peng, M. Z.; Liu, Y. D.; Yu, A. F.; Zhang, Y.; Liu, C. H.; Liu, J. Y.; Wu, W.; Zhang, K.; Shi, X. Q.; Kou, J. Z.; et al. Flexible Self-Powered GaN Ultraviolet Photoswitch with Piezo-Phototronic Effect Enhanced on/Off Ratio. *ACS Nano* **2016**, *10*, 1572–1579.
- (115) Zhang, K.; Zhai, J. Y.; Wang, Z. L. A Monolayer Mos<sub>2</sub> P-N Homogenous Photodiode with Enhanced Photoresponse by Piezo-Phototronic Effect. *2D Mater.* **2018**, *5*, 035038.
- (116) Zhang, K.; Peng, M. Z.; Wu, W.; Guo, J. M.; Gao, G. Y.; Liu, Y. D.; Kou, J. Z.; Wen, R. M.; Lei, Y.; Yu, A. F.; et al. A Flexible P-CuO/N-Mos<sub>2</sub> Heterojunction Photodetector with Enhanced Photoresponse by the Piezo-Phototronic Effect. *Mater. Horiz.* **2017**, *4*, 274–280.
- (117) Jiang, C. Y.; Jing, L.; Huang, X.; Liu, M. M.; Du, C. H.; Liu, T.; Pu, X.; Hu, W. G.; Wang, Z. L. Enhanced Solar Cell Conversion Efficiency of InGaN/GaN Multiple Quantum Wells by Piezo-Phototronic Effect. *ACS Nano* **2017**, *11*, 9405–9412.
- (118) Wang, L. F.; Liu, S. H.; Feng, X. L.; Xu, Q.; Bai, S.; Zhu, L. P.; Chen, L. B.; Qin, Y.; Wang, Z. L. Ultrasensitive Vertical Piezotronic Transistor Based on ZnO Twin Nanoplatelet. *ACS Nano* **2017**, *11*, 4859–4865.
- (119) Colinge, J. P. *Physics of Semiconductor Devices*; Wiley, 1981.
- (120) Wang, X. F.; Peng, W. B.; Yu, R. M.; Zou, H. Y.; Dai, Y. J.; Zi, Y. L.; Wu, C. S.; Li, S. T.; Wang, Z. L. Simultaneously Enhancing Light Emission and Suppressing Efficiency Droop in GaN Microwire-Based Ultraviolet Light-Emitting Diode by the Piezo-Phototronic Effect. *Nano Lett.* **2017**, *17*, 3718–3724.
- (121) Pan, C. F.; Chen, M. X.; Yu, R. M.; Yang, Q.; Hu, Y. F.; Zhang, Y.; Wang, Z. L. Progress in Piezo-Phototronic-Effect-Enhanced Light-Emitting Diodes and Pressure Imaging. *Adv. Mater.* **2016**, *28*, 1535–1552.
- (122) Li, X. Y.; Liang, R. R.; Tao, J.; Peng, Z. C.; Xu, Q. M.; Han, X.; Wang, X. D.; Wang, C. F.; Zhu, J.; Pan, C. F.; et al. Flexible Light Emission Diode Arrays Made of Transferred Si Microwires-ZnO Nanofilm with Piezo-Phototronic Effect Enhanced Lighting. *ACS Nano* **2017**, *11*, 3883–3889.
- (123) Huang, X.; Jiang, C. Y.; Du, C. H.; Jing, L.; Liu, M. M.; Hu, W. G.; Wang, Z. L. Enhanced Luminescence Performance of

Quantum Wells by Coupling Piezo-Phototronic with Plasmonic Effects. *ACS Nano* **2016**, *10*, 11420–11427.

(124) Du, C.; Jing, L.; Jiang, C.; Liu, T.; Pu, X.; Sun, J.; Li, D.; Hu, W. An Effective Approach to Alleviating the Thermal Effect in Microstripe Array-Leds Via the Piezo-Phototronic Effect. *Mater. Horiz.* **2018**, *5*, 116–122.

(125) Liu, Y.; Niu, S. M.; Yang, Q.; Klein, B. D. B.; Zhou, Y. S.; Wang, Z. L. Theoretical Study of Piezo-Phototronic Nano-Leds. *Adv. Mater.* **2014**, *26*, 7209–7216.

(126) Liu, Y.; Yang, Q.; Zhang, Y.; Yang, Z. Y.; Wang, Z. L. Nanowire Piezo-Phototronic Photodetector: Theory and Experimental Design. *Adv. Mater.* **2012**, *24*, 1410–1417.

(127) Wang, Z. N.; Yu, R. M.; Wen, X. N.; Liu, Y.; Pan, C. F.; Wu, W. Z.; Wang, Z. L. Optimizing Performance of Silicon-Based P-N Junction Photodetectors by the Piezo-Phototronic Effect. *ACS Nano* **2014**, *8*, 12866–12873.

(128) Neamen, D. *Semiconductor Physics and Devices*, 3rd ed.; McGraw-Hill: New York, 2006.

(129) Zhang, Z.; Yao, K.; Liu, Y.; Jin, C.; Liang, X.; Chen, Q.; Peng, L. M. Quantitative Analysis of Current-Voltage Characteristics of Semiconducting Nanowires: Decoupling of Contact Effects. *Adv. Funct. Mater.* **2007**, *17*, 2478–2489.

(130) Zhang, X. J.; Ji, W.; Tang, S. H. Determination of Optical Nonlinearities and Carrier Lifetime in ZnO. *J. Opt. Soc. Am. B* **1997**, *14*, 1951–1955.

(131) Lin, P.; Zhu, L. P.; Li, D.; Xu, L.; Pan, C. F.; Wang, Z. L. Piezo-Phototronic Effect for Enhanced Flexible Mos2/Wse2 Van Der Waals Photodiodes. *Adv. Funct. Mater.* **2018**, *28*, 1802849.

(132) Vandewal, K.; Tvingstedt, K.; Gadisa, A.; Inganas, O.; Manca, J. V. On the Origin of the Open-Circuit Voltage of Polymer-Fullerene Solar Cells. *Nat. Mater.* **2009**, *8*, 904–909.

(133) Godfrey, R. B.; Green, M. A. 655 Mv Open-Circuit Voltage, 17.6% Efficient Silicon Mis Solar Cells. *Appl. Phys. Lett.* **1979**, *34*, 790–793.

(134) Altındal, Ş.; Tataroğlu, A.; Dökme, İ. Density of Interface States, Excess Capacitance and Series Resistance in the Metal-Insulator-Semiconductor (Mis) Solar Cells. *Sol. Energy Mater. Sol. Cells* **2005**, *85*, 345–358.

(135) Brendel, R.; Queisser, H. J. On the Thickness Dependence of Open Circuit Voltages of P-N Junction Solar Cells. *Sol. Energy Mater. Sol. Cells* **1993**, *29*, 397–401.

(136) Chen, H.-Y.; Hou, J.; Zhang, S.; Liang, Y.; Yang, G.; Yang, Y.; Yu, L.; Wu, Y.; Li, G. Polymer Solar Cells with Enhanced Open-Circuit Voltage and Efficiency. *Nat. Photonics* **2009**, *3*, 649–653.

(137) Yuan, Y.; Reece, T. J.; Sharma, P.; Poddar, S.; Ducharme, S.; Gruverman, A.; Yang, Y.; Huang, J. Efficiency Enhancement in Organic Solar Cells with Ferroelectric Polymers. *Nat. Mater.* **2011**, *10*, 296–302.

(138) Zhang, Y.; Yang, Y.; Wang, Z. L. Piezo-Phototronics Effect on Nano/Microwire Solar Cells. *Energy Environ. Sci.* **2012**, *5*, 6850–6856.

(139) Janotti, A.; Van, d. W.; Chris, G. Fundamentals of Zinc Oxide as a Semiconductor. *Rep. Prog. Phys.* **2009**, *72*, 126501.

(140) Look, D. C.; Farlow, G. C.; Reunchan, P.; Limpijumnong, S.; Zhang, S. B.; Nordlund, K. Evidence for Native-Defect Donors in N-Type ZnO. *Phys. Rev. Lett.* **2005**, *95*, 225502.

(141) Wen, X. N.; Wu, W. Z.; Wang, Z. L. Effective Piezo-Phototronic Enhancement of Solar Cell Performance by Tuning Material Properties. *Nano Energy* **2013**, *2*, 1093–1100.

(142) Li, X.; Qi, J.; Zhang, Q.; Zhang, Y. Temperature-Dependent Electron Transport in ZnO Micro/Nanowires. *J. Appl. Phys.* **2012**, *112*, No. 084313.

(143) Hu, Y. F.; Klein, B. D. B.; Su, Y. J.; Niu, S. M.; Liu, Y.; Wang, Z. L. Temperature Dependence of the Piezotronic Effect in ZnO Nanowires. *Nano Lett.* **2013**, *13*, 5026–5032.

(144) Wang, X. F.; Yu, R. M.; Peng, W. B.; Wu, W. Z.; Li, S. T.; Wang, Z. L. Temperature Dependence of the Piezotronic and Piezophototronic Effects in a-Axis Gan Nanobelts. *Adv. Mater.* **2015**, *27*, 8067–8074.

(145) Yu, R. M.; Wang, X. F.; Wu, W. Z.; Pan, C. F.; Bando, Y.; Fukata, N.; Hu, Y. F.; Peng, W. B.; Ding, Y.; Wang, Z. L. Temperature Dependence of the Piezophototronic Effect in Cds Nanowires. *Adv. Funct. Mater.* **2015**, *25*, 5277–5284.

(146) Xue, F.; Zhang, L.; Tang, W.; Zhang, C.; Du, W.; Wang, Z. L. Piezotronic Effect on ZnO Nanowire Film Based Temperature Sensor. *ACS Appl. Mater. Interfaces* **2014**, *6*, 5955–5961.

(147) Bao, R. R.; Wang, C. F.; Dong, L.; Yu, R. M.; Zhao, K.; Wang, Z. L.; Pan, C. F. Flexible and Controllable Piezo-Phototronic Pressure Mapping Sensor Matrix by ZnO Nw/P-Polymer Led Array. *Adv. Funct. Mater.* **2015**, *25*, 2884–2891.

(148) Zhu, Y. G.; Wang, Y.; Shi, Y.; Wong, J. I.; Yang, H. Y. Coo Nanoflowers Woven by Cnt Network for High Energy Density Flexible Micro-Supercapacitor. *Nano Energy* **2014**, *3*, 46–54.

(149) Rueckes, T.; Kim, K.; Joselevich, E.; Tseng, G. Y.; Cheung, C. L.; Lieber, C. M. Carbon Nanotube-Based Nonvolatile Random Access Memory for Molecular Computing. *Science* **2000**, *289*, 94–97.

(150) Shen, Y.; Xia, L.; Zhang, H.; Liu, X.; Yang, A.; Shi, J.; Zhang, L.; Liao, Q.; Zhang, Y. Plasma-Induced Field Emission Study of Carbon Nanotube Cathode. *Phys. Rev. Spec. Top.-Accel. Beams* **2011**, *14*, 7.

(151) Fang, X.; Shen, C.; Ge, M.; Rong, J.; Liu, Y.; Zhang, A.; Wei, F.; Zhou, C. High-Power Lithium Ion Batteries Based on Flexible and Light-Weight Cathode of Lini0.5mn1.5o4/Carbon Nanotube Film. *Nano Energy* **2015**, *12*, 43–51.

(152) Wang, X.; Li, Z.; Xu, W.; Kulkarni, S. A.; Batabyal, S. K.; Zhang, S.; Cao, A.; Wong, L. H. Tio2 Nanotube Arrays Based Flexible Perovskite Solar Cells with Transparent Carbon Nanotube Electrode. *Nano Energy* **2015**, *11*, 728–735.

(153) Zhou, Y. S.; Hinchet, R.; Yang, Y.; Ardila, G.; Songmuang, R.; Zhang, F.; Zhang, Y.; Han, W. H.; Pradel, K.; Montes, L.; et al. Nano-Newton Transverse Force Sensor Using a Vertical Gan Nanowire Based on the Piezotronic Effect. *Adv. Mater.* **2013**, *25*, 883–888.

(154) Xue, F.; Zhang, L. M.; Tang, W.; Zhang, C.; Du, W. M.; Wang, Z. L. Piezotronic Effect on ZnO Nanowire Film Based Temperature Sensor. *ACS Appl. Mater. Interfaces* **2014**, *6*, 5955–5961.

(155) Wu, J. M.; Chen, K. H.; Zhang, Y.; Wang, Z. L. A Self-Powered Piezotronic Strain Sensor Based on Single Znsno3Microbelts. *RSC Adv.* **2013**, *3*, 25184–25189.

(156) Wu, J. M.; Chen, C. Y.; Zhang, Y.; Chen, K. H.; Yang, Y.; Hu, Y. F.; He, J. H.; Wang, Z. L. Ultrahigh Sensitive Piezotronic Strain Sensors Based on a Znsno3 Nanowire/Microwire. *ACS Nano* **2012**, *6*, 4369–4374.

(157) Wang, Z. N.; Yu, R. M.; Pan, C. F.; Liu, Y.; Ding, Y.; Wang, Z. L. Piezo-Phototronic Uv/Visible Photoresistor with Optical-Fiber-Nanowire Hybridized Structures. *Adv. Mater.* **2015**, *27*, 1553.

(158) Niu, S. M.; Hu, Y. F.; Wen, X. N.; Zhou, Y. S.; Zhang, F.; Lin, L.; Wang, S. H.; Wang, Z. L. Enhanced Performance of Flexible ZnO Nanowire Based Room-Temperature Oxygen Sensors by Piezotronic Effect. *Adv. Mater.* **2013**, *25*, 3701–3706.

(159) Liu, S. H.; Wang, L. F.; Wang, Z.; Cai, Y. F.; Feng, X. L.; Qin, Y.; Wang, Z. L. Double-Channel Piezotronic Transistors for Highly Sensitive Pressure Sensing. *ACS Nano* **2018**, *12*, 1732–1738.

(160) Frömling, T.; Yu, R.; Mintken, M.; Adlung, R.; Rödel, J. Piezotronic Sensors. *MRS Bull.* **2018**, *43*, 941–945.

(161) Li, X.; Lee, A.; Razavi, S. A.; Wu, H.; Wang, K. L. Voltage-Controlled Magnetoelectric Memory and Logic Devices. *MRS Bull.* **2018**, *43*, 970–977.

(162) Yang, Y.; Liao, Q.; Qi, J.; Guo, W.; Zhang, Y. Synthesis and Transverse Electromechanical Characterization of Single Crystalline ZnO Nanoleaves. *Phys. Chem. Chem. Phys.* **2010**, *12*, 552–555.

(163) Sun, K.; Qi, J.; Zhang, Q.; Yang, Y.; Zhang, Y. A Novel Logic Switch Based on Individual ZnO Nanotetrapods. *Nanoscale* **2011**, *3*, 2166–2168.

(164) Wang, L.; Liu, S.; Gao, G.; Pang, Y.; Yin, X.; Feng, X.; Zhu, L.; Bai, Y.; Chen, L.; Xiao, T.; et al. Ultrathin Piezotronic Transistors with 2 Nm Channel Lengths. *ACS Nano* **2018**, *12*, 4903–4908.

- (165) Zhu, G. A.; Yang, R. S.; Wang, S. H.; Wang, Z. L. Flexible High-Output Nanogenerator Based on Lateral ZnO Nanowire Array. *Nano Lett.* **2010**, *10*, 3151–3155.
- (166) Yang, R. S.; Qin, Y.; Dai, L. M.; Wang, Z. L. Power Generation with Laterally Packaged Piezoelectric Fine Wires. *Nat. Nanotechnol.* **2009**, *4*, 34–39.
- (167) Wang, Z. L.; Yang, R. S.; Zhou, J.; Qin, Y.; Xu, C.; Hu, Y. F.; Xu, S. Lateral Nanowire/Nanobelt Based Nanogenerators, Piezotronics and Piezo-Phototronics. *Mater. Sci. Eng., R* **2010**, *70*, 320–329.
- (168) Wang, Z. L. Piezotronic and Piezophototronic Effects. *J. Phys. Chem. Lett.* **2010**, *1*, 1388–1393.
- (169) Tung, R. T. Recent Advances in Schottky Barrier Concepts. *Mater. Sci. Eng., R* **2001**, *35*, 1–138.
- (170) Morozovska, A. N.; Eliseev, E. A.; Svechnikov, S. V.; Krutov, A. D.; Shur, V. Y.; Borisevich, A. Y.; Maksymovych, P.; Kalinin, S. V. Finite Size and Intrinsic Field Effect on the Polar-Active Properties of Ferroelectric-Semiconductor Heterostructures. *Phys. Rev. B* **2010**, *81*, DOI: 10.1103/PhysRevB.81.205308
- (171) Han, W.; Zhou, Y.; Zhang, Y.; Chen, C.-Y.; Lin, L.; Wang, X.; Wang, S.; Wang, Z. L. Strain-Gated Piezotronic Transistors Based on Vertical Zinc Oxide Nanowires. *ACS Nano* **2012**, *6*, 3760–3766.
- (172) Zhou, Y. S.; Wang, K.; Han, W. H.; Rai, S. C.; Zhang, Y.; Ding, Y.; Pan, C. F.; Zhang, F.; Zhou, W. L.; Wang, Z. L. Vertically Aligned CdSe Nanowire Arrays for Energy Harvesting and Piezotronic Devices. *ACS Nano* **2012**, *6*, 6478–6482.
- (173) Hu, W.; Kalantar-Zadeh, K.; Gupta, K.; Liu, C.-P. Piezotronic Materials and Large-Scale Piezotronics Array Devices. *MRS Bull.* **2018**, *43*, 936–940.
- (174) Wu, W. Z.; Wen, X. N.; Wang, Z. L. Taxel-Addressable Matrix of Vertical-Nanowire Piezotronic Transistors for Active and Adaptive Tactile Imaging. *Science* **2013**, *340*, 952–957.
- (175) Zhu, G.; Lin, Z. H.; Jing, Q. S.; Bai, P.; Pan, C. F.; Yang, Y.; Zhou, Y. S.; Wang, Z. L. Toward Large-Scale Energy Harvesting by a Nanoparticle-Enhanced Triboelectric Nanogenerator. *Nano Lett.* **2013**, *13*, 847–853.
- (176) Zhu, G.; Bai, P.; Chen, J.; Lin Wang, Z. Power-Generating Shoe Insole Based on Triboelectric Nanogenerators for Self-Powered Consumer Electronics. *Nano Energy* **2013**, *2*, 688–692.
- (177) Zheng, X.; Sun, Y.; Yan, X.; Chen, X.; Bai, Z.; Lin, P.; Shen, Y.; Zhao, Y.; Zhang, Y. Tunable Channel Width of a Uv-Gate Field Effect Transistor Based on ZnO Micro-Nano Wire. *RSC Adv.* **2014**, *4*, 18378.
- (178) Zhang, Y.; Yang, Y.; Wang, Z. L. Piezo-Phototronics Effect on Nano/Microwire Solar Cells. *Energy Environ. Sci.* **2012**, *5*, 6850.
- (179) Zhang, Y.; Wang, Z. L. Theory of Piezo-Phototronics for Light-Emitting Diodes. *Adv. Mater.* **2012**, *24*, 4712–4718.
- (180) Yi, F.; Liao, Q.; Huang, Y.; Gu, Y.; Zhang, Y. Self-Powered Ultraviolet Photodetector Based on a Single ZnO Tetrapod/Pedot:Pss Heterostructure. *Semicond. Sci. Technol.* **2013**, *28*, 105023.
- (181) Xu, S.; Wei, Y.; Kirkham, M.; Liu, J.; Mai, W.; Davidovic, D.; Snyder, R. L.; Wang, Z. L. Patterned Growth of Vertically Aligned ZnO Nanowire Arrays on Inorganic Substrates at Low Temperature without Catalyst. *J. Am. Chem. Soc.* **2008**, *130*, 14958–14959.
- (182) Wang, Z.; Qi, J.; Yan, X.; Zhang, Q.; Wang, Q.; Lu, S.; Lin, P.; Liao, Q.; Zhang, Z.; Zhang, Y. A Self-Powered Strain Sensor Based on a ZnO/Pedot:Pss Hybrid Structure. *RSC Adv.* **2013**, *3*, 17011.
- (183) Akyildiz, I. F.; Su, W.; Sankarasubramaniam, Y.; Cayirci, E. Wireless Sensor Networks: A Survey. *Comput. Netw.* **2002**, *38*, 393–422.
- (184) Bai, Z.; Chen, X.; Yan, X.; Zheng, X.; Kang, Z.; Zhang, Y. Self-Powered Ultraviolet Photodetectors Based on Selectively Grown ZnO Nanowire Arrays with Thermal Tuning Performance. *Phys. Chem. Chem. Phys.* **2014**, *16*, 9525–9529.
- (185) Bai, Z.; Yan, X.; Chen, X.; Zhao, K.; Lin, P.; Zhang, Y. High Sensitivity, Fast Speed and Self-Powered Ultraviolet Photodetectors Based on ZnO Micro/Nanowire Networks. *Prog. Nat. Sci.* **2014**, *24*, 1–5.
- (186) Burschka, J.; Pellet, N.; Moon, S.-J.; Humphry-Baker, R.; Gao, P.; Nazeeruddin, M. K.; Graetzel, M. Sequential Deposition as a Route to High-Performance Perovskite-Sensitized Solar Cells. *Nature* **2013**, *499*, 316.
- (187) Chen, X.; Bai, Z.; Yan, X.; Yuan, H.; Zhang, G.; Lin, P.; Zhang, Z.; Liu, Y.; Zhang, Y. Design of Efficient Dye-Sensitized Solar Cells with Patterned ZnO-Zns Core-Shell Nanowire Array Photoanodes. *Nanoscale* **2014**, *6*, 4691.
- (188) Chen, X.; Yan, X.; Bai, Z.; Shen, Y.; Wang, Z.; Dong, X.; Duan, X.; Zhang, Y. High-Throughput Fabrication of Large-Scale Highly Ordered ZnO Nanorod Arrays Via Three-Beam Interference Lithography. *CrystEngComm* **2013**, *15*, 8416.
- (189) Gao, Z.; Zhou, J.; Gu, Y.; Fei, P.; Hao, Y.; Bao, G.; Wang, Z. L. Effects of Piezoelectric Potential on the Transport Characteristics of Metal-ZnO Nanowire-Metal Field Effect Transistor. *J. Appl. Phys.* **2009**, *105*, 113707.
- (190) Guo, J.; Wen, R.; Liu, Y.; Zhang, K.; Kou, J.; Zhai, J.; Wang, Z. L. Piezotronic Effect Enhanced Flexible Humidity Sensing of Monolayer Mos2. *ACS Appl. Mater. Interfaces* **2018**, *10*, 8110–8116.
- (191) Guo, W.; Yang, Y.; Qi, J.; Zhang, Y. Room Temperature Negative Differential Resistance Based on a Single ZnO Nanowire/Cupc Nanofilm Hybrid Heterojunction. *Appl. Phys. Lett.* **2010**, *97*, 263118.
- (192) Monroy, E.; Munoz, E.; Sanchez, F. J.; Calle, F.; Calleja, E.; Beaumont, B.; Gibart, P.; Munoz, J. A.; Cusso, F. High-Performance Gan P-N Junction Photodetectors for Solar Ultraviolet Applications. *Semicond. Sci. Technol.* **1998**, *13*, 1042–1046.
- (193) Pimpurkar, S.; Speck, J. S.; DenBaars, S. P.; Nakamura, S. Prospects for Led Lighting. *Nat. Photonics.* **2009**, *3*, 179–181.
- (194) Ruh, D.; Reith, P.; Sherman, S.; Theodor, M.; Ruhhammer, J.; Seifert, A.; Zappe, H. Stretchable Optoelectronic Circuits Embedded in a Polymer Network. *Adv. Mater.* **2014**, *26*, 1706–1710.
- (195) Sarasqueta, G.; Choudhury, K. R.; Subbiah, J.; So, F. Organic and Inorganic Blocking Layers for Solution-Processed Colloidal Pbse Nanocrystal Infrared Photodetectors. *Adv. Funct. Mater.* **2011**, *21*, 167–171.
- (196) Si, H.; Kang, Z.; Liao, Q.; Zhang, Z.; Zhang, X.; Wang, L.; Zhang, Y. Design and Tailoring of Patterned ZnO Nanostructures for Energy Conversion Applications. *Sci. China Mater.* **2017**, *60*, 793–810.
- (197) Tsukazaki, A.; Ohtomo, A.; Onuma, T.; Ohtani, M.; Makino, T.; Sumiya, M.; Ohtani, K.; Chichibu, S. F.; Fuke, S.; Segawa, Y. Repeated Temperature Modulation Epitaxy for P-Type Doping and Light-Emitting Diode Based on ZnO. *Nat. Mater.* **2004**, *4*, 42–46.
- (198) Wen, X.; Wu, W.; Pan, C.; Hu, Y.; Yang, Q.; Lin Wang, Z. Development and Progress in Piezotronics. *Nano Energy* **2015**, *14*, 276–295.
- (199) Xing, Y.; Chaudry, Q.; Shen, C.; Kong, K. Y.; Zhau, H. E.; Wchung, L.; Petros, J. A.; O'Regan, R. M.; Yezhelyev, M. V.; Simons, J. W.; et al. Bioconjugated Quantum Dots for Multiplexed and Quantitative Immunohistochemistry. *Nat. Protoc.* **2007**, *2*, 1152–1165.
- (200) Yang, Y.; Guo, W.; Wang, X.; Wang, Z.; Qi, J.; Zhang, Y. Size Dependence of Dielectric Constant in a Single Pencil-Like ZnO Nanowire. *Nano Lett.* **2012**, *12*, 1919–1922.
- (201) Zhang, X.-S.; Han, M.-D.; Wang, R.-X.; Meng, B.; Zhu, F.-Y.; Sun, X.-M.; Hu, W.; Wang, W.; Li, Z.-H.; Zhang, H.-X. High-Performance Triboelectric Nanogenerator with Enhanced Energy Density Based on Single-Step Fluorocarbon Plasma Treatment. *Nano Energy* **2014**, *4*, 123–131.
- (202) Xu, S.; Wang, Z. L. One-Dimensional ZnO Nanostructures: Solution Growth and Functional Properties. *Nano Res.* **2011**, *4*, 1013–1098.
- (203) Xi, P. Semiconductor Physics and Devices. *Mater. Today* **2006**, *9*, 57.
- (204) Wu, W.; Wang, L.; Yu, R.; Liu, Y.; Wei, S. H.; Hone, J.; Wang, Z. L. Piezophototronic Effect in Single-Atomic-Layer Mos2 for Strain-Gated Flexible Optoelectronics. *Adv. Mater.* **2016**, *28*, 8463–8468.
- (205) Wang, Z.; Qi, J.; Lu, S.; Li, P.; Li, X.; Zhang, Y. Enhancing Sensitivity of Force Sensor Based on a ZnO Tetrapod by Piezo-Phototronic Effect. *Appl. Phys. Lett.* **2013**, *103*, 143125.

- (206) Rong, H.; Xu, S.; Kuo, Y.-H.; Sih, V.; Cohen, O.; Raday, O.; Paniccia, M. Low-Threshold Continuous-Wave Raman Silicon Laser. *Nat. Photonics* **2007**, *1*, 232–237.
- (207) Qin, Z.; Huang, Y.; Qi, J.; Liao, Q.; Wang, W.; Zhang, Y. Surface Destruction and Performance Reduction of the ZnO Nanowire Arrays Electrode in Dye Sensitization Process. *Mater. Lett.* **2011**, *65*, 3506–3508.
- (208) Momeni, K.; Odegard, G. M.; Yassar, R. S. Nanocomposite Electrical Generator Based on Piezoelectric Zinc Oxide Nanowires. *J. Appl. Phys.* **2010**, *108*, 114303.
- (209) Zhou, J.; Gu, Y.; Hu, Y.; Mai, W.; Yeh, P.-H.; Bao, G.; Sood, A. K.; Polla, D. L.; Wang, Z. L. Gigantic Enhancement in Response and Reset Time of ZnO UV Nanosensor by Utilizing Schottky Contact and Surface Functionalization. *Appl. Phys. Lett.* **2009**, *94*, 191103.
- (210) Wei, T.-Y.; Yeh, P.-H.; Lu, S.-Y.; Wang, Z. L. Gigantic Enhancement in Sensitivity Using Schottky Contacted Nanowire Nanosensor. *J. Am. Chem. Soc.* **2009**, *131*, 17690–17695.
- (211) Yeh, P.-H.; Li, Z.; Wang, Z. L. Schottky-Gated Probe-Free ZnO Nanowire Biosensor. *Adv. Mater.* **2009**, *21*, 4975–4978.
- (212) Pan, C. F.; Yu, R. M.; Niu, S. M.; Zhu, G.; Wang, Z. L. Piezotronic Effect on the Sensitivity and Signal Level of Schottky Contacted Proactive Micro/Nanowire Nanosensors. *ACS Nano* **2013**, *7*, 1803–1810.
- (213) Yu, R. M.; Pan, C. F.; Wang, Z. L. High Performance of ZnO Nanowire Protein Sensors Enhanced by the Piezotronic Effect. *Energy Environ. Sci.* **2013**, *6*, 494–499.
- (214) Yu, R. M.; Pan, C. F.; Chen, J.; Zhu, G.; Wang, Z. L. Enhanced Performance of a ZnO Nanowire-Based Self-Powered Glucose Sensor by Piezotronic Effect. *Adv. Funct. Mater.* **2013**, *23*, 5868–5874.
- (215) Han, Y.; Gao, C.; Zhu, H.; Chen, S.; Jiang, Q.; Li, T.; Willander, M.; Cao, X.; Wang, N. Piezotronic Effect Enhanced Nanowire Sensing of H<sub>2</sub>O<sub>2</sub> Released by Cells. *Nano Energy* **2015**, *13*, 405–413.
- (216) Cao, X. T.; Cao, X.; Guo, H. J.; Li, T.; Jie, Y.; Wang, N.; Wang, Z. L. Piezotronic Effect Enhanced Label-Free Detection of DNA Using a Schottky-Contacted ZnO Nanowire Biosensor. *ACS Nano* **2016**, *10*, 8038–8044.
- (217) Brillson, L. J.; Lu, Y. ZnO Schottky Barriers and Ohmic Contacts. *J. Appl. Phys.* **2011**, *109*, 121301.
- (218) Kou, L.; Huang, T.; Zheng, B.; Han, Y.; Zhao, X.; Gopalsamy, K.; Sun, H.; Gao, C. Coaxial Wet-Spun Yarn Supercapacitors for High-Energy Density and Safe Wearable Electronics. *Nat. Commun.* **2014**, *5*, 3754.
- (219) Muller, B. *Device Electronics for Integrated Circuits*; John Wiley & Sons, 1986.
- (220) Pan, C.; Guo, W.; Dong, L.; Zhu, G.; Wang, Z. L. Optical Fiber-Based Core-Shell Coaxially Structured Hybrid Cells for Self-Powered Nanosystems. *Adv. Mater.* **2012**, *24*, 3356–3361.
- (221) Pan, C.; Wu, H.; Wang, C.; Wang, B.; Zhang, L.; Cheng, Z.; Hu, P.; Pan, W.; Zhou, Z.; Yang, X.; et al. Nanowire-Based High Performance “Micro Fuel Cell”: One Nanowire, One Fuel Cell. *Adv. Mater.* **2008**, *20*, 1644.
- (222) Weerasinghe, H. C.; Huang, F.; Cheng, Y.-B. Fabrication of Flexible Dye Sensitized Solar Cells on Plastic Substrates. *Nano Energy* **2013**, *2*, 174–189.
- (223) Zhou, Y. Enhancement of Photovoltaic Effect in Nanoscale Polarization Graded Ferroelectrics. *Sol. Energy* **2012**, *86*, 811–815.
- (224) Yang, W. S.; Noh, J. H.; Jeon, N. J.; Kim, Y. C.; Ryu, S.; Seo, J.; Seok, S. I. High-Performance Photovoltaic Perovskite Layers Fabricated through Intramolecular Exchange. *Science* **2015**, *348*, 1234–1237.
- (225) Wang, Z. L.; Zhu, G.; Yang, Y.; Wang, S.; Pan, C. Progress in Nanogenerators for Portable Electronics. *Mater. Today* **2012**, *15*, 532–543.
- (226) Shi, J.; Zhao, P.; Wang, X. Piezoelectric-Polarization-Enhanced Photovoltaic Performance in Depleted-Heterojunction Quantum-Dot Solar Cells. *Adv. Mater.* **2013**, *25*, 916–921.
- (227) Pan, C.; Li, Z.; Guo, W.; Zhu, J.; Wang, Z. L. Fiber-Based Hybrid Nanogenerators for/as Self-Powered Systems in Biological Liquid. *Angew. Chem.* **2011**, *123*, 11388–11392.
- (228) Liu, M.; Johnston, M. B.; Snaith, H. J. Efficient Planar Heterojunction Perovskite Solar Cells by Vapour Deposition. *Nature* **2013**, *501*, 395.
- (229) Espinosa, H. D.; Bernal, R. A.; Minary-Jolandan, M. A Review of Mechanical and Electromechanical Properties of Piezoelectric Nanowires. *Adv. Mater.* **2012**, *24*, 4656–4675.
- (230) Boxberg, F.; Sondergaard, N.; Xu, H. Q. Photovoltaics with Piezoelectric Core-Shell Nanowires. *Nano Lett.* **2010**, *10*, 1108–1112.
- (231) Golam Sarwar, A. T. M.; Myers, R. C. Exploiting Piezoelectric Charge for High Performance Graded InGaN Nanowire Solar Cells. *Appl. Phys. Lett.* **2012**, *101*, 143905.
- (232) Shoaee, S.; Briscoe, J.; Durrant, J. R.; Dunn, S. Acoustic Enhancement of Polymer/ZnO Nanorod Photovoltaic Device Performance. *Adv. Mater.* **2014**, *26*, 263–268.
- (233) Tang, H.; Liu, B.; Wang, T. Influence of Piezoelectric Fields on InGaN Based Intermediate Band Solar Cells. *J. Phys. D: Appl. Phys.* **2015**, *48*, No. 025101.
- (234) Pan, C.; Niu, S.; Ding, Y.; Dong, L.; Yu, R.; Liu, Y.; Zhu, G.; Wang, Z. L. Enhanced Cu(2)S/Cds Coaxial Nanowire Solar Cells by Piezo-Phototronic Effect. *Nano Lett.* **2012**, *12*, 3302–3307.
- (235) Hu, G. F.; Guo, W. X.; Yu, R. M.; Yang, X. N.; Zhou, R. R.; Pan, C. F.; Wang, Z. L. Enhanced Performances of Flexible ZnO/Perovskite Solar Cells by Piezo-Phototronic Effect. *Nano Energy* **2016**, *23*, 27–33.
- (236) Zhu, L. P.; Wang, L. F.; Pan, C. F.; Chen, L. B.; Xue, F.; Chen, B. D.; Yang, L. J.; Su, L.; Wang, Z. L. Enhancing the Efficiency of Silicon-Based Solar Cells by the Piezo-Phototronic Effect. *ACS Nano* **2017**, *11*, 1894–1900.
- (237) Zhu, L. P.; Wang, L. F.; Xue, F.; Chen, L. B.; Fu, J. Q.; Feng, X. L.; Li, T. F.; Wang, Z. L. Piezo-Phototronic Effect Enhanced Flexible Solar Cells Based on N-ZnO/P-Sns Core-Shell Nanowire Array. *Adv. Sci.* **2017**, *4*, 1600185.
- (238) Zhang, K.; Peng, M.; Wu, W.; Guo, J.; Gao, G.; Liu, Y.; Kou, J.; Wen, R.; Lei, Y.; Yu, A.; et al. A Flexible P-CuO/N-MoS<sub>2</sub> Heterojunction Photodetector with Enhanced Photoresponse by the Piezo-Phototronic Effect. *Mater. Horiz.* **2017**, *4*, 274–280.
- (239) Yu, R. M.; Pan, C. F.; Hu, Y. F.; Li, L.; Liu, H. F.; Liu, W.; Chua, S.; Chi, D. Z.; Wang, Z. L. Enhanced Performance of Gan Nanobelt-Based Photodetectors by Means of Piezotronic Effects. *Nano Res.* **2013**, *6*, 758–766.
- (240) Xie, C.; Nie, B.; Zeng, L.; Liang, F.-X.; Wang, M.-Z.; Luo, L.; Feng, M.; Yu, Y.; Wu, C.-Y.; Wu, Y.; et al. Core-Shell Heterojunction of Silicon Nanowire Arrays and Carbon Quantum Dots for Photovoltaic Devices and Self-Driven Photodetectors. *ACS Nano* **2014**, *8*, 4015–4022.
- (241) Lin, P.; Yan, X.; Liu, Y.; Li, P.; Lu, S.; Zhang, Y. A Tunable ZnO/Electrolyte Heterojunction for a Self-Powered Photodetector. *Phys. Chem. Chem. Phys.* **2014**, *16*, 26697–26700.
- (242) Li, X.; Qi, J.; Zhang, Q.; Zhang, Y. Bias-Tunable Dual-Mode Ultraviolet Photodetectors for Photoelectric Tachometer. *Appl. Phys. Lett.* **2014**, *104*, No. 041108.
- (243) Yang, Q.; Guo, X.; Wang, W.; Zhang, Y.; Xu, S.; Lien, D. H.; Wang, Z. L. Enhancing Sensitivity of a Single ZnO Micro-/Nanowire Photodetector by Piezo-Phototronic Effect. *ACS Nano* **2010**, *4*, 6285–6291.
- (244) Dong, L.; Niu, S.; Pan, C.; Yu, R.; Zhang, Y.; Wang, Z. L. Piezo-Phototronic Effect of CdSe Nanowires. *Adv. Mater.* **2012**, *24*, 5470–5475.
- (245) Peng, M.; Liu, Y.; Yu, A.; Zhang, Y.; Liu, C.; Liu, J.; Wu, W.; Zhang, K.; Shi, X.; Kou, J.; et al. Flexible Self-Powered Gan Ultraviolet Photoswitch with Piezo-Phototronic Effect Enhanced on/Off Ratio. *ACS Nano* **2016**, *10*, 1572–1579.
- (246) Zhang, F.; Ding, Y.; Zhang, Y.; Zhang, X. L.; Wang, Z. L. Piezo-Phototronic Effect Enhanced Visible and Ultraviolet Photodetection Using a ZnO-Cds Core-Shell Micro/Nanowire. *ACS Nano* **2012**, *6*, 9229–9236.

- (247) Zhang, F.; Niu, S. M.; Guo, W. X.; Zhu, G.; Liu, Y.; Zhang, X. L.; Wang, Z. L. Piezo-Phototronic Effect Enhanced Visible/Uv Photodetector of a Carbon-Fiber/Zno-Cds Double-Shell Microwire. *ACS Nano* **2013**, *7*, 4537–4544.
- (248) Rai, S. C.; Wang, K.; Ding, Y.; Marmon, J. K.; Bhatt, M.; Zhang, Y.; Zhou, W. L.; Wang, Z. L. Piezo-Phototronic Effect Enhanced Uv/Visible Photodetector Based on Fully Wide Band Gap Type-Ii Zno/Zns Core/Shell Nanowire Array. *ACS Nano* **2015**, *9*, 6419–6427.
- (249) Zhang, Z.; Liao, Q.; Yu, Y.; Wang, X.; Zhang, Y. Enhanced Photoresponse of Zno Nanorods-Based Self-Powered Photodetector by Piezotronic Interface Engineering. *Nano Energy* **2014**, *9*, 237–244.
- (250) Wang, Z. N.; Yu, R. M.; Wang, X. F.; Wu, W. Z.; Wang, Z. L. Ultrafast Response P-Si/N-Zno Heterojunction Ultraviolet Detector Based on Pyro-Phototronic Effect. *Adv. Mater.* **2016**, *28*, 6880.
- (251) Wang, Z.; Yu, R.; Pan, C.; Li, Z.; Yang, J.; Yi, F.; Wang, Z. L. Light-Induced Pyroelectric Effect as an Effective Approach for Ultrafast Ultraviolet Nanosensing. *Nat. Commun.* **2015**, *6*, DOI: 10.1038/ncomms9401
- (252) Wang, Z.; Yu, R.; Wen, X.; Liu, Y.; Pan, C.; Wu, W.; Wang, Z. L. Optimizing Performance of Silicon-Based P-N Junction Photodetectors by the Piezo-Phototronic Effect. *ACS Nano* **2014**, *8*, 12866–12873.
- (253) Han, X.; Du, W. M.; Yu, R. M.; Pan, C. F.; Wang, Z. L. Piezo-Phototronic Enhanced Uv Sensing Based on a Nanowire Photodetector Array. *Adv. Mater.* **2015**, *27*, 7963–7969.
- (254) Wu, W.; Wang, X.; Han, X.; Yang, Z.; Gao, G.; Zhang, Y.; Hu, J.; Tan, Y.; Pan, A.; Pan, C. Flexible Photodetector Arrays Based on Patterned Ch3nh3pb3–Xclx Perovskite Film for Real-Time Photosensing and Imaging. *Adv. Mater.* **2019**, *31*, 1805913.
- (255) Zhong, J.; Zhong, Q.; Fan, F.; Zhang, Y.; Wang, S.; Hu, B.; Wang, Z. L.; Zhou, J. Finger Typing Driven Triboelectric Nanogenerator and Its Use for Instantaneously Lighting up Leds. *Nano Energy* **2013**, *2*, 491–497.
- (256) Zhao, Z. F.; Pu, X.; Han, C. B.; Du, C. H.; Li, L. X.; Jiang, C. Y.; Hu, W. G.; Wang, Z. L. Piezotronic Effect in Polarity-Controlled Gan Nanowires. *ACS Nano* **2015**, *9*, 8578–8583.
- (257) Zhang, G.; Liao, Q.; Ma, M.; Gao, F.; Zhang, Z.; Kang, Z.; Zhang, Y. Uniformly Assembled Vanadium Doped Zno Microflowers/ Bacterial Cellulose Hybrid Paper for Flexible Piezoelectric Nanogenerators and Self-Powered Sensors. *Nano Energy* **2018**, *52*, 501–509.
- (258) Xu, S.; Hansen, B. J.; Wang, Z. L. Piezoelectric-Nanowire-Enabled Power Source for Driving Wireless Microelectronics. *Nat. Commun.* **2010**, *1*, 93.
- (259) Nour, E. S.; Sandberg, M. O.; Willander, M.; Nur, O. Handwriting Enabled Harvested Piezoelectric Power Using Zno Nanowires/Polymer Composite on Paper Substrate. *Nano Energy* **2014**, *9*, 221–228.
- (260) Du, C. H.; Jiang, C. Y.; Zuo, P.; Huang, X.; Pu, X.; Zhao, Z. F.; Zhou, Y. L.; Li, L. X.; Chen, H.; Hu, W. G.; et al. Piezo-Phototronic Effect Controlled Dual-Channel Visible Light Communication (Pvlc) Using Ingan/Gan Multiquantum Well Nanopillars. *Small* **2015**, *11*, 6071–6077.
- (261) Du, C. H.; Huang, X.; Jiang, C. Y.; Pu, X.; Zhao, Z. F.; Jing, L.; Hu, W. G.; Wang, Z. L. Tuning Carrier Lifetime in Ingan/Gan Leds Via Strain Compensation for High-Speed Visible Light Communication. *Sci. Rep.* **2016**, *6*, DOI: 10.1038/srep37132
- (262) Liu, Y.; Niu, S.; Yang, Q.; Klein, B. D.; Zhou, Y. S.; Wang, Z. L. Theoretical Study of Piezo-Phototronic Nano-Leds. *Adv. Mater.* **2014**, *26*, 7209–7216.
- (263) Pan, C.; Chen, M.; Yu, R.; Yang, Q.; Hu, Y.; Zhang, Y.; Wang, Z. L. Progress in Piezo-Phototronic-Effect-Enhanced Light-Emitting Diodes and Pressure Imaging. *Adv. Mater.* **2016**, *28*, 1535–1552.
- (264) Wang, C.; Ba, R.; Zhao, K.; Zhang, T.; Dong, L.; Pan, C. Enhanced Emission Intensity of Vertical Aligned Flexible Zno Nanowire/P-Polymer Hybridized Led Array by Piezo-Phototronic Effect. *Nano Energy* **2015**, *14*, 364–371.
- (265) Bao, R.; Wang, C.; Peng, Z.; Ma, C.; Dong, L.; Pan, C. Light-Emission Enhancement in a Flexible and Size-Controllable Zno Nanowire/Organic Light-Emitting Diode Array by the Piezotronic Effect. *ACS Photonics* **2017**, *4*, 1344–1349.
- (266) Bao, R. R.; Wang, C. F.; Dong, L.; Shen, C. Y.; Zhao, K.; Pan, C. F. Cds Nanorods/Organic Hybrid Led Array and the Piezo-Phototronic Effect of the Device for Pressure Mapping. *Nanoscale* **2016**, *8*, 8078–8082.
- (267) Chen, M. X.; Pan, C. F.; Zhang, T. P.; Li, X. Y.; Liang, R. R.; Wang, Z. L. Tuning Light Emission of a Pressure-Sensitive Silicon/Zno Nanowires Heterostructure Matrix through Piezo-Phototronic Effects. *ACS Nano* **2016**, *10*, 6074–6079.
- (268) Zhang, T.; Liang, R.; Dong, L.; Wang, J.; Xu, J.; Pan, C. Wavelength-Tunable Infrared Light Emitting Diode Based on Ordered Zno Nanowire/Sil-Xgexalloy Heterojunction. *Nano Res.* **2015**, *8*, 2676–2685.
- (269) Pan, C. F.; Dong, L.; Zhu, G.; Niu, S. M.; Yu, R. M.; Yang, Q.; Liu, Y.; Wang, Z. L. High-Resolution Electroluminescent Imaging of Pressure Distribution Using a Piezoelectric Nanowire Led Array. *Nat. Photonics* **2013**, *7*, 752–758.
- (270) Peng, Y.; Que, M.; Lee, H. E.; Bao, R.; Wang, X.; Lu, J.; Yuan, Z.; Li, X.; Tao, J.; Sun, J.; et al. Achieving High-Resolution Pressure Mapping Via Flexible Gan/ Zno Nanowire Leds Array by Piezo-Phototronic Effect. *Nano Energy* **2019**, *58*, 633–640.
- (271) Li, X. Y.; Chen, M. X.; Yu, R. M.; Zhang, T. P.; Song, D. S.; Liang, R. R.; Zhang, Q. L.; Cheng, S. B.; Dong, L.; Pan, A. L.; et al. Enhancing Light Emission of Zno-Nanofilm/Si-Micropillar Heterostructure Arrays by Piezo-Phototronic Effect. *Adv. Mater.* **2015**, *27*, 4447–4453.
- (272) Shi, J.; Starr, M. B.; Xiang, H.; Hara, Y.; Anderson, M. A.; Seo, J. H.; Ma, Z.; Wang, X. Interface Engineering by Piezoelectric Potential in Zno-Based Photoelectrochemical Anode. *Nano Lett.* **2011**, *11*, 5587–5593.
- (273) Wang, X.; Rohrer, G. S.; Li, H. Piezotronic Modulations in Electro- and Photochemical Catalysis. *MRS Bull.* **2018**, *43*, 946–951.
- (274) Zhao, L. L.; Zhang, Y.; Wang, F. L.; Hu, S. C.; Wang, X. N.; Ma, B. J.; Liu, H.; Wang, Z. L.; Sang, Y. H. Batio3 Nanocrystal-Mediated Micro Pseudo-Electrochemical Cells with Ultrasound-Driven Piezotronic Enhancement for Polymerization. *Nano Energy* **2017**, *39*, 461–469.
- (275) Zhang, S.; Yin, C.; Kang, Z.; Wu, P.; Wu, J.; Zhang, Z.; Liao, Q.; Zhang, J.; Zhang, Y. Graphdiyne Nanowall for Enhanced Photoelectrochemical Performance of Si Heterojunction Photoanode. *ACS Appl. Mater. Interfaces* **2019**, *11*, 2745.
- (276) Yu, Y.; Zhang, Z.; Yin, X.; Kvit, A.; Liao, Q.; Kang, Z.; Yan, X.; Zhang, Y.; Wang, X. Enhanced Photoelectrochemical Efficiency and Stability Using a Conformal Tio2 Film on a Black Silicon Photoanode. *Nat. Energy* **2017**, *2*, 17045.
- (277) Qin, Z.; Liao, Q.; Huang, Y.; Tang, L.; Zhang, X.; Zhang, Y. Effect of Hydrothermal Reaction Temperature on Growth, Photoluminescence and Photoelectrochemical Properties of Zno Nanorod Arrays. *Mater. Chem. Phys.* **2010**, *123*, 811–815.
- (278) Qin, Z.; Huang, Y.; Qi, J.; Li, H.; Su, J.; Zhang, Y. Facile Synthesis and Photoelectrochemical Performance of the Bush-Like Zno Nanosheets Film. *Solid State Sci.* **2012**, *14*, 155–158.
- (279) Liu, Y.; Kang, Z.; Zhang, S.; Li, Y.; Wu, H.; Wu, J.; Wu, P.; Zhang, Z.; Liao, Q.; Zhang, Y. Ferroelectric Polarization-Enhanced Charge Separation in a Vanadium-Doped Zno Photoelectrochemical System. *Inorg. Chem. Front.* **2018**, *5*, 1533–1539.
- (280) Liu, Y.; Gu, Y.; Yan, X.; Kang, Z.; Lu, S.; Sun, Y.; Zhang, Y. Design of Sandwich-Structured Zno/Zns/Au Photoanode for Enhanced Efficiency of Photoelectrochemical Water Splitting. *Nano Res.* **2015**, *8*, 2891–2900.
- (281) Kang, Z.; Li, Y.; Yu, Y.; Liao, Q.; Zhang, Z.; Guo, H.; Zhang, S.; Wu, J.; Si, H.; Zhang, X.; et al. Facile Synthesis of Nico2s4 Nanowire Arrays on 3d Graphene Foam for High-Performance Electrochemical Capacitors Application. *J. Mater. Sci.* **2018**, *53*, 10292–10301.

- (282) Kang, Z.; Li, Y.; Cao, S.; Zhang, Z.; Guo, H.; Wu, P.; Zhou, L.; Zhang, S.; Zhang, X.; Zhang, Y. 3d Graphene Foam/Zno Nanorods Array Mixed-Dimensional Heterostructure for Photoelectrochemical Biosensing. *Inorg. Chem. Front.* **2018**, *5*, 364–369.
- (283) Xue, X.; Zang, W.; Deng, P.; Wang, Q.; Xing, L.; Zhang, Y.; Wang, Z. L. Piezo-Potential Enhanced Photocatalytic Degradation of Organic Dye Using Zno Nanowires. *Nano Energy* **2015**, *13*, 414–422.
- (284) Zhang, Y.; Liu, C. H.; Zhu, G. L.; Huang, X.; Liu, W.; Hu, W. G.; Song, M.; He, W. D.; Liu, J.; Zhai, J. Y. Piezotronic-Effect-Enhanced Ag<sub>2</sub>S/Zno Photocatalyst for Organic Dye Degradation. *RSC Adv.* **2017**, *7*, 48176–48183.
- (285) Li, H. D.; Sang, Y. H.; Chang, S. J.; Huang, X.; Zhang, Y.; Yang, R. S.; Jiang, H. D.; Liu, H.; Wang, Z. L. Enhanced Ferroelectric-Nanocrystal-Based Hybrid Photocatalysis by Ultrasonic-Wave-Generated Piezophototronic Effect. *Nano Lett.* **2015**, *15*, 2372–2379.
- (286) Wang, L. F.; Liu, S. H.; Wang, Z.; Zhou, Y. L.; Qin, Y.; Wang, Z. L. Piezotronic Effect Enhanced Photocatalysis in Strained Anisotropic Zno/Tio<sub>2</sub> Nanoplatelets Via Thermal Stress. *ACS Nano* **2016**, *10*, 2636–2643.
- (287) Bae, Y.; Fukushima, S.; Harada, A.; Kataoka, K. Design of Environment-Sensitive Supramolecular Assemblies for Intracellular Drug Delivery: Polymeric Micelles That Are Responsive to Intracellular Ph Change. *Angew. Chem., Int. Ed.* **2003**, *42*, 4640–4643.
- (288) Bai, Z.; Yan, X.; Chen, X.; Cui, Y.; Lin, P.; Shen, Y.; Zhang, Y. Ultraviolet and Visible Photoresponse Properties of a Zno/Si Heterojunction at Zero Bias. *RSC Adv.* **2013**, *3*, 17682.
- (289) Bai, Z.; Yan, X.; Chen, X.; Liu, H.; Shen, Y.; Zhang, Y. Zno Nanowire Array Ultraviolet Photodetectors with Self-Powered Properties. *Curr. Appl. Phys.* **2013**, *13*, 165–169.
- (290) Bai, Z.; Yan, X.; Li, Y.; Kang, Z.; Cao, S.; Zhang, Y. 3d-Branched Zno/Cds Nanowire Arrays for Solar Water Splitting and the Service Safety Research. *Adv. Energy Mater.* **2016**, *6*, 1501459.
- (291) Bao, R. R.; Wang, C. F.; Peng, Z. C.; Ma, C.; Dong, L.; Pan, C. F. Light-Emission Enhancement in a Flexible and Size-Controllable Zno Nanowire/Organic Light-Emitting Diode Array by the Piezotronic Effect. *ACS Photonics* **2017**, *4*, 1344–1349.
- (292) Zou, H. Y.; Li, X. G.; Peng, W. B.; Wu, W. Z.; Yu, R. M.; Wu, C. S.; Ding, W. B.; Hu, F.; Liu, R. Y.; Zi, Y. L.; et al. Piezo-Phototronic Effect on Selective Electron or Hole Transport through Depletion Region of Vis-Nir Broadband Photodiode. *Adv. Mater.* **2017**, *29*, 1701412.
- (293) Zhu, L. P.; Lin, P.; Chen, B. D.; Wang, L. F.; Chen, L. B.; Li, D.; Wang, Z. L. Piezo-Phototronic and Pyro-Phototronic Effects to Enhance Cu(in, Ga)Se-2 Thin Film Solar Cells. *Nano Res.* **2018**, *11*, 3877–3885.
- (294) Zhang, K. W.; Wang, Z. L.; Yang, Y. Enhanced P3ht/Zno Nanowire Array Solar Cells by Pyro-Phototronic Effect. *ACS Nano* **2016**, *10*, 10331–10338.
- (295) Yu, R. M.; Wu, W. Z.; Pan, C. F.; Wang, Z. N.; Ding, Y.; Wang, Z. L. Piezo-Phototronic Boolean Logic and Computation Using Photon and Strain Dual-Gated Nanowire Transistors. *Adv. Mater.* **2015**, *27*, 940–947.
- (296) Wen, X. N.; Wu, W. Z.; Ding, Y.; Wang, Z. L. Piezotronic Effect in Flexible Thin-Film Based Devices. *Adv. Mater.* **2013**, *25*, 3371–3379.
- (297) Wang, X. F.; Yu, R. M.; Jiang, C. Y.; Hu, W. G.; Wu, W. Z.; Ding, Y.; Peng, W. B.; Li, S. T.; Wang, Z. L. Piezotronic Effect Modulated Heterojunction Electron Gas in Algan/Aln/Gan Heterostructure Microwire. *Adv. Mater.* **2016**, *28*, 7234–7242.
- (298) Liu, S. H.; Wang, L. F.; Feng, X. L.; Wang, Z.; Xu, Q.; Bai, S.; Qin, Y.; Wang, Z. L. Ultrasensitive 2d Zno Piezotronic Transistor Array for High Resolution Tactile Imaging. *Adv. Mater.* **2017**, *29*, 1606346.
- (299) Zhu, L. P.; Zhang, Y.; Lin, P.; Wang, Y.; Yang, L. J.; Chen, L. B.; Wang, L. F.; Chen, B. D.; Wang, Z. L. Piezotronic Effect on Rashba Spin-Orbit Coupling in a Zno/P3ht Nanowire Array Structure. *ACS Nano* **2018**, *12*, 1811–1820.
- (300) Hu, G. W.; Zhang, Y.; Li, L. J.; Wang, Z. L. Piezotronic Transistor Based on Topological Insulators. *ACS Nano* **2018**, *12*, 779–785.
- (301) Han, X.; Du, W. M.; Chen, M. X.; Wang, X. D.; Zhang, X. J.; Li, X. Y.; Li, J.; Peng, Z. C.; Pan, C. F.; Wang, Z. L. Visualization Recording and Storage of Pressure Distribution through a Smart Matrix Based on the Piezotronic Effect. *Adv. Mater.* **2017**, *29*, 1701253.
- (302) Pradel, K. C.; Wu, W. Z.; Zhou, Y. S.; Wen, X. N.; Ding, Y.; Wang, Z. L. Piezotronic Effect in Solution-Grown P-Type Zno Nanowires and Films. *Nano Lett.* **2013**, *13*, 2647–2653.
- (303) Jiang, C. Y.; Liu, T.; Du, C. H.; Huang, X.; Liu, M. M.; Zhao, Z. F.; Li, L. X.; Pu, X.; Zhai, J. Y.; Hu, W. G.; et al. Piezotronic Effect Tuned Algan/Gan High Electron Mobility Transistor. *Nanotechnology* **2017**, *28*, 455203.
- (304) Dai, Y. J.; Wang, X. F.; Peng, W. B.; Zou, H. Y.; Yu, R. M.; Ding, Y.; Wu, C. S.; Wang, Z. L. Largely Improved near-Infrared Silicon-Photosensing by the Piezo-Phototronic Effect. *ACS Nano* **2017**, *11*, 7118–7125.
- (305) Dai, Y. J.; Wang, X. F.; Peng, W. B.; Xu, C.; Wu, C. S.; Dong, K.; Liu, R. Y.; Wang, Z. L. Self-Powered Si/Cds Flexible Photodetector with Broadband Response from 325 to 1550 Nm Based on Pyro-Phototronic Effect: An Approach for Photosensing Below Bandgap Energy. *Adv. Mater.* **2018**, *30*, 1705893.
- (306) Dai, Y. J.; Wang, X. F.; Peng, W. B.; Wu, C. S.; Ding, Y.; Dong, K.; Wang, Z. L. Enhanced Performances of Si/Cds Heterojunction near-Infrared Photodetector by the Piezo-Phototronic Effect. *Nano Energy* **2018**, *44*, 311–318.
- (307) Dai, G. Z.; Zou, H. Y.; Wang, X. F.; Zhou, Y. K.; Wang, P. H.; Ding, Y.; Zhang, Y.; Yang, J. L.; Wang, Z. L. Piezo-Phototronic Effect Enhanced Responsivity of Photon Sensor Based on Composition-Tunable Ternary Cdsxse1-X Nanowires. *ACS Photonics* **2017**, *4*, 2495–2503.
- (308) Chen, Y.; Zhang, Y.; Karnaushenko, D.; Chen, L.; Hao, J. H.; Ding, F.; Schmidt, O. G. Addressable and Color-Tunable Piezophotonic Light-Emitting Stripes. *Adv. Mater.* **2017**, *29*, 1605165.
- (309) Chen, M. X.; Zhao, B.; Hu, G. F.; Fang, X. S.; Wang, H.; Wang, L.; Luo, J.; Han, X.; Wang, X. D.; Pan, C. F.; et al. Piezo-Phototronic Effect Modulated Deep Uv Photodetector Based on Zno-Ga<sub>2</sub>O<sub>3</sub> Heterojunction Microwire. *Adv. Funct. Mater.* **2018**, *28*, 1700264.
- (310) Chen, L.; Wong, M. C.; Bai, G. X.; Jie, W. J.; Hao, J. H. White and Green Light Emissions of Flexible Polymer Composites under Electric Field and Multiple Strains. *Nano Energy* **2015**, *14*, 372–381.
- (311) Wang, X. D.; Zhang, Y. F.; Zhang, X. J.; Huo, Z. H.; Li, X. Y.; Que, M. L.; Peng, Z. C.; Wang, H.; Pan, C. F. A Highly Stretchable Transparent Self-Powered Triboelectric Tactile Sensor with Metalized Nanofibers for Wearable Electronics. *Adv. Mater.* **2018**, *30*, 1706738.
- (312) Wang, X. D.; Zhang, H. L.; Dong, L.; Han, X.; Du, W. M.; Zhai, J. Y.; Pan, C. F.; Wang, Z. L. Self-Powered High-Resolution and Pressure-Sensitive Triboelectric Sensor Matrix for Real-Time Tactile Mapping. *Adv. Mater.* **2016**, *28*, 2896–2903.
- (313) Xue, F.; Zhang, L. M.; Feng, X. L.; Hu, G. F.; Fan, F. R.; Wen, X. N.; Zheng, L.; Wang, Z. L. Influence of External Electric Field on Piezotronic Effect in Zno Nanowires. *Nano Res.* **2015**, *8*, 2390–2399.
- (314) Xue, F.; Yang, L. J.; Chen, M. X.; Chen, J.; Yang, X. N.; Wang, L. F.; Chen, L. B.; Pan, C. F.; Wang, Z. L. Enhanced Photoresponsivity of the Mos<sub>2</sub>-Gan Heterojunction Diode Via the Piezo-Phototronic Effect. *NPG Asia Mater.* **2017**, *9*, No. e418.
- (315) Liu, X. Q.; Yang, X. N.; Gao, G. Y.; Yang, Z. Y.; Liu, H. T.; Li, Q.; Lou, Z.; Shen, G. Z.; Liao, L.; Pan, C. F.; et al. Enhancing Photoresponsivity of Self-Aligned Mos<sub>2</sub> Field-Effect Transistors by Piezo-Phototronic Effect from Gan Nanowires. *ACS Nano* **2016**, *10*, 7451–7457.
- (316) Liu, W.; Zhou, Y. L.; Zhang, A. H.; Zhang, Y.; Wang, Z. L. Theoretical Study on the Top- and Enclosed-Contacted Single-Layer Mos<sub>2</sub> Piezotronic Transistors. *Appl. Phys. Lett.* **2016**, *108*, 181603.

(317) Huang, X.; Liu, W.; Zhang, A. H.; Zhang, Y.; Wang, Z. L. Ballistic Transport in Single-Layer Mos<sub>2</sub> Piezotronic Transistors. *Nano Res.* **2016**, *9*, 282–290.

(318) Peng, Y. Y.; Que, M. L.; Tao, J.; Wang, X. D.; Lu, J. F.; Hu, G. F.; Wan, B. S.; Xu, Q.; Pan, C. F. Progress in Piezotronic and Piezo-Phototronic Effect of 2d Materials. *2D Mater.* **2018**, *5*, No. 042003.